

Numerical and Experimental Studies of Two-Body Hydrodynamic Interaction in Waves

by

© *Wei Meng*

A thesis submitted to the
School of Graduate Studies
in partial fulfilment of the
requirements for the degree of
Doctor of Philosophy

Faculty of Engineering and Applied Science
Memorial University of Newfoundland

October 2020

St. John's

Newfoundland

Abstract

Challenges remain in the prediction of hydrodynamic interactions of multiple floating bodies in close proximity, such as side-by-side offloading and ship replenishment. During such operations, large free-surface elevations in the gap and body motions may occur, impacting operation and crew safety. In this thesis, numerical and experimental studies are presented, focusing on the two-body interactions in waves.

Linear potential-flow based seakeeping programs have been widely employed to solve hydrodynamic interaction problems due to their high efficiency. However, these methods over-predict body motions, free surface elevations in the gap, and hence low-frequency loadings on the bodies. To suppress the over-predictions, artificial damping is required as input, which is typically obtained from model tests.

With objectives of investigating the effects of viscosity and dynamic gap changes in the two-body interaction problem and developing a systematic approach to estimate the artificial damping for use in potential-flow tools, an immersed-boundary method based finite volume method solver has been implemented in the OpenFOAM framework. The pressure implicit with splitting of operators (PISO) algorithm is applied for velocity-pressure coupling. Free surface is captured using the geometrical volume of fluid method. The relaxation zone method is utilized for wave generation and absorption.

To provide high-quality experimental data and to validate the numerical method, model tests on two identical box-like FPSO models arranged side-by-side in head waves at zero forward speed have been conducted in the towing tank of Memorial University. Besides, sources of uncertainties in the model test were identified, and

comprehensive uncertainty analysis on the test results was conducted. A combined experimental and numerical approach has been developed to estimate uncertainties due to model geometry, model mass properties, and test set-up.

Validation studies on the present flow solver were conducted by firstly simulating the present experiment for two-body interactions in head seas without forward speed. Further, the solver was validated by simulating the underway replenishment of a frigate and a supply vessel at a moderate speed. Simulations were also performed using a panel-free method based potential-flow program in the frequency domain. The numerical results from both methods were compared with each other and with the experimental data to identify sources of the discrepancies in potential-flow predictions. A quasi-steady approach, which accounts for the gap changes due to transverse drift forces at zero speed, was adopted to improve the potential-flow simulations.

Acknowledgements

I would like to express my greatest appreciation and thanks to my supervisor, Dr. Wei Qiu, for his guidance, support, and encouragement throughout my studies and research. The countless instructions and discussions from him significantly enhanced my knowledge in the field of marine hydrodynamics. I am very grateful for the opportunities provided by Dr. Qiu to be involved in research projects and undergraduate course teaching, from which I have gained invaluable experience.

My gratitude also goes to Dr. Heather Peng for her sharp advice and insightful comments. She has been generously sharing her knowledge and playing an important role throughout this research work.

I would like to thank my colleagues and friends, Peng Wen, Md. Ashim Ali, Ruosi Zha, Saeed Barzegar Valikchali, Shanqin Jin, Quan Zhou, Junshi Wang, Jie Dai, and Boyang Zhang, at Memorial University for the fruitful discussions and happy memories. Special thanks are given to Weiwen Zhao from Shanghai Jiao Tong University for the useful help on OpenFOAM programming.

I would like to express my sincere appreciation to Trevor Clark, Matt Curtis, and Craig Mitchell for all their help and support during my experiments.

Last but not least, I am thoroughly grateful to my family. I would like to thank my wife, Meng Chen, for her love, support, and understanding throughout my work. I would like to give my thanks to my daughter, Qiaoyi Meng. Watching you grow up every day is the happiest experience I have ever had. I would also like to express my gratitude to my parents and parents-in-law for their unconditional love and support.

Contents

Abstract	ii
Acknowledgements	iv
List of Tables	ix
List of Figures	xi
1 Introduction	1
1.1 Background	1
1.1.1 Numerical Studies	1
1.1.1.1 Potential-flow methods	3
1.1.1.2 CFD methods	6
1.1.2 Experimental Studies	9
1.1.2.1 Model tests	9
1.1.2.2 Uncertainty analysis	13
1.2 Present Work	14
1.3 Thesis Outline	15

2	Mathematical Formulations	17
2.1	Coordinate Systems	17
2.2	Governing Equations	17
2.3	Flow Solver	19
2.4	Immersed-boundary Treatment	21
2.5	Free-surface Capturing	23
2.6	Numerical Wave Tank	25
2.7	Evaluation of Uncertainties Due to Spatial Discretization	27
3	Model Tests and Uncertainty Analysis of Two-body Interaction at Zero Speed	29
3.1	Model Tests	30
3.1.1	Experimental Set-up	30
3.1.2	Instrumentation and Pre-tests	33
3.1.3	Experimental Data Processing	37
3.2	Uncertainty Analysis	38
3.2.1	Uncertainty Analysis Method	39
3.2.2	Uncertainty Analysis of the Measurements	41
3.2.3	Type B Uncertainties Determined from Pre-tests	44
3.2.3.1	Uncertainties from load cell calibration	46
3.2.3.2	Uncertainties from wave probe calibration	49
3.2.3.3	Uncertainties from the Qualisys system calibration	49
3.2.3.4	Uncertainties from wave calibration	51

3.2.3.5	Uncertainties from swing tests	51
3.2.4	Type B Uncertainties Evaluated from Manufacturer’s Specifi- cations	54
3.2.4.1	Uncertainties from DAQ system	55
3.2.4.2	Uncertainties from power supply	56
3.2.5	Type B Uncertainties Estimated from Numerical Simulations .	57
3.2.5.1	Uncertainties due to model geometries	57
3.2.5.2	Uncertainties due to model mass properties	59
3.2.5.3	Uncertainties due to mooring set-up	61
3.2.6	Summary of the Type B Standard Uncertainties of the Mea- surements	66
3.2.6.1	Type B standard uncertainty of the incident wave am- plitude	66
3.2.6.2	Type B standard uncertainty of wave amplitudes in the gap	66
3.2.6.3	Type B standard uncertainty of drift forces	67
3.2.6.4	Type B standard uncertainty of 6-DOF motion am- plitudes	67
3.2.7	Uncertainties in Data Analysis	67
3.3	Summary	69
4	Numerical Simulations on Two-body Interactions in Waves	72
4.1	Two-body Interactions in Waves at Zero Speed	75
4.1.1	Set-up for CFD Simulations	75

4.1.2	Set-up for Potential-flow Simulations	76
4.1.3	Uncertainty Analysis and Convergence Studies	77
4.1.4	Validation Studies	85
4.2	Ship Replenishment in Waves with Forward Speed	103
4.2.1	Set-up for CFD Simulations	105
4.2.2	Set-up for Potential-flow Simulations	105
4.2.3	Uncertainty Analysis and Convergence Studies	107
4.2.4	Validation Studies	115
4.3	Summary	121
5	Conclusions and Future Work	124
5.1	Conclusions	124
5.2	Future Work	126
5.2.1	Numerical Aspects	127
5.2.2	Experimental Aspects	128
A	Example of Uncertainty Calculation	141
B	Investigations on Wave Modelling	144

List of Tables

3.1	Particulars of full-scale bodies and models (1:60)	31
3.2	Test matrix for waves	31
3.3	Sources of uncertainties in the two-body interaction tests	40
3.4	Sources of Type B uncertainty included in the calculations	45
3.5	Sources of Type B uncertainty considered in the calculations	46
3.6	Uncertainties determined from calibrations of load cells	48
3.7	Uncertainties determined from calibrations of wave probes	49
3.8	Uncertainties of the Qualisys system for two models	51
3.9	Uncertainties in the swing tests (Model 1)	52
3.10	Summary of swing test results (KG and radii of gyration) for Model 1	54
3.11	Uncertainties in DAQ system from specifications	55
3.12	Uncertainties in power supply from specifications	56
4.1	Uncertainties in motions of Body 1, wave elevations in the gap, and mean drift forces on Body 1 from OpenFOAM at $\omega = 4.65$ rad/s . . .	78
4.2	Uncertainties in motions of Body 1, wave elevations in the gap, and mean drift forces on Body 1 from OpenFOAM at $\omega = 5.72$ rad/s . . .	82

4.3	Uncertainties in motions of Body 1, wave elevations in the gap, and mean drift forces on Body 1 from OpenFOAM at $\omega = 6.91$ rad/s . . .	84
4.4	Uncertainties in motions of Body 1, wave elevations in the gap, and mean drift forces on Body 1 from OpenFOAM at $\omega = 7.04$ rad/s . . .	85
4.5	Particulars of full-scale ships and models	104
4.6	Wave frequencies for the replenishment model tests in model scale . .	106
4.7	Uncertainties in motions of two ships from OpenFOAM with frigate and supply vessel aligned at midships at $U = 1.23$ m/s and $\omega = 2.51$ rad/s	110
4.8	Uncertainties in motions of two ships from OpenFOAM with frigate ahead of supply vessel at $U = 1.23$ m/s and $\omega = 3.18$ rad/s	112
4.9	Uncertainties in motions of two ships from OpenFOAM with frigate and supply vessel aligned at midships at $U = 1.23$ m/s and $\omega = 4.10$ rad/s	113
A.1	Type A standard uncertainties (at the wave frequency of 5.91 rad/s) .	142
A.2	Type B standard uncertainties (at the wave frequency of 5.91 rad/s) .	142
A.3	Combined uncertainties (at the wave frequency of 5.91rad/s)	143

List of Figures

1.1	Side-by-Side Offloading Operation (www.royalhaskoningdhv.com) . . .	2
1.2	Ship Replenishment (McTaggart, 2017)	2
2.1	Coordinate Systems	18
2.2	Three-phase Flow	21
2.3	Free-surface Reconstruction and Advection	24
2.4	Relaxation Zones	25
3.1	Ship Models in Waves	30
3.2	Experimental Set-up	32
3.3	Mooring System Set-up	33
3.4	Mooring Line Connection Point on a Model	34
3.5	An Example of Load Cell Calibration Curve	35
3.6	An Example of Wave Probe Calibration Curve	35
3.7	An Example of the Qualisys System Calibration Report	36
3.8	Swing Test Set-up	37
3.9	Type B Uncertainty Sources	43
3.10	Load Cell Calibration Curve	47

3.11	Noise in Heave Motion of Model 1	50
3.12	Surge of Model 1 due to Uncertainties in Model Length	60
3.13	Wave Elevation at WP4 due to Uncertainties in Model Breadth	60
3.14	Longitudinal Mean Drift Force on Model 1 due to Uncertainties in Model Draft	61
3.15	Roll of Model 1 due to Uncertainties in KG	62
3.16	Roll of Model 1 due to Uncertainties in Roll Radius of Gyration	62
3.17	Transverse Mean Drift Force on Model 1 due to Uncertainty in Mooring Stiffness	63
3.18	Heave of Model 1 due to Uncertainties in Gap Width	64
3.19	Wave Elevation at WP4 due to Uncertainties in Gap Width	64
3.20	Longitudinal Mean Drift Force on Model 1 due to Uncertainties in Gap Width	65
3.21	Time Series of Heave Motion for Model 1	68
3.22	Time Series of Wave Elevation at WP4	68
3.23	Time Series of Mooring Line Tension of Mooring Line M1 for Model 1	68
3.24	Heave of Model 1 Using Different Segments for Data Analysis	69
3.25	Wave Elevation at WP4 Using Different Segments for Data Analysis	70
3.26	Transverse Mean Drift Force on Model 1 Using Different Segments for Data Analysis	71
4.1	Background Mesh (Top: Section View; Bottom: Side View)	74
4.2	Convergence Study on Cell Size in Body Refinement Zone	74
4.3	Simulation Set-up	75

4.4	Gaussian Point Distribution on Ship Hull Surfaces	76
4.5	Temporal Convergence for Motions of Body 1 and Wave Elevations in the Gap from OpenFOAM at $\omega = 4.65$ rad/s	80
4.6	Temporal Convergence for Motions of Body 1, Mean Drift Forces on Body 1 and Wave Elevations in the Gap from OpenFOAM at $\omega = 5.72$ rad/s	81
4.7	Temporal Convergence for Motions of Body 1, Mean Drift Forces on Body 1 and Wave Elevations in the Gap from OpenFOAM at $\omega = 6.91$ rad/s	83
4.8	Temporal Convergence for Motions of Body 1, Mean Drift Forces on Body 1 and Wave Elevations in the Gap from OpenFOAM at $\omega = 7.04$ rad/s	86
4.9	Time Series of Sway of Bodies 1 and 2, Heave and Roll of Body 1 and Wave Elevation at WP6 at $\omega = 3.90$ rad/s	88
4.10	Time Series of Sway of Bodies 1 and 2, Heave and Roll of Body 1 and Wave Elevation at WP6 at $\omega=5.72$ rad/s	89
4.11	Time Series of Sway of Bodies 1 and 2, Heave and Roll of Body 1 and Wave Elevation at WP6 at $\omega=6.91$ rad/s	90
4.12	Comparison between Numerical Simulation and Model Test at $\omega=6.91$ rad/s	91
4.13	Surge Motion of Body 1	93
4.14	Sway Motion of Body 1	93
4.15	Heave Motion of Body 1	94
4.16	Roll Motion of Body 1	94

4.17 Pitch Motion of Body 1	95
4.18 Yaw Motion of Body 1	95
4.19 Wave Elevation at WP4	96
4.20 Wave Elevation at WP5	96
4.21 Wave Elevation at WP6	97
4.22 Longitudinal Drift Force on Body 1	97
4.23 Transverse Drift Force on Body 1	98
4.24 Mean Gap Width	98
4.25 Surge Motion of Body 1	99
4.26 Heave Motion of Body 1	100
4.27 Roll Motion of Body 1	100
4.28 Pitch Motion of Body 1	101
4.29 Wave Elevation at WP5	101
4.30 Wave Elevation at WP6	102
4.31 Longitudinal Drift Force on Body 1	102
4.32 Transverse Drift Force on Body 1	103
4.33 Supply Ship and Frigate Models	104
4.34 Ship Replenishment Set-up	105
4.35 Simulation Set-up	106
4.36 Gaussian Point Distribution on Ship Hull Surfaces	107
4.37 Temporal Convergence for Motions of Two Ships from OpenFOAM with Frigate and Supply Vessel Aligned at Midships at $U = 1.23$ m/s and $\omega = 2.51$ rad/s	109

4.38	Temporal Convergence for Motions of Two Ships with Frigate and Supply Vessel Aligned at Midships from OpenFOAM at $U = 1.23$ m/s and $\omega = 2.51$ rad/s	111
4.39	Temporal Convergence for Motions of Two Ships from OpenFOAM with Frigate and Supply Vessel Aligned at Midships at $U = 1.23$ m/s and $\omega = 4.10$ rad/s	114
4.40	Time Series of Motions for Two Ship Models from OpenFOAM at $U = 1.23$ m/s and $\omega = 3.18$ rad/s - Aligned Longitudinally at Midships	115
4.41	Time Series of Motions for Two Ship Models from OpenFOAM at $U = 1.23$ m/s and $\omega = 3.18$ rad/s - Frigate ahead of Supply Ship	116
4.42	Two Ships in Waves at $U = 1.23$ m/s and $\omega = 3.18$ rad/s - Aligned Longitudinally at Midships (left) and Frigate ahead of Supply Ship (Right)	117
4.43	Heave Motions of Two Ships in Two Side-by-Side Arrangements - Aligned Longitudinally at Midships (Top) and Frigate ahead of Supply Ship (Bottom)	118
4.44	Roll Motions of Two Ships in Two Side-by-Side Arrangements - Aligned Longitudinally at Midships (Top) and Frigate ahead of Supply Ship (Bottom)	119
4.45	Pitch Motions of Two Ships in Two Side-by-Side Arrangements - Aligned Longitudinally at Midships (Top) and Frigate ahead of Supply Ship (Bottom)	120
B.1	Simulation Set-up	145

B.2	Effect of Vertical Cell Size on Wave Generation	146
B.3	Effect of Cell Aspect Ratio on Wave Generation	148
B.4	Effect of Damping Zone Length on Wave Generation	149
B.5	Effect of Damping Zone Length on Wave Generation	150
B.6	Effect of Time Step on Wave Generation	151

Chapter 1

Introduction

1.1 Background

Prediction of hydrodynamic interactions of multiple floating bodies in close proximity remains challenging. During operations, such as side-by-side offloading (see Fig. 1.1) and underway ship replenishment (see Fig. 1.2), large free surface elevations in the gap and body motions may occur, impacting operation and crew safety.

1.1.1 Numerical Studies

Extensive numerical studies have been carried out on the two-body interaction problem. Potential-flow based methods have been widely adopted by the industry for their high efficiency. However, due to the ignorance of viscous effects, they over-predict responses, such as wave elevations in the gap between bodies and low-frequency loadings. On the other hand, as computational power increases, Computational Fluid Dynamics (CFD) approaches become progressively applied to account for the viscous



Figure 1.1: Side-by-Side Offloading Operation (www.royalhaskoningdhv.com)



Figure 1.2: Ship Replenishment (McTaggart, 2017)

effects and to model highly nonlinear free surface movements.

1.1.1.1 Potential-flow methods

Early investigations were focused on analytical solutions of resonant free surface elevations in fixed gaps. For example, Molin (2001) derived the analytical solution of the natural modes, including the piston and the sloshing modes, of the free surfaces between two fixed barges with infinite lengths and beams in infinitely deep water. Faltinsen et al. (2007) used the domain decomposition method, and analytically investigated the piston-like sloshing in the two-dimensional gap in between two heaving rectangular boxes.

Besides the analytical solutions, numerical simulations utilizing the potential-flow theory have been carried out; however, they over-predict the free surface elevations between bodies. For example, Newman and Sclavounos (1988) used a 3D panel method to predict hydrodynamic coefficients of two identical side-by-side barges and wave elevations in the gap when the two bodies undergo forced motions. Pronounced wave resonance was observed from their predictions, with the wave elevation in the middle of the gap 50 times the forced heave amplitude.

To overcome the over-prediction problem, researchers have developed different techniques. For instance, Huijsmans et al. (2001) developed a lid technique, in which a rigid lid is applied on the free surface in the gap to suppress unrealistic solutions. Buchner et al. (2001) used this method along with the impulse response function method (Cummins, 1962) to compute the hydrodynamic responses of a barge-type Liquefied Natural Gas (LNG) Floating Production Storage and Offloading (FPSO) and an LNG shuttle tanker arranged side-by-side in the time domain. The results

were compared to the model test data, and it was found that the over-predictions in body motions and drift forces were alleviated.

The lid technique developed by Huijsmans et al. (2001) is successful in suppressing unrealistic responses; however, it does not reflect real physics. Newman (2003) proposed a generalized mode approach to model free surface in the gap, and Chen (2004) included a linear dissipation term in the free surface boundary condition. Fournier et al. (2006) simulated the interactions between two side-by-side vessels using WAMIT and HYDROSTAR, which are based on the methods of Newman (2003) and Chen (2004), respectively. Since no prior guideline was provided on the selection of damping coefficients, various damping values were tested to match the experimental data. Pauw et al. (2007) used the damping lid method (Chen, 2004) to simulate the hydrodynamic responses of an LNG carrier positioned parallel and close to the tank wall. Their work indicated no unique damping coefficient could be determined to cover all the comparisons with experimental results. Also, slight frequency shifts were observed between the numerical and experimental results. To resolve the frequency shift problem in the work of Pauw et al. (2007), Bunnik et al. (2009) applied damping not only to the free surface in the gap between two ships but also to the free surface inside the vessels, which is different from the traditional rigid-lid approach for irregular frequency removal. More recently, Watai et al. (2015) developed a time-domain solver based on the Rankine panel method and applied the damping lid method (Chen, 2004) to suppress the over-predicted motions and wave elevations in the two-body interaction problem. These methods, although effectively address the over-prediction problem, require the input damping coefficients to be “tuned” to match experimental results.

Higher-order boundary element methods (HOBEMs) have also been utilized to study the multi-body interaction problem. Kashiwagi et al. (2005) applied the HOBEM to compute wave exciting forces and wave drift forces on a modified Wigley hull and a rectangular barge in a side-by-side arrangement. In their work, good agreement was achieved between numerical and experimental results. Later, Kashiwagi (2007) applied the HOBEM to compute wave forces on four identical box-shaped bodies. Hong et al. (2013) studied the hydrodynamic interaction between two side-by-side bodies using a nine-node discontinuous higher-order boundary element method (9dHOBEM) and a constant boundary element method based on the boundary matching formulation (BM-CBEM). In their work, it was shown that both BM-CBEM combined with free surface damping and 9dHOBEM combined with wetted surface damping could suppress the unphysical over-predictions in the resonance region. Zhou et al. (2015), Peng et al. (2015) and Qiu et al. (2017) simulated two identical box-like FPSOs in waves using the panel-free method developed by Qiu et al. (2006). The method utilizes Non-Uniform Rational Basis Spline (NURBS) surfaces to represent body surfaces and desingularizes the integral equation over exact body geometries. Feng and Bai (2015) developed a fully nonlinear potential-flow model and simulated the wave resonances in the gap between side-by-side barges. Their study indicated that accounting the free surface nonlinearity does not alleviate the problem of over-predicted resonance response. More recently, Chen et al. (2018) adopted a time-domain Rankine source method with HOBEM to predict motions of a supply ship and a frigate on a parallel course at a moderate speed and investigated the effects of lateral distance and forward speed.

1.1.1.2 CFD methods

Efforts have also been made to investigate the hydrodynamic interactions of floating bodies in close proximity with CFD methods, where the viscous effects, ignored by potential-flow methods, are considered. For example, Lu et al. (2010) predicted wave elevations in the narrow gaps between fixed bodies using a finite element solver, and a significant improvement was observed compared to the potential-flow solutions.

To improve computational efficiency, researchers proposed combined methods that take advantage of the merits of both viscous and potential-flow solvers. For example, Kristiansen and Faltinsen (2012) developed a domain-decomposition method, which combines an FVM viscous flow solver and a potential-flow solver, to study the wave elevations in the gap between two 2D barges. Elie et al. (2013) simulated the wave resonance between two fixed barges with different headings using the Spectral Wave Explicit Navier-Stokes Equations (SWENSE) approach. In the SWENSE method, the incident waves are modelled by a nonlinear potential-flow solver while the diffracted waves are accounted for by a viscous-flow solver.

More recently, Feng et al. (2017) performed CFD simulations on wave resonance in the narrow gap between two side-by-side barges using OpenFOAM. Barges with sharp bilges and rounded bilges were investigated, and it was found that the viscous damping is mainly induced by the sharp bilges. Jiang et al. (2018) studied the wave resonance in the gap between two identical 2D bodies using a numerical wave flume based on OpenFOAM. According to their study, both energy dissipation induced by the fluid rotational motion and energy transformation associated with the free surface are the sources for the over-predicted wave elevations. Their work was further

extended to two non-identical barges (Jiang et al., 2019), and the simulation results showed that when the larger barge is placed in upstream, the total forces on both barges become smaller.

The studies mentioned above were focused on fixed bodies; however, when body motions are involved, the interaction problem becomes more complicated. Various numerical methods can be applied to consider body motions, such as the deforming-mesh method, the overset-mesh method, and the immersed-boundary method. Ok et al. (2017) predicted 6-DOF motions of two side-by-side vessels in regular waves, and Zhuang and Wan (2018) solved the seakeeping problem of a barge and a geosim in a side-by-side arrangement. In their work, the deforming-mesh method was used as the body motions are relatively small. This method is, however, inadequate to deal with large relative body motions since meshes between bodies can be suppressed, stretched or twisted, causing instabilities in simulations. Maysam Mousaviraad et al. (2016) used an incompressible Unsteady Reynolds Averaged Navier Stokes (URANS) solver, CFDSHIP-IOWA V4.5, with an overset grid to simulate interactions of two ships at forward speed in waves. The overset-mesh method is suitable for modelling large body motions; on the other hand, there are challenges associated with implementation and additional computing costs due to the field interpolation between the background mesh and the overset meshes.

Alternatively, the immersed-boundary method, which does not conform to ship geometries as the two methods aforementioned, can be applied to handle large motions of multiple bodies. The governing equations are solved on a Cartesian grid; thus, no mesh deforming or mesh moving is involved. The method was originated by Peskin (1972) to simulate flow patterns around heart valves. According to the work of Mittal

and Iaccarino (2005), immerse boundary methods can be categorized into two main groups: continuous forcing and direct forcing approaches.

In the continuous forcing approach, boundary conditions of the immersed boundaries (IBs) are spread out to a band of computational cells near the IBs using a discrete delta function. Examples can be found in the work of Uhlmann (2005), Yang et al. (2009) and Pinelli et al. (2010). Since this approach smears out solid interfaces, it is not considered suitable to solve fluid-structure interaction (FSI) problems.

The direct forcing approach proposed by Mohd-Yusof (1997), on the other hand, imposes the IB boundary conditions only to background cells near the IBs and preserves the sharp interface properties. Fadlun et al. (2000) applied the direct forcing method to simulate 3D complex flow with moving boundaries and investigated different interpolation procedures from 0th order to 2nd order. Hu and Kashiwagi (2004) developed the constrained interpolation profile (CIP) method to simulate wave-body interaction problems, where the CIP algorithm is used to solve the advection term in the Navier-Stokes (N-S) equations and to capture the free surface. This method was further applied by Hu and Liu (2016) to simulate violent ship-wave interactions and by Wen and Qiu (2018) to solve 3D slamming problems with improved schemes for free surface capturing. Yang and Stern (2009) developed a finite-difference solver with the immersed-boundary method for solid body modelling and the level-set method for free surface capturing. The velocity field near the immersed boundary is reconstructed using a linear function based on the surrounding fluid and rigid-body velocities (Yang and Balaras, 2006). The method was used to compute the wave fields induced by various ships with forward speed. Liu and Hu (2014) proposed an efficient immersed-boundary treatment to suppress pressure oscillations when higher-

order interpolation schemes are applied for forcing calculations, and the method was used to simulate flow past flexible moving bodies. Recently, Meng and Qiu (2019), implemented the immersed-boundary method in OpenFOAM to simulate two-body interactions in waves at zero forward speed and presented preliminary simulation results. The predictions were compared with the model test data from Qiu et al. (2019), and good agreement was achieved. Further, Meng et al. (2020) used the flow solver developed by Meng and Qiu (2019) and conducted comprehensive validation studies by simulating two-body interactions in waves with and without forward speed.

1.1.2 Experimental Studies

The numerical methods need to be validated using model test data; therefore, extensive model tests have been conducted on the multi-body interaction problem. However, it was only until recently, the uncertainties in the test results have been brought to the researchers' attention.

1.1.2.1 Model tests

In early studies, simple geometries with forced motions were used to investigate the hydrodynamic interaction problem. For example, Ohkusu (1969) measured the wave elevations induced by two side-by-side cylinders undergoing forced heave motions. Van Oortmerssen (1979) obtained the hydrodynamic coefficients of a vertical cylinder and a box in each other's vicinity. During the tests, one of the models was forced to oscillate in surge and heave while the other one stayed still.

Later, experiments with more focus on engineering applications were carried out. Kodan (1984) conducted model tests to investigate wave forces and motions of a

barge and a ship adjacent to each other in oblique waves. Buchner et al. (2001) experimentally studied motions and drift forces of a barge-type LNG FPSO and an LNG shuttle tanker arranged side-by-side. Hong et al. (2005) investigated the interaction characteristics of side-by-side moored vessels, including an LNG FPSO, an LNG carrier, and a shuttle tanker. Kashiwagi et al. (2005) carried out experiments on a modified Wigley model and a rectangular barge model fixed side-by-side in beam waves, during which the first-order hydrodynamic forces and the second-order steady forces were measured. Fournier et al. (2006) experimentally studied the resonant behavior of a Floating Storage and Regasification Unit (FSRU) and an LNG carrier in a side-by-side configuration. Large wave elevations in the gap between the two vessels were observed, and it was demonstrated that the resonance in the gap affects the motions and drift forces. Instead of using two ship models, Pauw et al. (2007) took advantage of the mirror effect and positioned an LNG carrier model parallel and close to the sidewall of a basin to mimic two identical models alongside each other.

Besides the work mentioned above, studies have also been performed, emphasizing the gap wave resonance. As examples, Faltinsen et al. (2007) investigated the piston-mode resonance in a moonpool. In their tests, a rectangular ship section with a moonpool, which is composed of two rectangular boxes arranged side-by-side, was forced to oscillate, and the wave elevations in the gap were measured. Molin and Remy (2009) measured the wave elevations in the gap between two identical fixed barges in waves. Two different gap widths were used in their tests, and it was found that the potential-flow based methods over-predict the wave elevations for the narrow gap case but work well for the large gap one.

With increased offshore side-by-side operations, for instance, LNG offloading, ex-

tensive experiments have been carried out in this area. For instance, Zhao et al. (2014) conducted experiments on the dynamic behaviors of an FLNG in a side-by-side configuration with an LNG carrier under the combination of wave, current, and wind. During the tests, the FLNG model was moored by an external turret, and the LNG carrier model was connected to the FLNG model using hawsers and fenders. Perić and Swan (2015) investigated water surface elevation in the gap between a bottom-mounted gravity-based structure and an LNG through laboratory tests. Their study showed that allowing the LNG model to move leads to an increment of the resonance frequency. Watai et al. (2015) experimentally studied the interactions between a fixed barge and a geosim arranged in two different side-by-side configurations. In their test, the geosim was only free to surge, heave, and pitch, keeping the gap width constant. The tank wall effects were also investigated using a series of image bodies in WAMIT, and the results showed that the reflected waves were not significant in the gap resonance region. More recently, Vieira et al. (2018) conducted experiments on an FLNG and a small LNG carrier with a side-by-side configuration. The FLNG was equipped with six tanks that were filled with water. The test results indicated that the smaller LNG carrier had a minimum influence on motions of the larger FLNG; on the contrary, large motions of the LNG carrier were induced due to the presence of the FLNG. In addition, the free surface in the FLNG tanks amplified the surge, sway, and roll motions and increased the natural roll period. Dong et al. (2019) carried out experiments to investigate the dynamic gangway responses between a Tender Assisted Drilling (TAD) platform and a tension leg platform (TLP). In their study, the gangway responses were obtained from the global motions of the platforms.

The experiments mentioned above either fixed the bodies or utilized fenders and side-by-side mooring systems to restrain the ship models. To better understand the physics behind the two-body interaction problem, it is ideal to consider free-body motions and their interactions with free surfaces without fenders and side-by-side mooring systems. For example, Zhou et al. (2015) conducted model tests on two side-by-side box-like FPSOs at the towing tank of Memorial University (MUN). Both single body and two bodies with various gap distances were investigated, and strong interactions due to the existence of the second body were observed. In the following, the same models were applied by Qiu et al. (2017) to extend the measurements to drift forces on the bodies. In their work, more wave frequencies were tested in the resonance region, and extensive repeated tests were carried out for uncertainty analysis. Moreover, experiments were also conducted at the wave basin of Ecole Centrale de Nantes (ECN) to investigate tank wall effects.

The literature on experiments for ship underway replenishment is relatively sparse. McTaggart et al. (2003) conducted model tests on the replenishment of a frigate and a supply ship at a moderate speed in head waves. In their experiment, two configurations were considered: two ships parallel at midships and frigate ahead of the supply vessel. Maysam Mousaviraad et al. (2016) presented the experimental results on two side-by-side ships travelling in calm water and in waves with different headings. Effects on configuration, spacing, and speed were also investigated. More recently, model tests were performed by McTaggart et al. (2018) to validate the simulation of replenishment at sea. In their work, a destroyer was equipped with a propeller controller and freely maneuvering alongside a tanker in both calm water and random head waves.

1.1.2.2 Uncertainty analysis

High-quality experimental data requires thorough and comprehensive uncertainty analysis, which depends on detailed knowledge of the measurements, the measurement method, and the test procedure. Although many experimental data exist, as mentioned above, comprehensive uncertainty analysis is not reported in those studies. Since measurements are affected by many parameters in the two-body interaction tests, it is essential to understand and quantify those uncertainties in the measurements. In terms of uncertainty analysis of model test results, most of the work has been done based on the ISO-GUM methodology (ISO, 2008). For instance, Qiu et al. (2014) identified the parameters that may cause uncertainties in ocean engineering model tests. Uncertainty sources in the model tests were categorized in their work in terms of physical properties of the fluid, initial test conditions, model definition, environments, instrumentation, scaling, and human factors. The application of the ISO-GUM methodology to the seakeeping experiments was discussed by Kim and Hermansky (2014). The ITTC procedure on the uncertainty analysis for seakeeping tests (ITTC, 2014) is also based on ISO-GUM. More recently, Woodward et al. (2016) applied the ISO-GUM methodology to uncertainty analysis in the inclining experiments. A procedure, along with case studies, was presented to assess the uncertainties in centre of gravity and metacentric height. More recently, Qiu et al. (2019) performed a comprehensive uncertainty analysis on the two-body interaction model test data (Qiu et al., 2017). The sources of uncertainties in the two-body interaction model tests were identified, and a combined experimental and numerical approach was proposed to estimate uncertainties due to model geometry, model mass

properties, gap distance, and mooring set-up.

Besides the ISO-GUM methodology, other uncertainty analysis methods have been applied. For example, Irvine et al. (2008) conducted experiments on the coupled heave and pitch motions of a DTMB model 5512 in a towing tank to provide data for validation of CFD codes. In their work, the uncertainties in pitch and heave results were evaluated based on the ASME and AIAA standards, where the systematic bias, random precision limits, and their root-sum-squares were calculated.

1.2 Present Work

The present work focuses on the numerical and experimental studies on the hydrodynamic interaction between two floating bodies in close proximity. The main objectives of this thesis are summarized as follows:

Accurately predicting responses in the two-body interaction problem Linear potential-flow based seakeeping programs over-predict responses in the two-body interaction problem due to the ignorance of fluid viscosity. To investigate the viscous effects and to solve the large-amplitude body motions in the two-body interaction problem, a multi-phase finite-volume solver with an immersed-boundary method has been implemented in the OpenFOAM framework. The flow solver is applied to simulate two-body interactions in waves with and without forward speed.

Providing high-quality test data The available experiments on two-body interactions mainly apply fixed bodies or utilize fenders and side-by-side mooring systems to restrain the ship models. To better understand the physics behind the two-body

interaction problem, extensive model tests on two identical box-like FPSOs have been conducted, where the models undergo 6-DOF motions. Moreover, sources of uncertainties in the experiments are identified, and detailed uncertainty analysis on the test results is performed based on the ISO-GUM methodology. A combined experimental and numerical approach is developed to estimate the uncertainties due to model geometry, model mass properties, and test set-up.

Improving response prediction by potential-flow methods The hydrodynamic interactions between two bodies are also simulated using a frequency-domain potential-flow program, MAPS0, which is developed based on the panel-free method (Qiu et al., 2006). The results are compared with those from CFD simulations and model tests. Discrepancies in the predictions by MAPS0 for the zero-speed cases are analyzed, and a quasi-steady approach, which accounts for gap changes during interactions, is used to improve the simulations.

1.3 Thesis Outline

Chapter 1 introduces the two-body interaction problem and presents a review of previous studies in this field. The objectives of the present work and the outline of this thesis are then presented.

Chapter 2 gives detailed mathematical formulations of the present method, including N-S equation solver, immersed-boundary treatment, free surface capturing method, and numerical wave tank implementation. The approach to estimate uncertainties in the numerical results due to spatial discretization is also described.

In Chapter 3, details are given on the model tests of two box-like FPSO in head waves with zero forward speed. In the following, the sources of uncertainties in the present experiment are identified, and detailed uncertainty analysis on the test results along with detailed examples are presented.

Chapter 4 focuses on validation studies. Best practices on wave modelling are determined in the beginning. The present numerical method is then validated by simulating the present model tests for two-body interactions with zero forward speed. Validation studies are extended to simulations on ship underway replenishment for a frigate and a supply ship at a moderate forward speed. The uncertainty analysis of the numerical results is conducted for selected wave frequencies. The numerical results are compared with the experimental data and those from a potential-flow method.

In Chapter 5, this thesis ends with conclusions and future perspectives.

Chapter 2

Mathematical Formulations

2.1 Coordinate Systems

As shown in Fig. 2.1, two sets of coordinate systems are introduced. An earth-fixed Cartesian coordinate system, $OXYZ$, is employed with the OXY plane coinciding with the undisturbed free surface and the OZ axis pointing vertically upward. In the body-fixed coordinate systems, $o_i x_i y_i z_i$, $i = 1, 2$, o_i is the intersection point of the calm water surface, the centerplane of the ship and the vertical plane passing through the midsection; the $o_i z_i$ axis points upward; the $o_i x_i y_i$ plane coincides with the undisturbed free surface when the body is at rest; and the $o_i x_i$ axis points from the stern to the bow.

2.2 Governing Equations

The multi-phase incompressible viscous flow is governed by the momentum equations and the continuity equation:

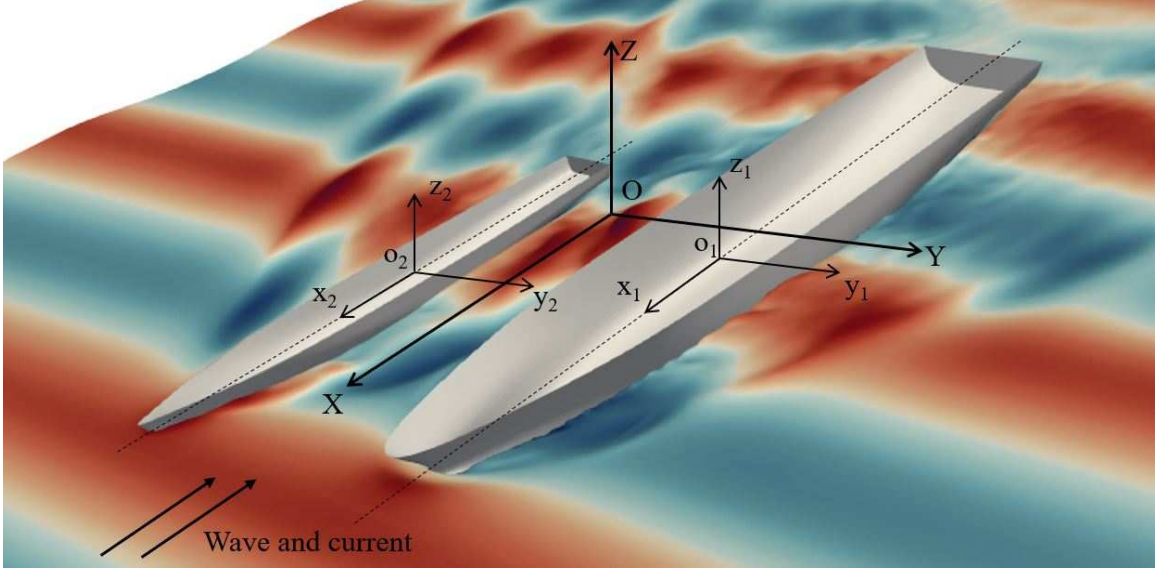


Figure 2.1: Coordinate Systems

$$\frac{\partial(\rho\mathbf{U})}{\partial t} + \nabla \cdot (\rho\mathbf{U}\mathbf{U}) - \nabla \cdot \mu\nabla\mathbf{U} - \nabla\mathbf{U} \cdot \nabla\mu = -\nabla p + \rho\mathbf{g} \quad (2.1)$$

$$\nabla \cdot \mathbf{U} = 0 \quad (2.2)$$

where \mathbf{U} is the fluid velocity, ρ is the density, μ is the dynamic viscosity, p is the pressure, and \mathbf{g} is the gravitational acceleration. Note that surface tension is not considered in the present work.

Introducing the dynamic pressure, $p_d = p + \mathbf{g} \cdot \mathbf{x}$, Eq. (2.1) can be expressed as follows,

$$\frac{\partial(\rho\mathbf{U})}{\partial t} + \nabla \cdot (\rho\mathbf{U}\mathbf{U}) - \nabla \cdot \mu\nabla\mathbf{U} - \nabla\mathbf{U} \cdot \nabla\mu = -\nabla p_d - \mathbf{g} \cdot \mathbf{x}\nabla\rho \quad (2.3)$$

where $\mathbf{x} = (x, y, z)$ is coordinate of a point in the flow field.

Prior to solving the governing equations, the transport equations for volume fractions of three phases, α_m , are solved based on the divergence-free velocity field com-

puted from the previous time step and motions of rigid bodies:

$$\frac{\partial \alpha_m}{\partial t} + \nabla \cdot (\mathbf{U} \alpha_m) = 0 \quad (2.4)$$

where $m = 1, 2$ and 3 represent water, air and solid phases, respectively. The density, ρ , and the dynamic viscosity, μ , are then calculated by:

$$\rho = \sum \alpha_m \rho_m \quad (2.5)$$

$$\mu = \sum \alpha_m \mu_m \quad (2.6)$$

2.3 Flow Solver

The governing equations are discretized using the finite volume method (FVM) on a collocated grid (Jasak, 1996). The linear upwind and linear schemes with second-order accuracy in space are applied to discretize the convection and diffusion terms in Eq. (2.3), respectively. The implicit Euler method with first-order accuracy in time is used for time advancing. The pressure implicit with splitting of operators (PISO) algorithm, developed by Issa (1986), is employed for the velocity-pressure coupling.

Denote the present time step as n , a semi-discretized form of Eq. (2.3) can be obtained:

$$A_P \mathbf{U}^n = A_H \mathbf{U}^n - \nabla p_d^n + S^n \quad (2.7)$$

where A_P and A_H are the diagonal and off-diagonal terms of the square coefficient matrix, A . A_H contains contributions from the discretized convection and diffusion terms, A_P contains contributions, in addition, from the unsteady term. S is the source term contributed by the unsteady term, the forcing term and the boundary conditions.

The pressure-correction scheme starts with a momentum prediction step by solving Eq. (2.7) using the pressure field from the previous time step, $n - 1$. A predicted velocity field \mathbf{U}^* is achieved, which is not divergence-free.

In what follows, a pressure-correction step is conducted to ensure that the velocity field \mathbf{U}^n satisfies the continuity equation, Eq. (2.2). Dividing both sides of Eq. (2.7) by A_P , and substituting \mathbf{U}^n on the RHS by the predicted velocity field, \mathbf{U}^* , the following expression is obtained

$$\mathbf{U}^n = \frac{A_H(\mathbf{U}^*)}{A_P} - \frac{\nabla p_d^n}{A_P} + \frac{S^n}{A_P} \quad (2.8)$$

Let $\mathbf{U}^{**} = \frac{A_H(\mathbf{U}^*)}{A_P} + \frac{S^n}{A_P}$, Eq. (2.8) can be rewritten as

$$\mathbf{U}^n = \mathbf{U}^{**} - \frac{\nabla p_d^n}{A_P} \quad (2.9)$$

Taking the divergence of both sides of Eq. (2.9), the equation reads

$$\nabla \cdot \mathbf{U}^n = \nabla \cdot \mathbf{U}^{**} - \nabla \cdot \left(\frac{\nabla p_d^n}{A_P} \right) \quad (2.10)$$

Applying the continuity equation, Eq. (2.2), the pressure Poisson equation is constructed as

$$\nabla \cdot \left(\frac{\nabla p_d^n}{A_P} \right) = \nabla \cdot \mathbf{U}^{**} \quad (2.11)$$

To avoid pressure oscillations on collocated grids, the Rhie-Chow interpolation (Rhie and Chow, 1983) is applied to solve Eq. (2.11), where the RHS of Eq. (2.11) is evaluated by using the Gauss theorem

$$\nabla \cdot \mathbf{U}^{**} = \frac{\sum \phi^{**}}{\Delta V} \quad (2.12)$$

where $\phi^{**} = \mathbf{U}_f^{**} \mathbf{S}$ is the flux on cell faces, \mathbf{U}_f is the velocity on cell faces obtained by a linear interpolation of the velocity stored at cell centres, \mathbf{S} is the face area vector and ΔV is the cell volume.

Finally, the velocity field is corrected with the newly solved pressure gradient using Eq. (2.9). The algorithm then proceeds to another pressure-correction step by assigning the corrected velocity field back to \mathbf{U}^* , i.e., repeating the steps from Eq. (2.8) to Eq. (2.12) until the desired number of iterations or the convergence criteria is met.

2.4 Immersed-boundary Treatment

As shown in Fig. 2.2, solid bodies are treated as a phase in the flow.

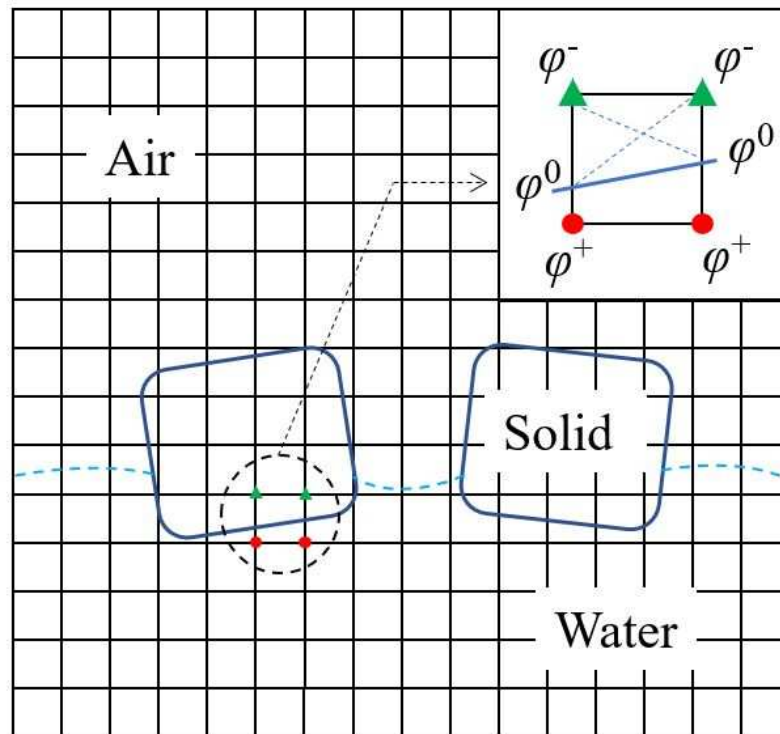


Figure 2.2: Three-phase Flow

No-flux and no-slip velocity boundary conditions are imposed on immersed bound-

aries and are enforced in each PISO loop before solving the Poisson equations for pressure. When a computational cell or face is cut by or lies within an immersed boundary, velocities at this location are obtained based on body motions and the volume fraction of the cell, α_3 , and the area fraction of the face, α_{3f} , of the solid phase, i.e.,

$$\mathbf{U}' = \alpha_3 \mathbf{U}_{IB} + (1 - \alpha_3) \mathbf{U} \quad (2.13)$$

$$\mathbf{U}'_f = \alpha_{3f} \mathbf{U}_{IBf} + (1 - \alpha_{3f}) \mathbf{U}_f \quad (2.14)$$

where \mathbf{U}_{IB} and \mathbf{U}_{IBf} are velocities at cell centre and cell face, respectively, obtained from the rigid-body motions, and \mathbf{U} and \mathbf{U}_f are solved from the governing equations.

The cell and face fractions for the solid phase are calculated geometrically. When a cell or a face is located inside of a rigid body, the corresponding volume and face fractions are set to one. When it is cut by an immersed boundary, the fractions are calculated by using a level-set function, $\varphi(\mathbf{x})$, which is defined on cell vertices based on the exact location of the immersed boundary. When a vertex lies in the solid region, $\varphi(\mathbf{x})$ is negative (see the green triangles in Fig. 2.2); otherwise positive (see the red filled circles in Fig. 2.2). The immersed boundaries are then determined at $\varphi(\mathbf{x}) = 0$. In other words, when values of $\varphi(\mathbf{x})$ at vertices of a cell or face are in different signs, it indicates that the cell or face is cut by an immersed boundary. Furthermore, the intersection points between an immersed boundary and cell edges are determined by linear interpolations. The fractions of the solid phase can then be calculated by decomposing the remaining cell or face into pyramids or triangles (see the zoomed part in Fig. 2.2) and by summing their corresponding fraction values.

2.5 Free-surface Capturing

The present research involves long time simulation to capture the nonlinear effects due to dynamic gap changes between two bodies. Therefore, it is crucial to apply a free-surface capturing scheme that preserves the sharp air-water interface and guarantees mass conservation. A geometric volume of fluid (VOF) algorithm, isoAdvector, proposed by Roenby et al. (2016) is utilized for the free-surface capturing.

To update the free surface, the convection equation for the water phase, α_1 , is solved from

$$\frac{\partial \alpha_1}{\partial t} + \nabla \cdot (\mathbf{U}\alpha_1) = 0 \quad (2.15)$$

where \mathbf{U} is the divergence-free velocity field.

In the FVM framework, integrate Eq. (2.15) over the control volume, V , and apply the Gauss theorem, the following expression is obtained:

$$\frac{\partial}{\partial t} \int_V \alpha_1 dV = - \int_V \nabla \cdot (\mathbf{U}\alpha_1) dV = - \int_S (\mathbf{U}_f \alpha_{1f}) d\mathbf{S} \quad (2.16)$$

where \mathbf{S} is the area vector pointing out of the control volume, \mathbf{U}_f and α_{1f} are the velocity and water phase fraction defined on the cell faces, respectively.

The water phase fraction is updated by calculating the total water volume transported across the cell faces during the time interval, $\Delta t = t^n - t^{n-1}$

$$\alpha_1^n = \alpha_1^{n-1} - \frac{1}{V} \sum_{j=1}^m \int_{t^{n-1}}^{t^n} \mathbf{U}_f(\tau) \alpha_{1f}(\tau) d\tau \mathbf{S}_m \quad (2.17)$$

where n denotes the current time step, and the control volume is enclosed by m faces.

In comparison to algebraic VOF methods, geometric VOF approaches are more accurate owing to the free-surface reconstruction step (Deshpande et al., 2012). In the present method, as shown in Fig. 2.3, the α_1 values stored at the cell centres

are first linearly interpolated to cell vertexes. For each cell with $0 < \alpha_1 < 1$, the interface, including the centroid, \mathbf{C} , and the orientation, \vec{n} , of it, as shown in Fig. 2.3, is constructed using an isoFace determined by the α_1 values defined on cell vertexes so that the geometrical volume fraction under the interface is equal to the corresponding α_1 value.

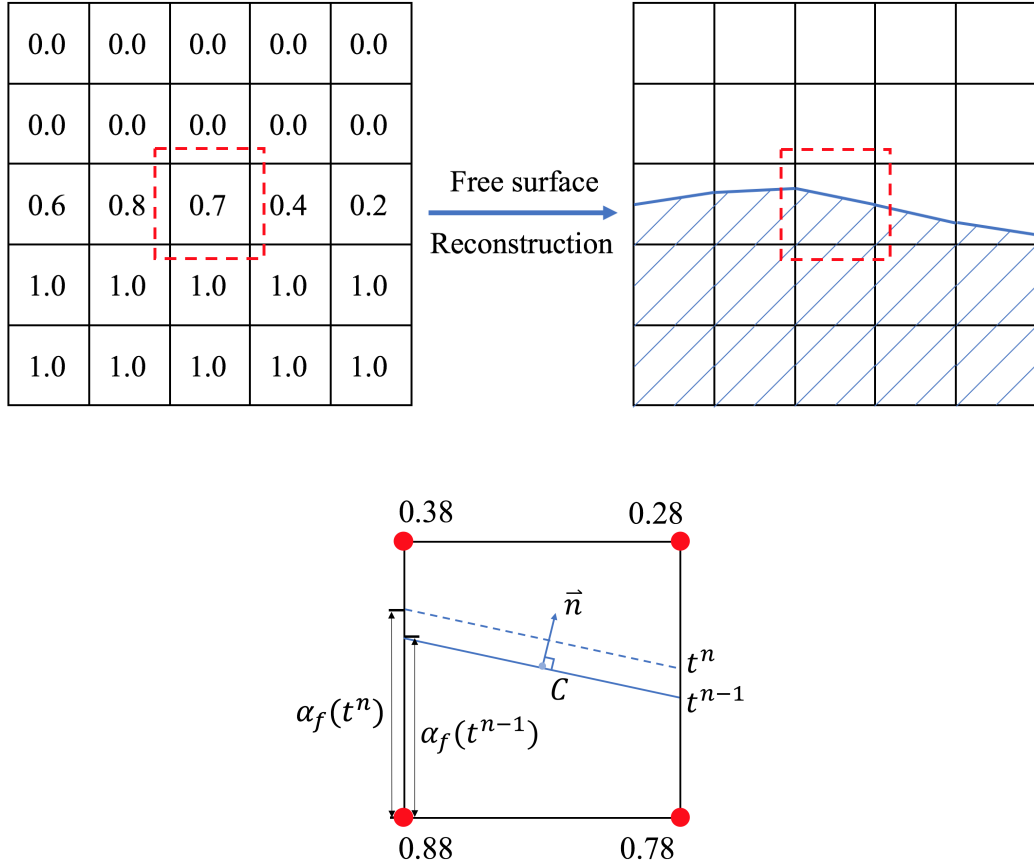


Figure 2.3: Free-surface Reconstruction and Advection

To obtain the water volume transported across the faces in Eq. (2.17), the movement of the interface during the time interval from t^{n-1} to t^n is also considered. Assume a constant velocity field within the time interval, i.e., $\mathbf{U}_f(\tau)$ is constant, the

motion of the interface from t^{n-1} to t^n is determined by, $u_n \Delta t$, where $u_n = \vec{u} \cdot \vec{n}$ is the normal velocity of the interface, \vec{u} is the velocity vector at the interface centroid, \mathbf{C} , interpolated from the divergence-free velocity field, and \vec{n} is the interface orientation (see Fig. 2.3). Further, the change of $\alpha_{1f}(\tau)$ in Eq. (2.17) during the time interval can be computed geometrically based on the movement of the interface (see Fig. 2.3). The integration in Eq. (2.17) can then be solved, therefore updating the α_1 field.

2.6 Numerical Wave Tank

A numerical wave tank is developed to simulate ship motions in waves, including wave modelling and rigid body dynamics. The toolbox, waves2Foam (Jacobsen et al., 2012), is used for wave generation and absorption. Inlet and outlet relaxation zones, proposed by Mayer et al. (1998) and shown in Fig. 2.4, are employed to avoid reflected waves from the wavemaker boundary and the outlet boundary.

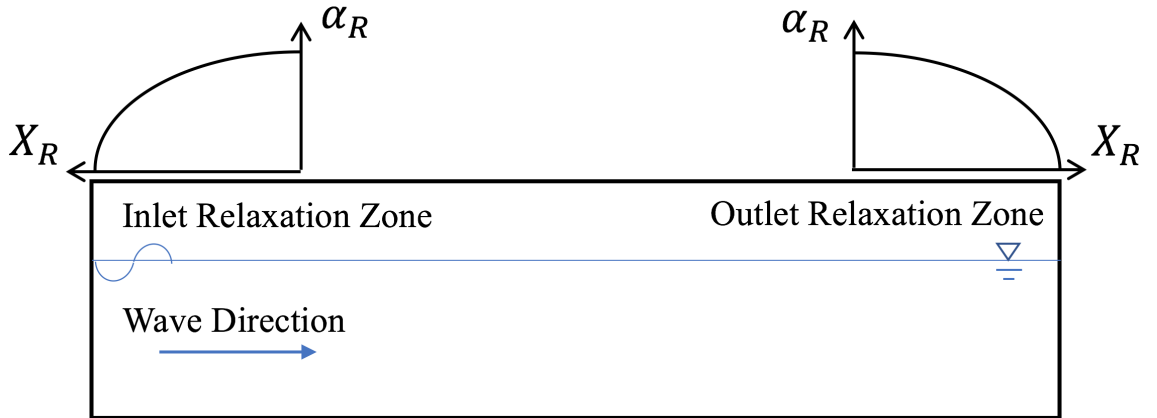


Figure 2.4: Relaxation Zones

In the relaxation zones, the explicit approach is applied, i.e., a quantity is explicitly

corrected after solving the flow field using the relaxation function, $\alpha_R(X_R)$:

$$\phi = \alpha_R \phi_{NS} + (1 - \alpha_R) \phi_w \quad (2.18)$$

where ϕ is a quantity, which can be the velocity, \mathbf{U} , or water volume fraction, α_1 ; ϕ_{NS} is the solution of N-S equations; and ϕ_w is the one obtained from the potential-flow based wave theory. It is noted that implicit relaxation methods exist, for example the work of Vukčević et al. (2016a,b).

The relaxation function, $\alpha_R(X_R)$, is defined as

$$\alpha_R(X_R) = 1 - \frac{e^{X_R^p} - 1}{e^1 - 1}, \quad X_R \in [0, 1] \quad (2.19)$$

where α_R ranges from zero to one and X_R is the normalized horizontal distance from a point in the relaxation zone to the boundary, and p is the spatial exponent set as 3.5 by default (Jacobsen et al., 2012).

The relaxation step is applied at the end of each time step after a divergence-free velocity field is achieved, i.e., the velocity and water volume fraction fields are modified explicitly using Eq. 2.18.

For problems involving a ship speed, U , a steady current is introduced in the relaxation zones, i.e., the computational mesh remains constant. In this case, the frequency of an incident wave, ω_0 , defined at the wave-maker boundary is replaced by the frequency of encounter, $\omega_e = \omega_0 - \omega_0^2/gU \cos \beta$, where β is the wave heading with $\beta = 180^\circ$ for head seas.

As for the motion solver, equations of motion are established according to the work of Danmeier (1999) and Qiu and Peng (2013). Denoting a column vector by braces $\{\}$, the translational displacements in the earth-fixed coordinate system, $OXYZ$ (see

Fig. 2.1), are represented by \mathbf{X} and the Eulerian angles are given by \mathbf{X}_R . The angular velocity in xyz (see Fig. 2.1) is denoted by $\boldsymbol{\omega}$. The time rate change of the Eulerian angles is related to the angular velocity by

$$\dot{\mathbf{X}}_R = \mathbf{T}\boldsymbol{\omega} = \begin{bmatrix} 1 & s_1 t_2 & c_1 t_2 \\ 0 & c_1 & -s_1 \\ 0 & s_1/c_2 & c_1/c_2 \end{bmatrix} \boldsymbol{\omega} \quad (2.20)$$

where $c_k = \cos(X_{3+k})$, $s_k = \sin(X_{3+k})$ and $t_k = \tan(X_{3+k})$ for $k=1, 2$ and 3 .

Equations of motion are then given as

$$\begin{bmatrix} \mathbf{m} & -m\mathbf{x}_{cg}\mathbf{D}^T \\ m\mathbf{x}_{cg}\mathbf{D} & \mathbf{I}_o \end{bmatrix} \begin{Bmatrix} \ddot{\mathbf{X}} \\ \dot{\boldsymbol{\omega}} \end{Bmatrix} = \begin{Bmatrix} \mathbf{F} \\ \mathbf{M}_o \end{Bmatrix} \quad (2.21)$$

where \mathbf{m} is the 3×3 matrix with the body mass, m , along its diagonal and zero everywhere else, \mathbf{I}_o is the mass moment of inertia matrix with respect to the origin, \mathbf{x}_{cg} is the centre of gravity, \mathbf{F} are the external forces, \mathbf{M}_o are the moment about the origin of the body-fixed coordinate system, and \mathbf{D} is the rotational transformation matrix between the earth-fixed and body-fixed coordinate systems as follows:

$$\mathbf{D} = \begin{bmatrix} c_2 c_3 & c_2 s_3 & -s_2 \\ s_1 s_2 c_3 - c_1 s_3 & s_1 s_2 s_3 + c_1 c_3 & s_1 c_2 \\ c_1 s_2 c_3 + s_1 s_3 & c_1 s_2 s_3 - s_1 c_3 & c_1 c_2 \end{bmatrix} \quad (2.22)$$

2.7 Evaluation of Uncertainties Due to Spatial Discretization

The Grid Convergence Index (GCI) method (Celik et al., 2008) is applied to estimate uncertainties due to spatial discretization. A summary of the method is provided

below.

Considering three sets of meshes with cell sizes, h_1 , h_2 and h_3 ($h_1 < h_2 < h_3$), numerical results, such as ship motions, wave elevations in the gap and drift forces, obtained using the three meshes are denoted as ϕ_1 , ϕ_2 and ϕ_3 , respectively. Introducing the refinement factors, $r_{21} = h_2/h_1$ and $r_{32} = h_3/h_2$, the apparent order, p , is calculated as

$$p = \frac{1}{\ln r_{21}} \ln |\epsilon_{32}/\epsilon_{21}| + \ln \left(\frac{r_{21}^p - s}{r_{32}^p - s} \right) \quad (2.23)$$

where $\epsilon_{32} = \phi_3 - \phi_2$, $\epsilon_{21} = \phi_2 - \phi_1$ and $s = \text{sgn}(\epsilon_{32}/\epsilon_{21})$. Equation 2.23 can be solved using the fixed-point iteration. It is noted that three convergence types are possible: $0 < \epsilon_{21}/\epsilon_{32} < 1$ for monotonic convergence, $\epsilon_{21}/\epsilon_{32} < 0$ for oscillatory convergence, and $\epsilon_{21}/\epsilon_{32} > 1$ for divergence. The extrapolated values are calculated by:

$$\phi_{ext}^{21} = \frac{r_{21}^k \phi_1 - \phi_2}{r_{21}^k - 1} \quad (2.24)$$

The approximate relative error and the extrapolated relative error are evaluated by

$$e_a^{21} = \left| \frac{\phi_1 - \phi_2}{\phi_1} \right| \quad (2.25)$$

$$e_{ext}^{21} = \left| \frac{\phi_{ext}^{21} - \phi_1}{\phi_{ext}^{21}} \right| \quad (2.26)$$

The uncertainty in the numerical results using the fine mesh with the smallest cell size due to spatial discretization is then estimated as

$$GCI_{fine}^{21} = \frac{1.25e_a^{21}}{r_{21}^p - 1} \quad (2.27)$$

Chapter 3

Model Tests and Uncertainty

Analysis of Two-body Interaction at Zero Speed

To validate the present numerical method, model tests on two side-by-side FPSO models in head waves have been conducted in the towing tank of Memorial University. The present experiment is based on the work of Zhou et al. (2015), with measurements extended to drift forces, more wave frequencies investigated in the resonance region and extensive repeated tests performed for uncertainty analysis. Details on the model tests are first presented. Sources of uncertainty in the experiment are then identified, and uncertainties in the test results are determined based on the ISO-GUM methodology (ISO, 2008). A combined experimental and numerical approach is developed to estimate the uncertainties due to model geometry and mass properties and experimental set-up.

3.1 Model Tests

Model tests of two identical box-like FPSO models, as shown in Fig. 3.1, were carried out in the towing tank of Memorial University. The tank is 58.0 m long, 4.6 m wide, and 1.8 m deep.

3.1.1 Experimental Set-up

The particulars of the ships and the scaled models are given in Table 3.1. The test matrix is presented in Table 3.2. The wave steepness was $1/30$. Each test case was repeated five times.



Figure 3.1: Ship Models in Waves

6-DOF motions of the two bodies, wave elevations in the gap between the two models and mean drift forces were measured. The experimental set-up is presented

Table 3.1: Particulars of full-scale bodies and models (1:60)

	Vessel 1	Vessel 2	Model 1	Model 2
<i>Length</i> (m)	120.0	120.0	1.997	1.998
<i>Breadth</i> (m)	24.0	24.0	0.397	0.397
<i>Depth</i> (m)	18.0	18.0	0.301	0.301
<i>Draft</i> (m)	6.0	6.0	0.103	0.104
Δ (kg)	1.64×10^7	1.64×10^7	76.6	76.6
<i>KG</i> (m)	7.68	7.56	0.128	0.126
<i>R_{xx}</i> (m)	7.02	7.08	0.117	0.118
<i>R_{yy}</i> (m)	28.02	28.92	0.467	0.482
<i>GM_T</i> (m)	3.24	3.18	0.054	0.053

Table 3.2: Test matrix for waves

No.	$\omega(rad/s)$	λ/L	No.	$\omega(rad/s)$	λ/L
1	3.90	2.03	10	6.09	0.83
2	4.27	1.69	11	6.22	0.80
3	4.65	1.43	12	6.41	0.75
4	4.96	1.25	13	6.53	0.72
5	5.09	1.19	14	6.66	0.69
6	5.34	1.08	15	6.79	0.67
7	5.53	1.01	16	6.91	0.65
8	5.72	0.94	17	7.04	0.62
9	5.91	0.88	18	7.16	0.60

in Fig. 3.2. The gap distance between the two bodies was 0.4 m. The wave probe, denoted as WP2, was positioned at 8.3 m from the wave board to measure the incoming waves. Three wave probes, WP4, WP5, and WP6, were positioned along the centre line of the gap. WP5 was in line with the mid-ship sections of the two models, and the spacing between these three wave probes was 0.5 m.

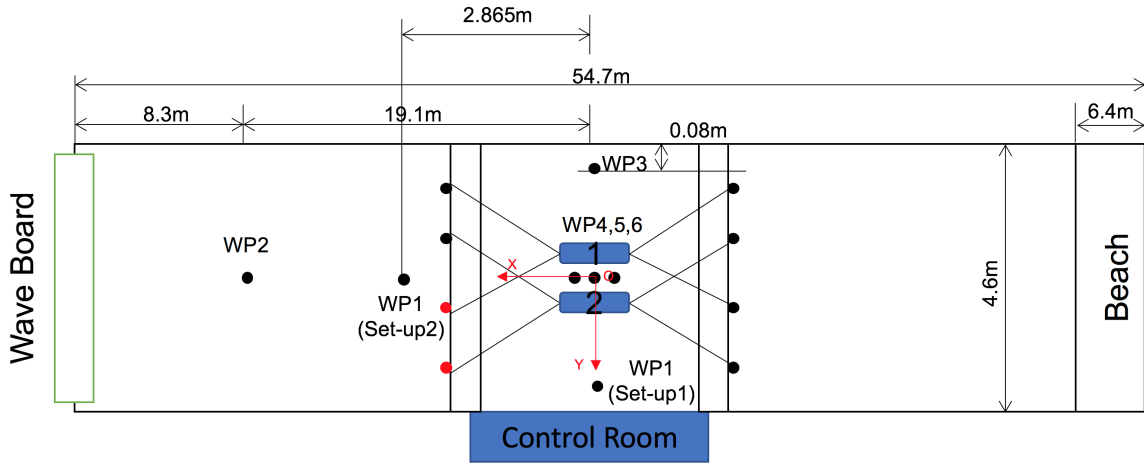


Figure 3.2: Experimental Set-up

For each model, four mooring lines comprised of springs and fishing lines were used to restrain the model from drifting, as shown in Fig. 3.3. At the end of each mooring line connected to the fixed platform, a load cell was installed to measure the in-line tension, hence the drift forces. The stiffness of each spring was 3.4 N/m, which was determined to meet the requirement by the ITTC procedure (ITTC, 2005), i.e., the natural period of the mooring system should be one order of magnitude greater than the maximum wave period in the tests. The mooring connection points on each model, which are identical at the bow and the stern, are shown in Fig. 3.4.

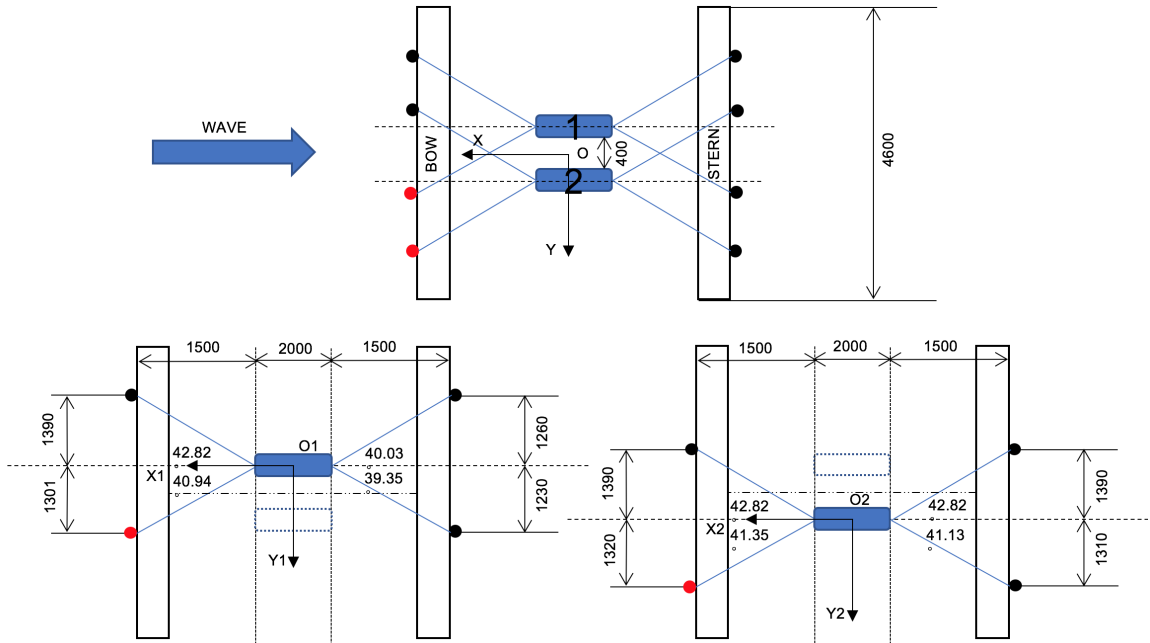


Figure 3.3: Mooring System Set-up

3.1.2 Instrumentation and Pre-tests

Motions of the two bodies were captured by the Qualisys system with three Oqus 3+ cameras, and a total of 10 and 11 markers were placed on the deck of Model 1 and Model 2, respectively. Wave elevations were measured by AWP-24 resistive wave height gauges. LFS 270-UW load cells were used to measure mooring line tensions. The NI9239 modules were utilized for data acquisition, and the PS-3330(3A) power supply was employed to provide constant input voltage (10 V) for the sensors.

Prior to the model tests, three repeated static calibrations were performed for each load cell with an input voltage of 10 V. For each calibration, ten constant load steps were taken, and the load was held constant for 30 seconds in each step, as shown in Fig. 3.5.

Similar to the calibration for load cells, the wave probes were calibrated by mea-

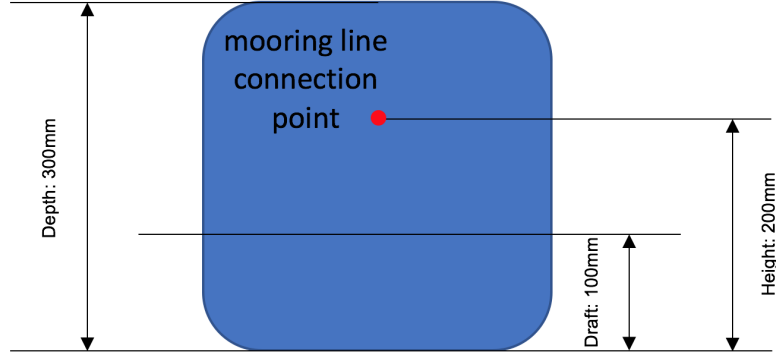


Figure 3.4: Mooring Line Connection Point on a Model

asuring the voltages when submerged in different water depths, and the input voltage is also 10 V. An example of the calibration results for WP5 is shown in Fig. 3.6.

During the tests, the Qualisys system was calibrated every week to ensure the accuracy of motion capturing. Calibration of the Qualisys system was done by using a calibration toolkit and a wand after the camera layout was established. The standard deviation of the wand length was obtained as an indication of the calibration quality. The wand length was 750 mm, and the deviation in each calibration was less than 1 mm. An example of the calibration report is shown in Fig. 3.7.

Wave calibrations were performed and repeated four times to obtain the reduction coefficient, β , between the wave amplitude at WP2, ξ_2 , and the incident wave amplitude at the model location, ξ_0 , as shown in Fig. 3.2.

Swing tests were conducted and repeated nine times to determine the vertical center of gravity and mass moments of inertia of the two models. In the tests, an electronic inclinometer and a stopwatch were used to measure inclining angles and swing periods, respectively. The set-up is illustrated in Fig. 3.8.

To obtain the location of center of gravity above keel, KG , a small weight was

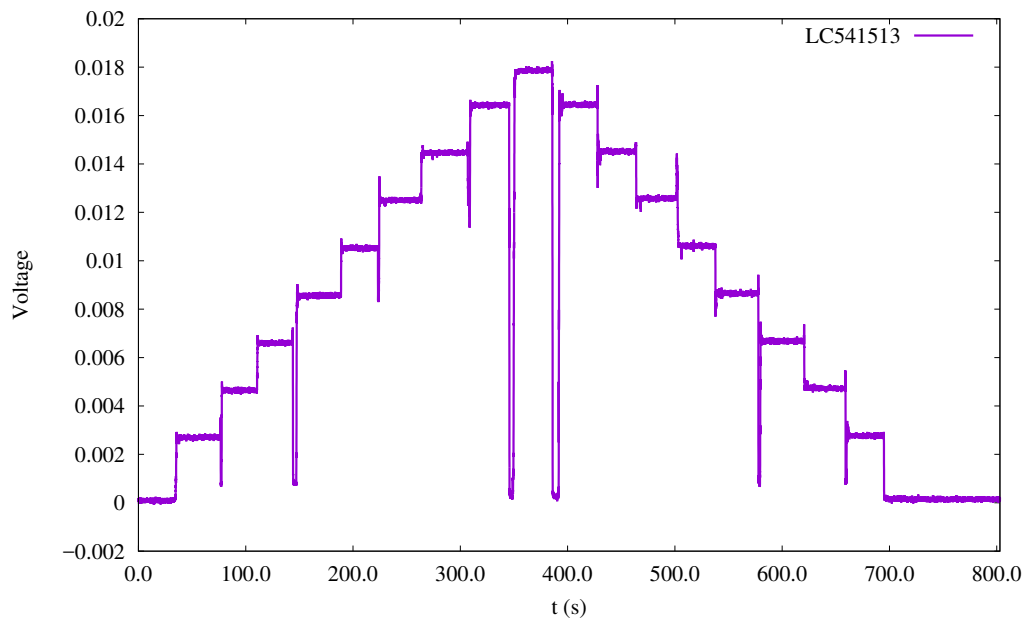


Figure 3.5: An Example of Load Cell Calibration Curve

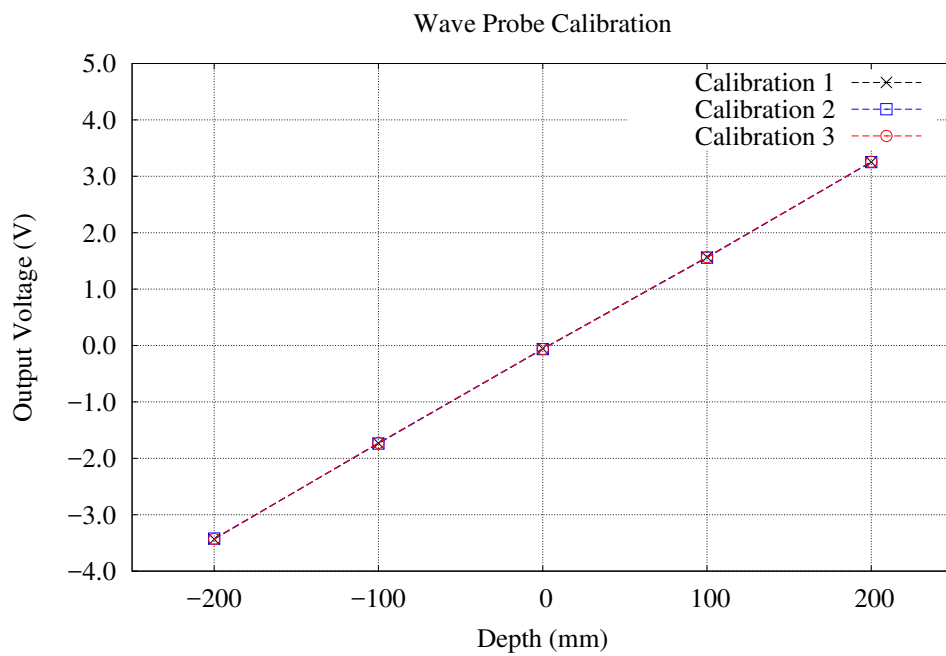


Figure 3.6: An Example of Wave Probe Calibration Curve

Calibration passed					
Camera results					
Id	X (mm)	Y (mm)	Z (mm)	Points	Avg res (mm)
01	-2725.91	410.75	3203.62	4665	0.61185
02	-2550.95	-1452.22	2996.10	5983	0.67676
03	-2565.55	-711.07	3229.14	6070	0.23535

Standard deviation of wand length: 0.83842 (mm)

Calibration carried out: 2015-10-13 16:10:29

Figure 3.7: An Example of the Qualisys System Calibration Report

applied on the weight hanging point (see Fig. 3.8), and the tilt angles caused by the weight were then measured. The KG value can be determined from

$$KG = d_0 - \frac{mL \cot \alpha - mL \cot \gamma}{M} \quad (3.1)$$

where m is the mass of the hanging weight, M is the mass of the model, and α and γ are the angles measured with and without the model on the swing frame, respectively.

The moments of inertia were obtained by applying a small initial tilt angle to the frame and recording the swing periods. The moment of inertia for roll about the pivot axis, I' , is then determined by

$$I' = J_T - J_F \quad (3.2)$$

where $J_T = \frac{T^2}{2\pi^2} m_T g OZ_T$ is the total inertia of the model and the frame and $J_F = \frac{T_0^2}{2\pi^2} m_F g OZ_F$ is the inertia of the frame. Note m_T and m_F are the total mass and frame mass, respectively; T_0 and T represent the oscillation period of the frame without and with the model, respectively; OZ_T and OZ_F are the distance from the knife edge to the total and frame centre of gravity, respectively. The moment of inertia about the

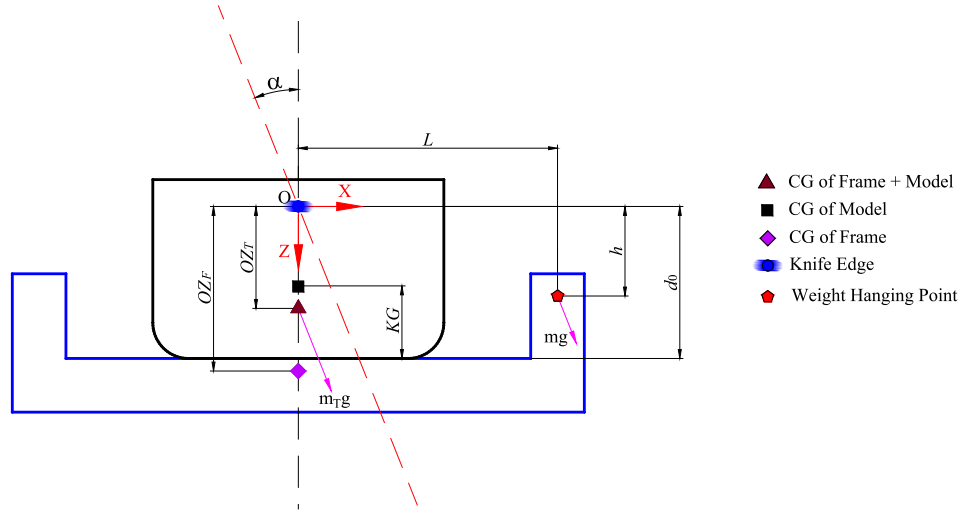


Figure 3.8: Swing Test Set-up

center of gravity, I , is given as

$$I = I' - M \cdot OG^2 \quad (3.3)$$

where OG is the distance from the knife edge to the centre of gravity of the model.

3.1.3 Experimental Data Processing

Fast Fourier Transform (FFT) analysis was applied to obtain body motions and wave elevations. Motions of the models were taken into account in determining the mooring line forces at each time step.

Since the motion data and the mooring line tension data were recorded using two different computers, a post-synchronization process was applied in order to consider the instantaneous lengths of mooring lines and positions of the mooring connection points on the models.

Denoting the translational motions as $\mathbf{T}(t)$ and the rotational motions as $\mathbf{R}(t)$, the

position of a mooring connection point on a model as \mathbf{x}_m in the body-fixed coordinate system and as $\mathbf{X}_m(t)$ in the earth-fixed coordinate system, $\mathbf{X}_m(t)$ can be obtained from

$$\mathbf{X}_m(t) = [M(t)]\mathbf{x}_m + \mathbf{T}(t) \quad (3.4)$$

where $[M(t)]$ is the transformation matrix. Note that the body-fixed coordinate systems and the earth-fixed coordinate system are shown in Fig. 3.3.

The length $L(t)$ and the direction $\mathbf{d}(t)$ of each mooring line at each time step can then be calculated by

$$L(t) = |\mathbf{X}_m(t) - \mathbf{X}_p| \quad (3.5)$$

$$\mathbf{d}(t) = \frac{\mathbf{X}_m(t) - \mathbf{X}_p}{|\mathbf{X}_m(t) - \mathbf{X}_p|} \quad (3.6)$$

where \mathbf{X}_p is the position vector of the fixed mooring connection point on the platform of the towing tank.

The longitudinal and transverse components of the mooring tension at each time step were calculated based on the instantaneous direction of a mooring line and the measured line tension. The mean drift forces were then obtained by subtracting the tare values from the mean tension values, which were measured when the models were stationary and in steady-state oscillations, respectively.

3.2 Uncertainty Analysis

The uncertainty analysis on the model test results, including 6-DOF motions, wave elevations in the gap between the two models, and drift forces, are conducted based on the ISO-GUM methodology (ISO, 2008). A combined experimental and numerical

method is proposed to evaluate the uncertainties due to model geometry, model mass properties, gap distance, and mooring set-up.

According to the categories presented in the work of Qiu et al. (2014), the main uncertainty sources in two-body model tests are identified and listed in Table 3.3.

3.2.1 Uncertainty Analysis Method

The ISO-GUM methodology (ISO, 2008) was adopted for the uncertainty analysis. The uncertainty analysis procedure is summarized as below.

The Type A standard uncertainty is calculated from the repeated measurements according to Eq. (3.7), and the Type B standard uncertainty is obtained based on scientific judgment and experience.

$$u(\bar{q}) = \left[\frac{1}{n(n-1)} \sum_{j=1}^n (q_j - \bar{q})^2 \right]^{\frac{1}{2}} \quad (3.7)$$

where q_j is the j th independent observation of the n measurements and \bar{q} is the mean value.

When a quantity y under investigation is not measured directly, but calculated from N other measurements, x_1, x_2, \dots, x_N , based on a relationship, $y = f(x_1, x_2, \dots, x_N)$, the combined standard uncertainty of y , denoted as $u_c(y)$, is calculated by applying the law of propagation of uncertainty:

$$u_c(y) = \left[\sum_{i=1}^N \left(\frac{\partial f}{\partial x_i} \right)^2 u^2(x_i) \right]^{\frac{1}{2}} \quad (3.8)$$

where $u(x_i)$ is the Type A or Type B standard uncertainty of x_i , and $\frac{\partial f}{\partial x_i}$ is the sensitivity coefficient.

Table 3.3: Sources of uncertainties in the two-body interaction tests

Category	Uncertainty source elements
Physical properties of the fluid	Viscosity and temperature
Initial test conditions	Remaining waves
Model	Model dimensions
	Centre of gravity
	Mass and moments of inertia
	Mooring system
Wave generation	Wave board control
	Wave absorber
	Tank dimensions
Instrumentation	Load cells
	Wave probes
	Qualisys system
	Power supply
	AD converter
Scaling	Viscous effect
Human factors	Set-up of mooring system
	Model position and orientation
	Sensor installation

Multiplying the combined uncertainty by a coverage factor k , the expanded uncertainty is obtained as

$$u_e(y) = ku_c(y) \quad (3.9)$$

where k is obtained from the level of confidence and the effective degree of freedom, ν_{eff} , which is calculated using the Welch-Satterthwaite formula:

$$\nu_{eff} = \frac{u_c^4(y)}{\sum_{i=1}^N \frac{u_i^4(y)}{\nu_i}} \quad (3.10)$$

where the degree of freedom ν_i is $n - 1$ for n repetitions for Type A analysis. In the present work, ν_i is equal to 4 for five repeated tests.

As for Type B analysis, ν_i can be estimated by using the relative uncertainty

$$\nu_i = \frac{1}{2} \left[\frac{\Delta u(x_i)}{u(x_i)} \right]^{-2} \quad (3.11)$$

from experience or judgment based on the available information. In Eq. (3.11), $\Delta u(x_i)$ is the uncertainty of $u(x_i)$. If $u(x_i)$ is exactly known, ν_i is infinity. By adopting a confidence level (95% in the present work), the coverage factor k can then be determined (ISO, 2008).

3.2.2 Uncertainty Analysis of the Measurements

The results of two-body interaction tests are presented in terms of non-dimensional forms. The non-dimensional motions of a model, x'_{ij} , $i = 1, \dots, 6$, $j = 1, 2$ (two bodies), wave elevation at a location, ξ'_k , $k = 1, \dots, 6$ (WP1 to WP6), and the drift forces on the j th model, F'_{lj} , $l = 1, 2$ (longitudinal and transverse directions), are given as follows:

$$x'_{ij} = f_1(\bar{x}_{ij}, \bar{\xi}_0) = \frac{\bar{x}_{ij}}{\bar{\xi}_0}, \quad i = 1, 2, 3 \quad (3.12)$$

$$x'_{ij} = f_2(\bar{x}_{ij}, \bar{\xi}_0) = \frac{\bar{x}_{ij}}{k_w \bar{\xi}_0}, \quad i = 4, 5, 6 \quad (3.13)$$

$$\xi'_k = f_3(\bar{\xi}_k, \bar{\xi}_0) = \frac{\bar{\xi}_k}{\bar{\xi}_0} \quad (3.14)$$

$$F'_{lj} = f_4(\bar{F}_{lj}, \rho, g, \bar{\xi}_0, L_j) = \frac{\bar{F}_{lj}}{\frac{1}{4}\rho g \bar{\xi}_0^2 L_j} \quad (3.15)$$

where k_w is the wave number, \bar{x}_{ij} , $\bar{\xi}_k$, \bar{F}_{lj} and $\bar{\xi}_0$ are the mean motion, wave elevation, drift force and incident wave amplitude, respectively, which were obtained from repeated tests, and L_j is the length of Model j .

Uncertainties of these non-dimensional values can be obtained according to the uncertainty analysis methodology summarized in the previous section. The Type A standard uncertainties of the measured quantities, x_{ij} , ξ_k , F_{lj} and ξ_0 , were calculated according to Eq. (3.7).

The Type A combined uncertainties of the non-dimensional values are given as

$$u_{x'_{ij}A}^2 = \left(\frac{1}{\bar{\xi}_0}\right)^2 u_{x_{ij}A}^2 + \left(-\frac{\bar{x}_{ij}}{\bar{\xi}_0^2}\right)^2 u_{\xi_0A}^2, \quad i = 1, 2, 3 \quad (3.16)$$

$$u_{x'_{ij}A}^2 = \left(\frac{1}{k_w \bar{\xi}_0}\right)^2 u_{x_{ij}A}^2 + \left(-\frac{\bar{x}_{ij}}{k_w \bar{\xi}_0^2}\right)^2 u_{\xi_0A}^2, \quad i = 4, 5, 6 \quad (3.17)$$

$$u_{\xi'_kA}^2 = \left(\frac{1}{\bar{\xi}_0}\right)^2 u_{\xi_kA}^2 + \left(-\frac{\bar{\xi}_k}{\bar{\xi}_0^2}\right)^2 u_{\xi_0A}^2 \quad (3.18)$$

$$u_{F'_{lj}A}^2 = \left(\frac{1}{\frac{1}{4}\rho g \bar{\xi}_0^2 L_j}\right)^2 u_{F_{lj}A}^2 + \left(-\frac{2\bar{F}_{lj}}{\frac{1}{4}\rho g \bar{\xi}_0^3 L_j}\right)^2 u_{\xi_0A}^2 \quad (3.19)$$

The Type B standard uncertainties were obtained from the instrumentation calibrations, manufacturer's specifications, and scientific judgments, as discussed in the following sections. The Type B combined uncertainties are calculated as follows:

$$u_{x'_{ij}B}^2 = \left(\frac{1}{\bar{\xi}_0}\right)^2 u_{x_{ij}B}^2 + \left(-\frac{\bar{x}_{ij}}{\bar{\xi}_0^2}\right)^2 u_{\xi_0B}^2, i = 1, 2, 3 \quad (3.20)$$

$$u_{x'_{ij}B}^2 = \left(\frac{1}{k_w \bar{\xi}_0}\right)^2 u_{x_{ij}B}^2 + \left(-\frac{\bar{x}_{ij}}{k_w \bar{\xi}_0^2}\right)^2 u_{\xi_0B}^2, i = 4, 5, 6 \quad (3.21)$$

$$u_{\xi'_k B}^2 = \left(\frac{1}{\bar{\xi}_0}\right)^2 u_{\xi_k B}^2 + \left(-\frac{\bar{\xi}_k}{\bar{\xi}_0^2}\right)^2 u_{\xi_0 B}^2 \quad (3.22)$$

$$u_{F'_{lj}B}^2 = \left(\frac{1}{\frac{1}{4}\rho g \bar{\xi}_0^2 L_j}\right)^2 u_{F_{lj}B}^2 + \left(-\frac{2\bar{F}_{lj}}{\frac{1}{4}\rho g \bar{\xi}_0^3 L_j}\right)^2 u_{\xi_0B}^2 + \left(-\frac{\bar{F}_{lj}}{\frac{1}{4}\rho g \bar{\xi}_0^2 L_j^2}\right)^2 u_{L_jB}^2 \quad (3.23)$$

The Type B standard uncertainties were determined explicitly and implicitly from the sources illustrated in Fig. 3.9.

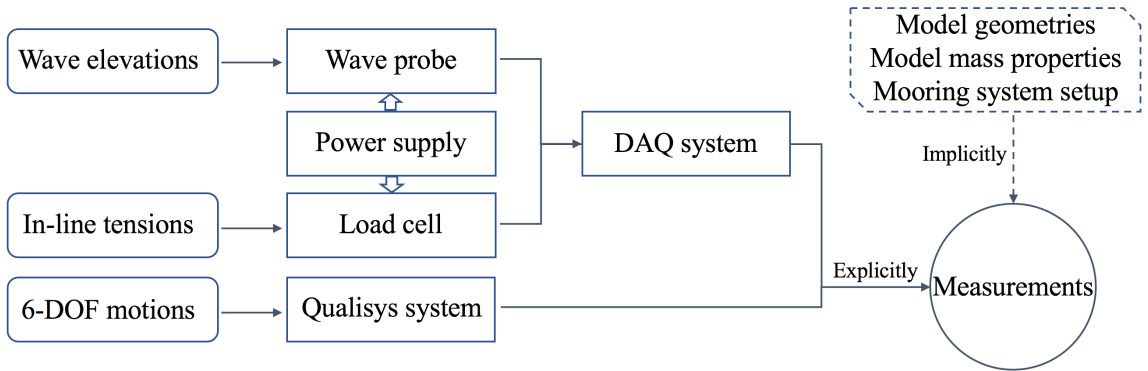


Figure 3.9: Type B Uncertainty Sources

Uncertainties due to sensors were obtained from calibrations. Uncertainties contributed by the power supply and the data acquisition (DAQ) system were evaluated based on the manufacturer’s specifications. Uncertainties due to model geometry, mass properties, and mooring setup were assessed based on numerical simulations. Sources of uncertainties, as shown in Fig. 3.9, are further categorized in Table 3.4 in terms of calibrations, u_{CB} , manufacturer’s specifications, u_{MB} , and numerical simulations, u_{NB} . The assessment of these sources will be discussed in the later sections.

The Type B standard uncertainty of a measurement, u_B , can then be calculated as

$$u_B^2 = u_{CB}^2 + u_{MB}^2 + u_{NB}^2 \quad (3.24)$$

Based on Table 3.4, the corresponding sources for Type B standard uncertainties for all the measurements are presented in Table 3.5.

3.2.3 Type B Uncertainties Determined from Pre-tests

Uncertainties determined from calibrations, u_{CB} , such as those due to wave probes, load cells, and the Qualisys system, are discussed in this section. Prior to the experiments, wave probes and load cells were calibrated to establish the relationship between the input (voltage) to the measurement system and the physical output values (wave height or tension). The calibration data were then used to assess the uncertainties due to hysteresis, linearity, and repeatability (Figliola and Beasley, 2011).

It should be noted that the degree of freedom, ν_i , used in Eq. (3.10) was identified as infinity for uncertainties determined from calibrations. In the calibrations for wave probes and load cells, the values to be measured are within the calibration range, i.e.,

Table 3.4: Sources of Type B uncertainty included in the calculations

Item	Sources	
Calibrations, u_{CB}	Wave probe calibration, u_{CWP}	Linearity, u_{linear}
		Repeatability, u_{repeat}
	Wave calibration, u_{CW}	Repeat tests, u_{CW}
	Load cell calibration, u_{CLC}	Linearity, u_{linear}
		Hysteresis, u_{hyster}
Repeatability, u_{repeat}		
Specifications, u_{MB}	Qualisys system, u_{QS}	RMS noise, u_{QS}
	DAQ system, u_{DAQ}	Gain, u_{gain}
		Noise, u_{noise}
	Power supply, u_{ps}	Load regulation, u_{load}
		Line regulation, u_{line}
Noise, u_{noise}		
Numerical Simulations, u_{NB}	Model, u_{model}	Geometry, $u_{geometry}$
		Mass properties, u_{mass}
	Mooring system, u_{moor}	Spring stiffness, u_{stiff}
		Spring layout, u_{layout}

the probability of these values outside the calibration range is basically zero and ν_i is, therefore, infinity according to Eq. (3.11). The same degree of freedom was applied to uncertainties due to the Qualisys system.

Table 3.5: Sources of Type B uncertainty considered in the calculations

Measurement	Item	Sources
Incident wave amplitude, $u_{\xi_0 B}$	Calibrations, u_{CB}	Wave probe calibration, u_{CWP} Wave calibration, u_{WC}
	Specifications, u_{MB}	DAQ system, u_{DAQ} Power supply, u_{ps}
Wave amplitudes in the gap, $u_{\xi_k B}$	Calibrations, u_{CB}	Wave probe calibration, u_{CWP}
	Specifications, u_{MB}	DAQ system, u_{DAQ} Power supply, u_{ps}
	Numerical, u_{NB}	Model, u_{model} Mooring system, u_{moor}
6-DOF motions amplitudes, $u_{x_{ij} B}$	Calibrations, u_{CB}	Qualisys system, u_{QS}
	Numerical, u_{NB}	Model, u_{model} Mooring system, u_{moor}
Drift forces, $u_{F_{ij} B}$	Calibrations, u_{CB}	Load cell calibration, u_{CLC}
	Specifications, u_{MB}	DAQ system, u_{DAQ} Power supply, u_{ps}
	Numerical, u_{NB}	Model, u_{model} Mooring system, u_{moor}

3.2.3.1 Uncertainties from load cell calibration

Static calibrations were performed for the load cells, and each calibration was repeated three times. The calibration results of the load cell installed on the mooring line on the port side of the bow of Model 1 is shown in Fig. 3.10. Note that the weight was

measured using a digital scale with a precision of 0.001 kg.

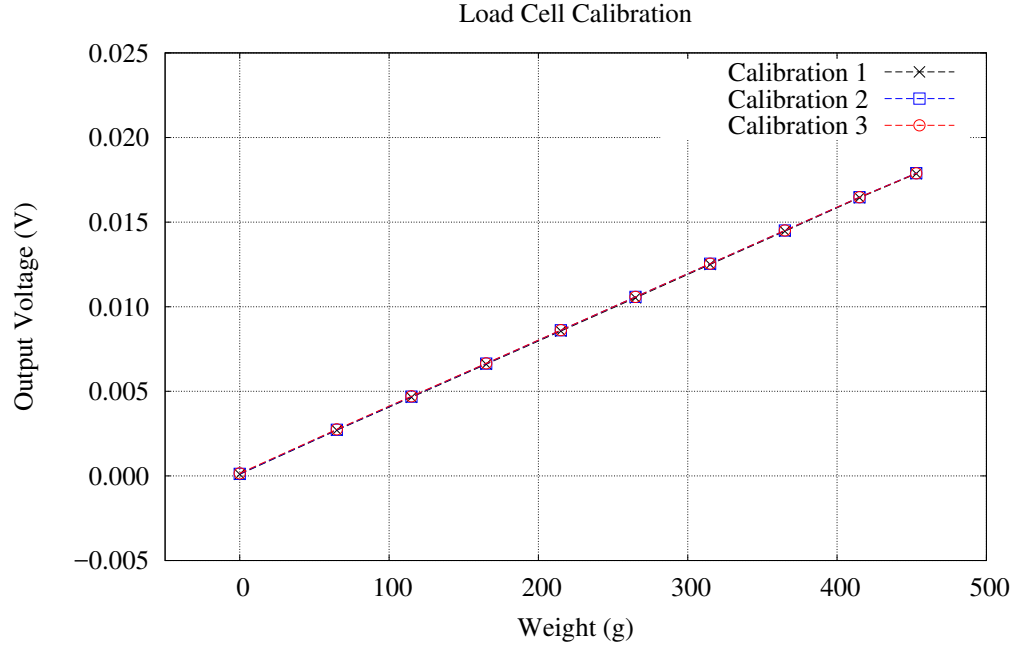


Figure 3.10: Load Cell Calibration Curve

According to the ITTC procedure on the calibration of load cells (ITTC, 2002), uncertainties due to linearity, hysteresis, and repeatability were obtained as below:

$$u_{linear} = \frac{\Delta\theta_L}{\theta_N} F_R \quad (3.25)$$

$$u_{hyster} = \frac{\Delta\theta_H}{\theta_N} F_R \quad (3.26)$$

$$u_{repeat} = \frac{\Delta\theta_R}{\theta_N} F_R \quad (3.27)$$

where $\Delta\theta_L$ is the maximum value of the deviation between the mean advance curve

and the straight line of two mean end points; $\Delta\theta_H$ is the maximum value of the deviation between the return mean calibration curve and the advance calibration curve; $\Delta\theta_R$ is the maximum value of the output range at each load point during the repeated calibration; θ_N is the rated output; and F_R is the rated load (ITTC, 2002). The overall uncertainty from calibration was then calculated by:

$$u_{CLC}^2 = u_{linear}^2 + u_{hyster}^2 + u_{repeat}^2 \quad (3.28)$$

As an example, the calibration uncertainties and sensitivities of load cells on the mooring lines connected to Model 1 are presented in Table 3.6, where M1 and M2 denote the two mooring lines on the port and starboard sides of the bow, respectively; M3 and M4 are those at the stern. The sensitivities, i.e., the physical calibration (input) range divided by the output range, were further used to calculate the uncertainties due to the DAQ system.

Table 3.6: Uncertainties determined from calibrations of load cells

Load Cell	u_{linear}	u_{hyster}	u_{repeat}	u_{CLC}	Sensitivity
	(N)	(N)	(N)	(N)	(N/mV)
LC M1	0.018	0.019	0.015	0.030	0.250
LC M2	0.017	0.025	0.052	0.060	0.444
LC M3	0.019	0.013	0.047	0.052	0.464
LC M4	0.014	0.016	0.031	0.026	0.453

3.2.3.2 Uncertainties from wave probe calibration

Similar to the calibrations of load cells, wave probes were calibrated by measuring the voltages when they were submerged in different water depths. The submerged depth was marked on the wave probe and measured with a measuring tape in a precision of 0.001 m. The linearity and repeatability uncertainties were taken into account in the calculation of the total uncertainty:

$$u_{CWP}^2 = u_{linear}^2 + u_{repeat}^2 \quad (3.29)$$

The uncertainties and sensitivities of wave probes are presented in Table 3.7.

Table 3.7: Uncertainties determined from calibrations of wave probes

No.	u_{linear} (mm)	u_{repeat} (mm)	u_{CWP} (mm)	sensitivity (mm/mV)
WP2	1.146	0.771	1.381	0.058
WP4	1.363	0.526	1.461	0.067
WP5	1.481	2.416	2.834	0.051
WP6	0.719	1.016	1.245	0.064

3.2.3.3 Uncertainties from the Qualisys system calibration

As mentioned in the previous section, the Qualisys system was calibrated using a calibration toolkit and a wand, and the standard deviation of the wand length was obtained to indicate the calibration quality (wand length: 750 mm, deviation: < 1 mm).

The actual uncertainties in the 6-DOF motion measurements depend on the quality of the tracking system, the size of markers, the quality and the number of markers, model location, and orientation, etc. Imperfect visual capture of the reflective markers may lead to “jumps” in their 3-D positions and thus influence the measured 6-DOF motions. To quantify the uncertainties from the Qualisys system, u_{QS} , time series of 6-DOF motions of the two models were recorded for 15 s before activating the wave board in each test. As the models were not exactly stationary due to the remaining waves from previous tests, model motions were filtered, and the differences between the measured and filtered data were used to calculate the RMS noise, as shown in Fig. 3.11. The RMS values of noises for all test runs were averaged and used as the uncertainties of the Qualisys system, u_{QS} . Table 3.8 presents the corresponding uncertainties for two models. Note that 10 and 11 markers were placed on Model 1 and Model 2, respectively.

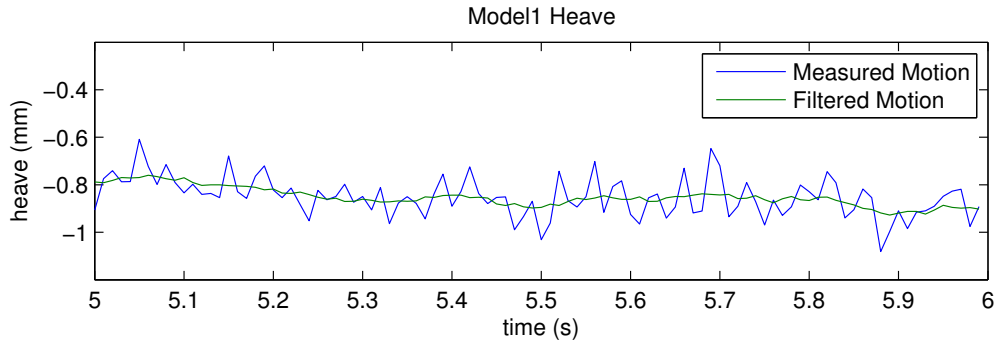


Figure 3.11: Noise in Heave Motion of Model 1

Table 3.8: Uncertainties of the Qualisys system for two models

Model	Surge (mm)	Sway (mm)	Heave (mm)	Roll (degree)	Pitch (degree)	Yaw (degree)
1	0.080	0.062	0.077	0.018	0.005	0.001
2	0.084	0.059	0.078	0.017	0.004	0.001

3.2.3.4 Uncertainties from wave calibration

Wave calibrations were performed to obtain the reduction coefficient, β , between the wave amplitude at WP2, ξ_2 , and the incident wave amplitude at the model location, ξ_0 , as shown in Fig. 3.2.

$$\xi_0 = \beta \xi_2 \quad (3.30)$$

The uncertainty from wave calibration, u_{CW} , was calculated from four repeated calibrations in a Type A manner:

$$u_{CW}^2 = \left(\frac{1}{\bar{\xi}_0}\right)^2 u_{\xi_2}^2 + \left(-\frac{\bar{\xi}_2}{\bar{\xi}_0^2}\right)^2 u_{\xi_0}^2 \quad (3.31)$$

where $\bar{\xi}_0$ and $\bar{\xi}_2$ are the mean wave amplitudes, and u_{ξ_0} and u_{ξ_2} are the standard uncertainties determined from repeated measurements.

3.2.3.5 Uncertainties from swing tests

Swing tests were performed to determine the vertical center of gravity and mass moments of inertia of the two models. Detailed description of the tests are presented in Section 3.1.

Uncertainties in all the quantities associated with the swing tests are listed in Table 3.9, where the Type A uncertainties were calculated from the nine repeated

measurements and the Type B ones were obtained based on the accuracy of the measuring instrument. For measurements such as the frame dimensions, the uncertainty was half of the smallest increment of the measuring tape (0.5 mm). Uncertainties in tilt angles measured by the inclinometer and in oscillation periods recorded by the stopwatch were 0.1° and 0.001 s, respectively. Uncertainties in masses of the model and the frame measured by the tension scale were 0.01 kg, and the uncertainty in the mass of the hanging weight measured by a digital scale was 0.001 kg. Note that the uncertainty in the total mass of the frame and the model was obtained from their individual uncertainties.

Table 3.9: Uncertainties in the swing tests (Model 1)

Quantity (Unit)	Type A	Type B
Tilt angle for roll, frame only, γ (degree)	0.0201	0.1
Tilt angle for roll, frame + model, α (degree)	0.0250	0.1
Oscillation period for roll, frame only, T_0 (s)	0.00246	0.001
Oscillation period for roll, frame + model, T (s)	0.00715	0.001
Oscillation period for pitch, frame only, T_{P0} (s)	0.0148	0.001
Oscillation period for pitch, frame + model, T_P (s)	0.0777	0.001
Model mass, M (kg)	-	0.01
Swing frame mass, m_F (kg)	-	0.01
Total mass, m_T (kg)	-	0.0141
Hanging weight mass, m (kg)	-	0.001
Frame dimensions, L, d_0, h (m)	-	0.0005

The Type A combined uncertainty of KG , u_{KGA} , is obtained by considering the uncertainty of the two angles, α and γ :

$$u_{KGA}^2 = \left(\frac{\partial KG}{\partial \alpha}\right)^2 u_{\alpha_A}^2 + \left(\frac{\partial KG}{\partial \gamma}\right)^2 u_{\gamma_A}^2 \quad (3.32)$$

where u_{α_A} and u_{γ_A} are the Type A standard uncertainties of the measured angles.

To calculate the Type B combined uncertainty of KG , uncertainties of mass and frame dimensions were also taken into account as below:

$$\begin{aligned} u_{KGB}^2 = & \left(\frac{\partial KG}{\partial \alpha}\right)^2 u_{\alpha_B}^2 + \left(\frac{\partial KG}{\partial \gamma}\right)^2 u_{\gamma_B}^2 + \left(\frac{\partial KG}{\partial m}\right)^2 u_{mB}^2 \\ & + \left(\frac{\partial KG}{\partial M}\right)^2 u_{MB}^2 + \left(\frac{\partial KG}{\partial L}\right)^2 u_{LB}^2 + \left(\frac{\partial KG}{\partial d_0}\right)^2 u_{d_0B}^2 \end{aligned} \quad (3.33)$$

where u_{α_B} and u_{γ_B} , u_{mB} and u_{MB} , and u_{LB} and u_{d_0B} are the Type B standard uncertainties of the measured angles, masses, and frame dimensions, respectively.

Similar to KG , the Type A combined uncertainty of the roll or pitch radius of gyration, r , can be derived from the uncertainties of periods, T and T_0 :

$$u_{rA}^2 = \left(\frac{\partial r}{\partial T}\right)^2 u_{TA}^2 + \left(\frac{\partial r}{\partial T_0}\right)^2 u_{T_0A}^2 \quad (3.34)$$

where u_{TA} and u_{T_0A} are the Type A standard uncertainties of the recorded periods with and without the model, respectively.

The Type B combined uncertainty of a radius of gyration is given as

$$\begin{aligned} u_{rB}^2 = & \left(\frac{\partial r}{\partial \alpha}\right)^2 u_{\alpha_B}^2 + \left(\frac{\partial r}{\partial \gamma}\right)^2 u_{\gamma_B}^2 + \left(\frac{\partial r}{\partial m}\right)^2 u_{mB}^2 \\ & + \left(\frac{\partial r}{\partial M}\right)^2 u_{MB}^2 + \left(\frac{\partial r}{\partial L}\right)^2 u_{LB}^2 + \left(\frac{\partial r}{\partial d_0}\right)^2 u_{d_0B}^2 \\ & + \left(\frac{\partial r}{\partial T}\right)^2 u_{TB}^2 + \left(\frac{\partial r}{\partial T_0}\right)^2 u_{T_0B}^2 + \left(\frac{\partial r}{\partial h}\right)^2 u_{hB}^2 \\ & + \left(\frac{\partial r}{\partial m_T}\right)^2 u_{m_TB}^2 + \left(\frac{\partial r}{\partial m_F}\right)^2 u_{m_FB}^2 \end{aligned} \quad (3.35)$$

where u_{TB} and u_{T_0B} , u_{mTB} and u_{mFB} , and u_{hB} are the Type B standard uncertainties of the measured periods, masses, and frame dimensions, respectively.

As a summary, the measurements and associated uncertainties are presented in Table 3.10. Note that the radius of gyration in yaw, r_z , and its uncertainty were assumed to be the same as those in pitch.

Table 3.10: Summary of swing test results (KG and radii of gyration) for Model 1

Parameter (unit)	KG	Roll r_{x1}	Pitch r_{y1}
Experimental results (m)	0.128	0.118	0.467
Type A combined uncertainty, u_{cA} (mm)	0.203	0.994	11.960
Type A effective DOF, ν_{effA}	13.448	9.483	8.224
Type A coverage factor, k_A	2.150	2.244	2.299
Type A expanded uncertainty, u_{eA} (mm)	0.436	2.231	27.492
Type B combined uncertainty, u_{cB} (mm)	1.304	2.327	13.635
Type B effective DOF, ν_{effB}	∞	∞	∞
Type B coverage factor, k_B	1.960	1.960	1.960
Type B expanded uncertainty, u_{eB} (mm)	2.555	4.560	26.724

3.2.4 Type B Uncertainties Evaluated from Manufacturer's Specifications

The Type B uncertainties due to the power supply and the DAQ system are presented in this Section. When the information from specifications is used, the associated

degree of freedom, ν_i , was identified as infinity. The standard uncertainty should be the specified uncertainty from the manufacturer divided by the coverage factor k (ISO, 2008). With a confidence level of 95%, the coverage factor k was determined as 1.960. Note that the noise uncertainty is Type A, and the specified value could be used directly as the standard uncertainty (Braudaway, 2003).

3.2.4.1 Uncertainties from DAQ system

The NI9239 modules were used in the data acquisition of wave elevations and in-line tensions. Following the uncertainty evaluation method for DAQ devices discussed in the work of Braudaway (2003), the specification provided by the manufacturer and sources of uncertainty are listed in Table 3.11.

Table 3.11: Uncertainties in DAQ system from specifications

Source of uncertainty	Manufacturer's specification	Standard uncertainty
Gain, u_{gain}	0.13 % of reading	0.066 % of reading
Noise, u_{noise}	70 μ V RMS	0.070 mV

Note: Range 10.52 V

Note that offset was not considered in the analysis since it was removed by subtracting the tare values from the signals of wave elevation and in-line tension.

The standard uncertainty due to noise, u_{noise} , was used to obtain the uncertainty of a measurement based on the sensitivity of a sensor listed in Tables 3.6 and 3.7. For example, the sensitivity of the wave probe, WP2, is 0.058 mm/mV. Multiplying it by u_{noise} (0.070 mV), the uncertainty of the wave elevation due to the noise of the

DAQ system is then obtained as 0.004 mm.

3.2.4.2 Uncertainties from power supply

The PS-3330(3A) power supply was used to provide a steady input voltage of 10 V for the wave probes and load cells. Uncertainties due to the power supply are listed in Table 3.12.

Table 3.12: Uncertainties in power supply from specifications

Source of uncertainty	Manufacturer's specification	Standard uncertainty
Load regulation, u_{load}	0.25 % + 3 mV	0.143 % of reading
Line regulation, u_{line}	0.025 % + 2 mV	0.023 % of reading
Noise, u_{noise}	0.5 mV RMS	0.005 % of reading
Total, u_{ps}	-	0.145 % of reading

The load regulation indicates the voltage variations on the output level caused by the change of load on sensors connected to the power supply. The line regulation is caused by the non-ideal input of AC line power.

For strain gauge load cells and resistive wave probes, the change of input voltage will lead to the same percentage of change in output voltage. Furthermore, the relationship between the physical measurement and the output voltage of a sensor is linear (see Fig. 3.10 as an example). Therefore, the uncertainty of measurement due to the power supply can be estimated based on the uncertainty of the input voltage in a percentage. Knowing the input voltage was 10 V, the percentage can then be determined from manufacturer's specifications listed in Table 3.12.

3.2.5 Type B Uncertainties Estimated from Numerical Simulations

Uncertainties contributed by model geometries, mass properties, mooring spring stiffness, and mooring layout were estimated from numerical simulations using the potential-flow frequency-domain Motion Analysis Program Suite (MAPS0), developed based on the panel-free method (Qiu et al., 2006). Since the solutions from MAPS0 are linear, the uncertainty in response due to a small change in a parameter, such as model length, can be evaluated based on the finite difference method described in the following section.

As mentioned in Chapter 1, the potential-flow based seakeeping programs over-predict the wave elevations in the gap and the drift forces in the resonance region. Artificial free-surface damping can be used to suppress the over-predictions. To avoid introducing unknown uncertainties due to artificial damping to numerical simulations, viscous roll damping and artificial free-surface damping were not applied in the computations by MAPS0.

3.2.5.1 Uncertainties due to model geometries

In the two-body interaction model tests, a measurement X can be expressed as follows:

$$X = f(L_1, B_1, D_1, L_2, B_2, D_2, S_{others}) \quad (3.36)$$

where X can be motions, wave elevations or drift forces; L , B and D are the model length, beam and draft, respectively; and S_{others} are parameters other than the principle dimensions of the models.

According to the experience of model construction at Memorial University, the uncertainty in CNC machining is five-thousandths of an inch or 0.127 mm. Extra glue and fiberglass layers also contributed to the overall uncertainty in model geometry. Table 3.1 presents the Type B uncertainties in model particulars.

By considering one uncertainty source, for example, the model length, and keeping the others unchanged, the corresponding 6-DOF motions, wave elevations in the gap and drift forces can be computed from MAPS0. Denoting the length of Model 2 as L_2 , the longitudinal drift force on Model 1, F_{11} , is affected by L_2 and other parameters such as beam, draft, the center of gravity, and mass properties, etc., i.e., $F_{11}^0 = f(L_2, \text{others})$. Introducing the length uncertainty, u_{L_2} , and

$$F_{11}^+ = f(L_2 + u_{L_2}, \text{others})$$

$$F_{11}^- = f(L_2 - u_{L_2}, \text{others})$$

the uncertainty in F_{11} due to u_{L_2} can be evaluated by

$$u_{F_{11}} = \frac{F_{11}^+ - F_{11}^0}{2} + \frac{F_{11}^0 - F_{11}^-}{2} \quad (3.37)$$

Note that other parameters remain unchanged when changing L_2 in numerical simulations.

For illustration, uncertainties in surge motions of Model 1 due to the change of model length, uncertainties in wave elevation in the gap at WP4 due to the change in the model beam, and uncertainties in the longitudinal mean drift force on Model 1 due to uncertainties in the draft are presented in Figs. 3.12 - 3.14, respectively. The vertical axis on the left indicates the non-dimensional values of surge, wave elevation, and longitudinal mean drift force, while the right one (in red) represents the corresponding uncertainty values. For example, the two red dashed and dash-dot-

dot lines in Fig. 3.12 denotes the uncertainties in surge motions due to uncertainties in the lengths of Models 1 and 2, respectively. Their corresponding values can be read from the right vertical axis.

From the simulation results, it can be seen that the uncertainty of a response, X , i.e., motion, wave elevation or drift force, due to the uncertainty in geometry, $u_{Xgeometry}$, is very small. Note that $u_{Xgeometry}$ is given as

$$u_{Xgeometry}^2 = u_{XL_1}^2 + u_{XB_1}^2 + u_{XD_1}^2 + u_{XL_2}^2 + u_{XB_2}^2 + u_{XD_2}^2 \quad (3.38)$$

where u_{XL_j} , u_{XB_j} and u_{XD_j} denote the Type B uncertainties of X due to the uncertainties of the length, beam and draft of Model j , $j = 1, 2$, respectively.

3.2.5.2 Uncertainties due to model mass properties

Similar to Eq. (3.36), a response X can be affected by model mass properties,

$$X = f(KG_1, r_{x1}, r_{y1}, r_{z1}, KG_2, r_{x2}, r_{y2}, r_{z2}, S_{others}) \quad (3.39)$$

where rs denote radii of gyration, KGs are the centres of gravity, and S_{others} represents parameters other than mass properties of a model.

Uncertainties in model mass properties were obtained from the swing test results listed in Table 3.10. The numerical results show that the roll motion is the most affected response by uncertainties in the mass properties of a model. Fig. 3.15 and 3.16 present roll motions and their uncertainties due to uncertainties in KG and roll radius of gyration. As shown in the figures, uncertainties in KG_1 and r_{x1} led to uncertainty of 5%-10% in roll motion of Model 1.

The uncertainty in a response due to uncertainties in model mass properties,

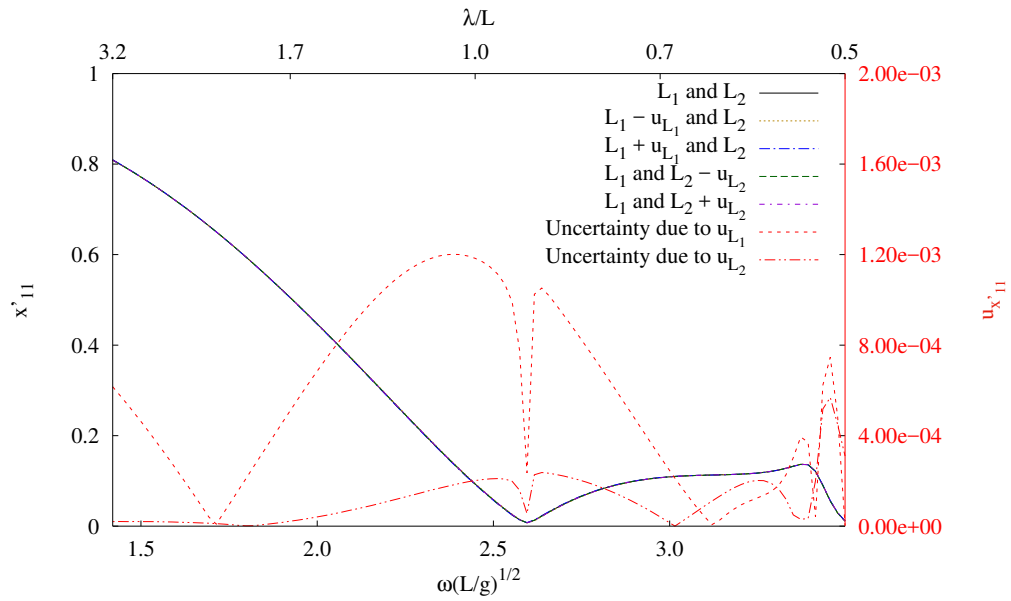


Figure 3.12: Surge of Model 1 due to Uncertainties in Model Length

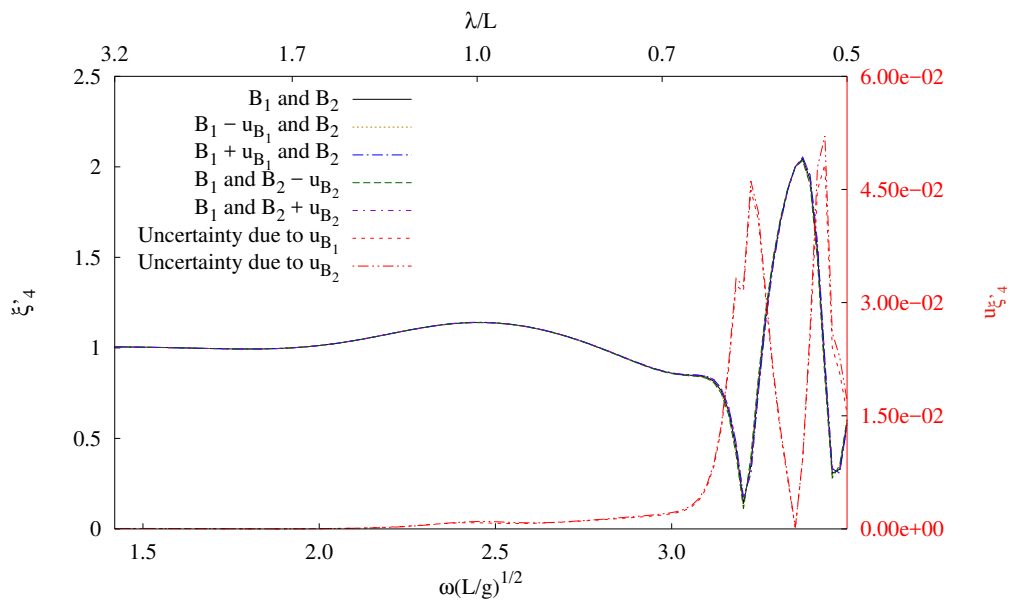


Figure 3.13: Wave Elevation at WP4 due to Uncertainties in Model Breadth

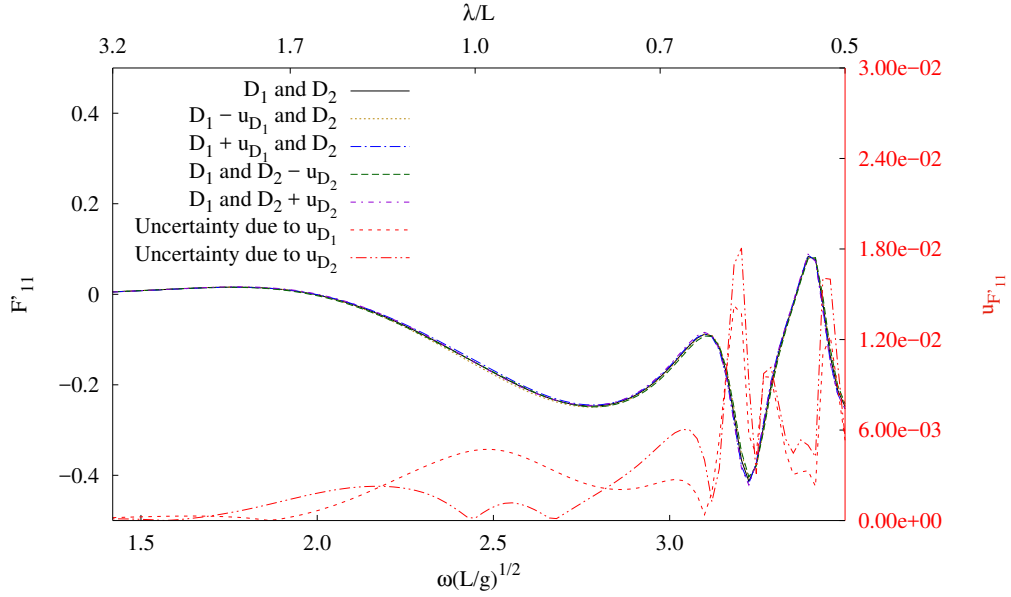


Figure 3.14: Longitudinal Mean Drift Force on Model 1 due to Uncertainties in Model Draft

$u_{X_{mass}}$, is calculated as

$$u_{X_{mass}}^2 = u_{X_{KG_1}}^2 + u_{X_{r_{x1}}}^2 + u_{X_{r_{y1}}}^2 + u_{X_{r_{z1}}}^2 + u_{K_{G_2}}^2 + u_{X_{r_{x2}}}^2 + u_{X_{r_{y2}}}^2 + u_{X_{r_{z2}}}^2 \quad (3.40)$$

where $u_{X_{KG_j}}$, $u_{X_{r_{xj}}}$, $u_{X_{r_{yj}}}$ and $u_{X_{r_{zj}}}$ are the Type B uncertainties of X due to the uncertainties in the vertical centre of gravity and the radii of gyration in roll, pitch and yaw of Model j , $j = 1, 2$, respectively.

3.2.5.3 Uncertainties due to mooring set-up

Four soft mooring lines were used for each model to restrain the model from drifting. The stiffness of the spring for each mooring line was selected in such a way that the natural period of the mooring system is one order of magnitude greater than

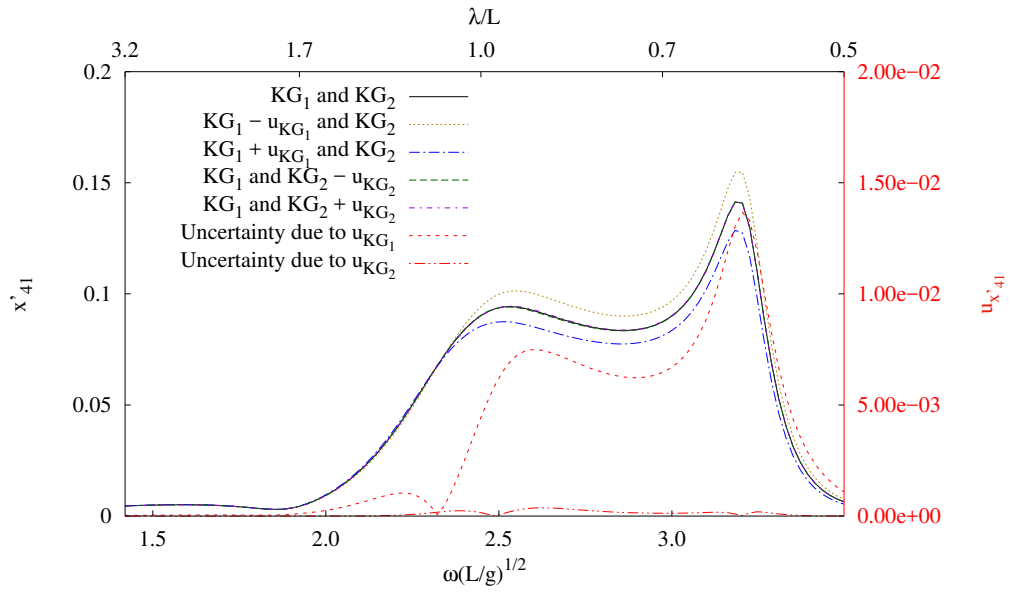


Figure 3.15: Roll of Model 1 due to Uncertainties in KG

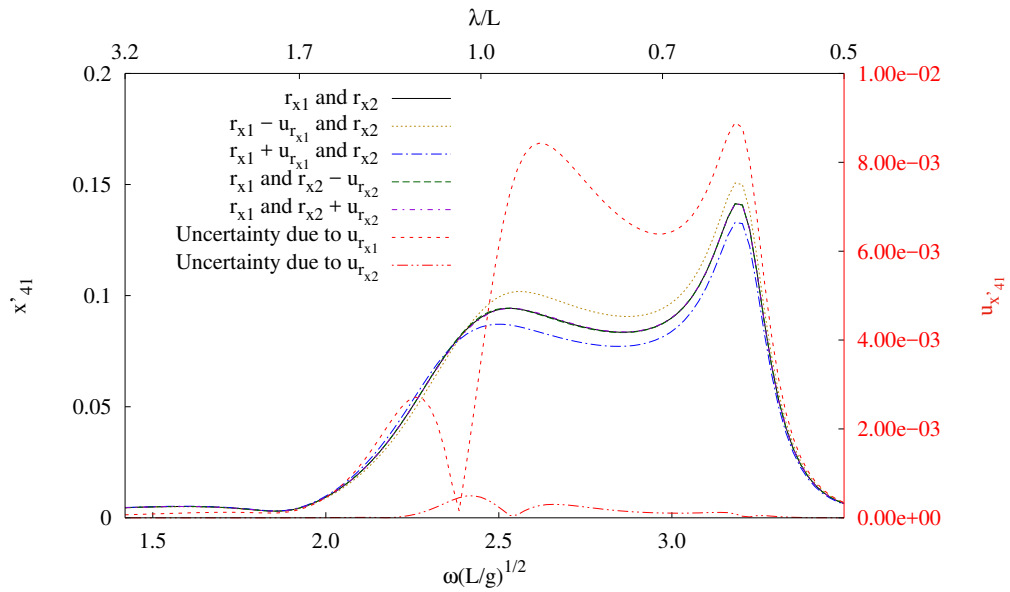


Figure 3.16: Roll of Model 1 due to Uncertainties in Roll Radius of Gyration

the highest wave period in the tests. From the calibrations, the stiffness of the spring was 3.45 ± 0.02 N/m. Similar to the approach used in the determination of uncertainties due to geometry and model mass properties, uncertainties in the mooring system in terms of mooring stiffness and gap width were also determined from numerical simulations. Fig. 3.17 presents the uncertainty in transverse mean drift force due to the uncertainty in the stiffness of the mooring line. It can be seen that the uncertainties due to mooring stiffness are negligible.

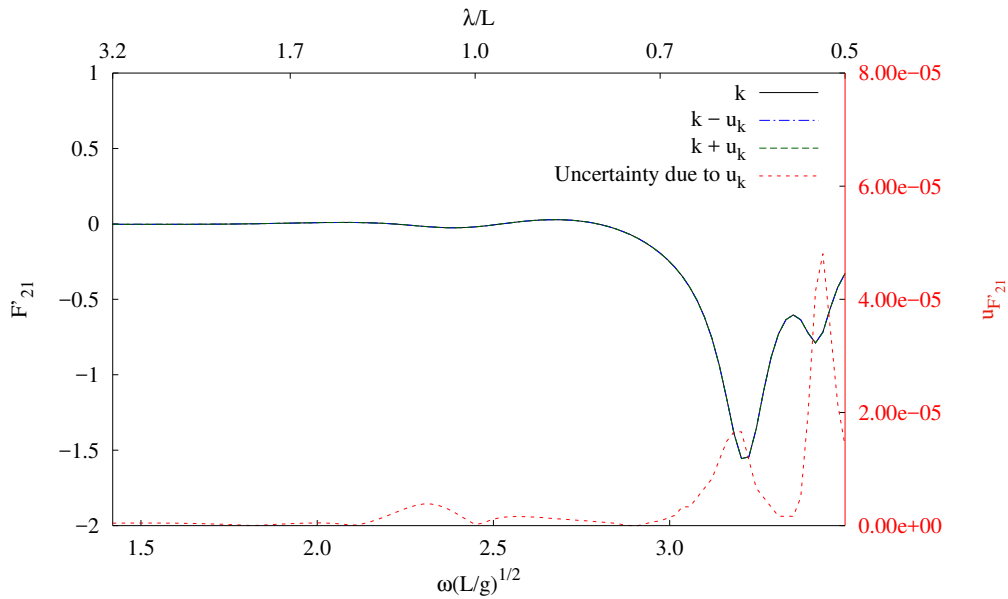


Figure 3.17: Transverse Mean Drift Force on Model 1 due to Uncertainty in Mooring Stiffness

The mooring layout affects the gap width and further leads to uncertainties in responses. Figs. 3.18 - 3.20 present heave, wave elevation at WP4, and the longitudinal drift force due to uncertainties in gap width.

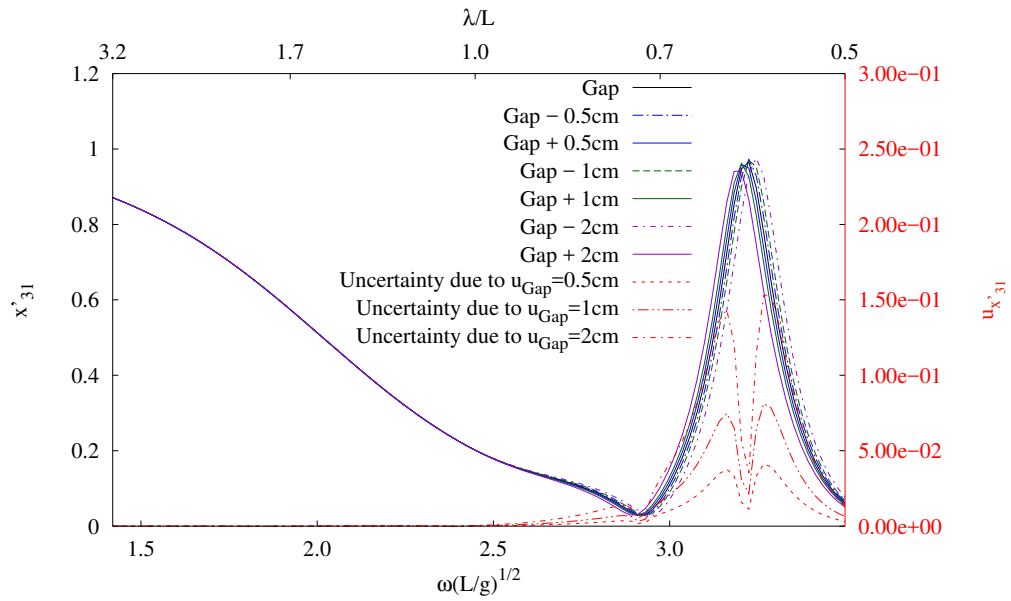


Figure 3.18: Heave of Model 1 due to Uncertainties in Gap Width

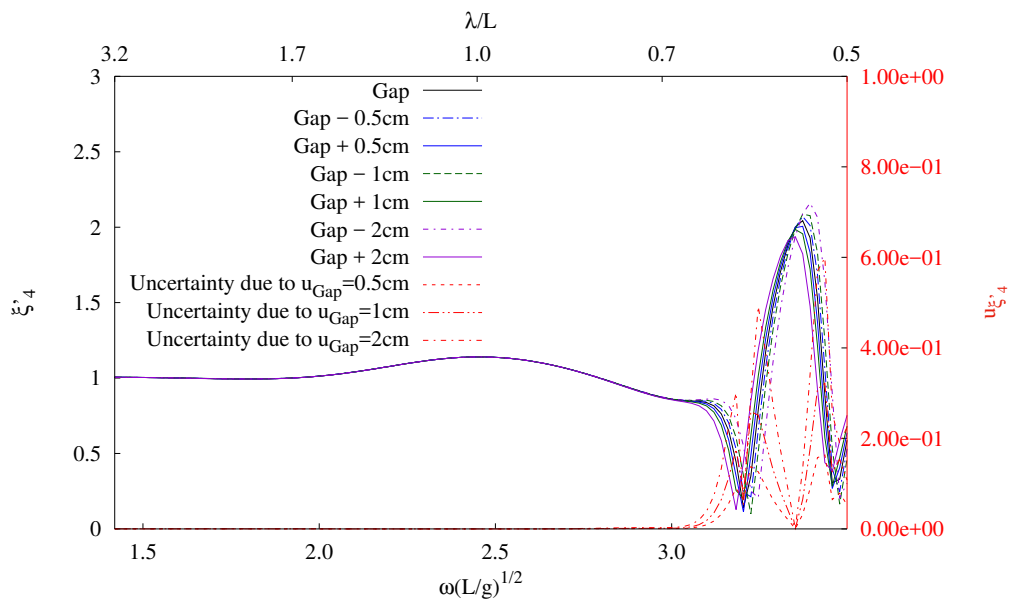


Figure 3.19: Wave Elevation at WP4 due to Uncertainties in Gap Width

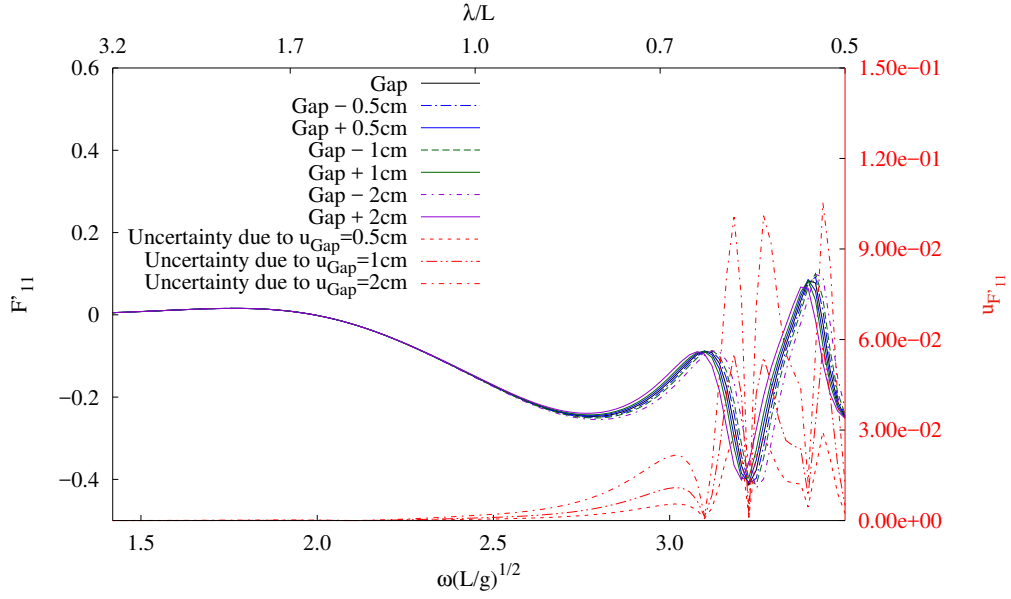


Figure 3.20: Longitudinal Mean Drift Force on Model 1 due to Uncertainties in Gap Width

It can be seen from the results that larger uncertainties due to gap occur near the resonance. The uncertainty of the gap in the test was identified as 0.005 m, and uncertainties due to the mooring system, u_{Xmoor} , can be expressed as

$$u_{Xmoor}^2 = u_{Xstiff}^2 + u_{Xlayout}^2 \quad (3.41)$$

where u_{Xstiff} and $u_{Xlayout}$ are the Type B uncertainties of X due to the uncertainties in mooring stiffness and mooring layout, respectively.

3.2.6 Summary of the Type B Standard Uncertainties of the Measurements

Referring to Table 3.5, calculations of Type B standard uncertainties of measurements can be summarized as follows.

3.2.6.1 Type B standard uncertainty of the incident wave amplitude

The Type B standard uncertainty of the incident wave amplitude, $u_{\xi_0 B}$, is associated with the uncertainties from wave calibrations, u_{WC} , and the Type B standard uncertainty of the wave amplitude at WP2, $u_{\xi_2 B}$, and it is calculated as

$$u_{\xi_0 B}^2 = \bar{\beta} u_{\xi_2 B}^2 + \bar{\xi}_2 u_{WC}^2 \quad (3.42)$$

3.2.6.2 Type B standard uncertainty of wave amplitudes in the gap

The Type B standard uncertainties of the measured wave amplitudes were obtained by considering uncertainties from wave probe calibrations, u_{CWP} , instrument specifications, u_{MB} , and those evaluated numerically, u_{NB} . The final Type B standard uncertainty is given as

$$u_{\xi_j B}^2 = u_{CWP}^2 + u_{MB}^2 + u_{NB}^2 \quad (3.43)$$

The uncertainty from specifications u_{MB} , contributed by the DAQ system and the power supply, was calculated by

$$u_{MB}^2 = u_{DAQ}^2 + u_{ps}^2 \quad (3.44)$$

Uncertainties evaluated from numerical simulations, u_{NB} , were obtained by considering model geometries, $u_{Xgeometry}$, model mass properties, u_{Xmass} , and the moor-

ing system, u_{Xmoor} :

$$u_{NB}^2 = u_{Xgeometry}^2 + u_{Xmass}^2 + u_{Xmoor}^2 \quad (3.45)$$

3.2.6.3 Type B standard uncertainty of drift forces

The Type B standard uncertainties of the drift forces were calculated by considering uncertainties from calibrations of the four load cells, specifications of the DAQ system and the power supply, and those evaluated numerically, i.e.,

$$u_{F'_{ij}B}^2 = \sum (u_{LCC}^2 + u_{MB}^2) + u_{NB}^2 \quad (3.46)$$

where \sum denotes summation of the uncertainties from the four load cells.

3.2.6.4 Type B standard uncertainty of 6-DOF motion amplitudes

Different from wave elevations and drift forces, the 6-DOF motions were captured by the Qualisys system alone. The Type B standard uncertainties of the 6-DOF motion amplitudes were calculated by

$$u_{x'_{ij}B}^2 = u_{QS}^2 + u_{NB}^2 \quad (3.47)$$

3.2.7 Uncertainties in Data Analysis

Uncertainty in data analysis was investigated using different segments of time histories. In each test case, the wave board was operated for 10 minutes. Time series of the measured 6-DOF motions, wave elevations in the gap and drift forces were equally divided into three segments after the transient period, and the data analysis was performed using three separate segments (denoted as Segments 1, 2 and 3)

and the entire segment (denoted as Segment 4). An example of heave motion, wave elevation in the gap and mooring line tension are shown in Figs. 3.21 - 3.23.

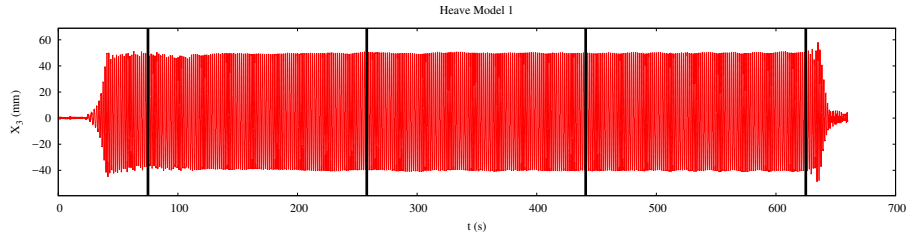


Figure 3.21: Time Series of Heave Motion for Model 1

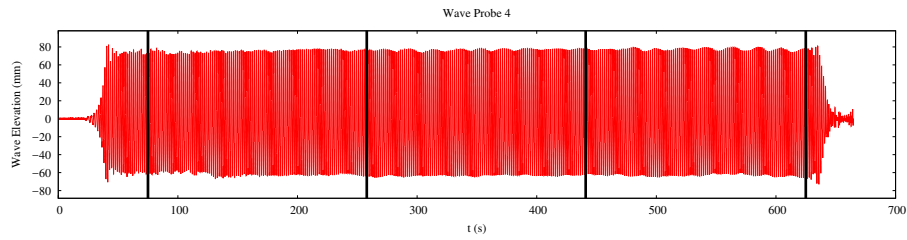


Figure 3.22: Time Series of Wave Elevation at WP4

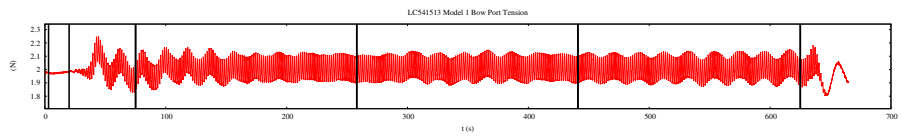


Figure 3.23: Time Series of Mooring Line Tension of Mooring Line M1 for Model 1

The expanded Type A uncertainties were evaluated and compared to investigate the effects of different segments. Figs. 3.24 - 3.26 present uncertainties of heave motion of Model 1, the wave elevation at WP4 and the transverse drift force on Model 1. The results indicate that the uncertainties from Segment 1 are the smallest as expected since the potential wall effect and reflected waves would contribute to uncertainties in measurements for a longer duration. Segment 1 was therefore used

in the following analysis.

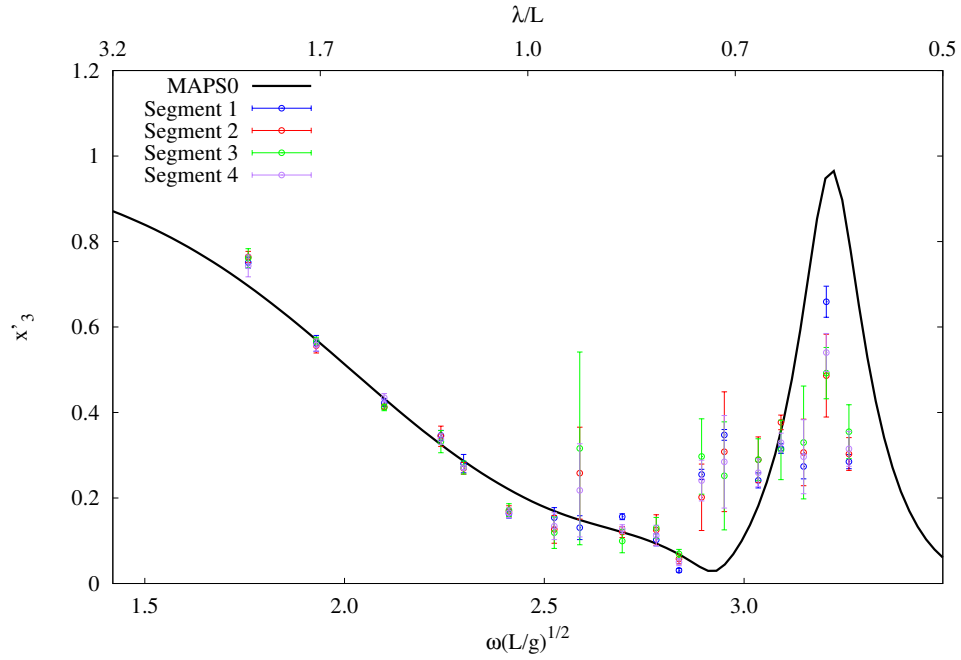


Figure 3.24: Heave of Model 1 Using Different Segments for Data Analysis

3.3 Summary

Details on the model tests of two identical side-by-side FPSOs are presented. Sources of uncertainties in the experiment were identified, and comprehensive uncertainty analysis on the test results was conducted based on the ISO-GUM methodology. The Type A uncertainties were obtained from repeated tests, while the Type B ones were determined from calibration and specification data for instrumentation and by using the numerical method for uncertainties due to model geometry, mass properties, and set-up of the mooring system.

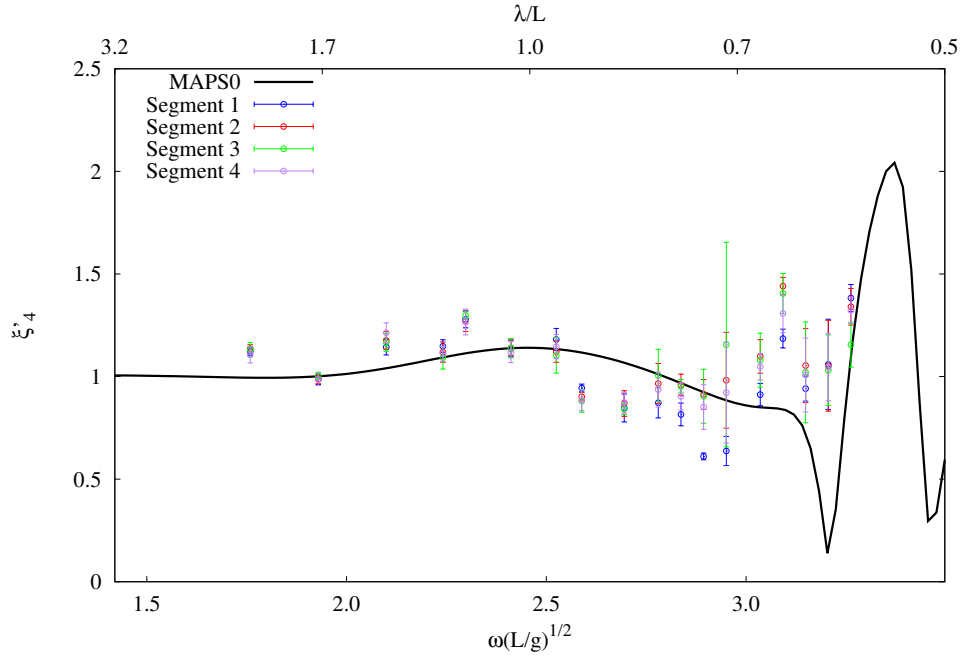


Figure 3.25: Wave Elevation at WP4 Using Different Segments for Data Analysis

It is found from numerical simulations that uncertainties due to the model geometry are negligible. However, uncertainties due to the model mass properties are relatively significant, especially for roll motions. The uncertainty in the gap width leads to large uncertainties in all results since it is closely related to the gap resonance frequency.

As an example, details on the calculation of uncertainties in the heave motion of Model 1, wave elevation at WP4 in the gap, and the longitudinal drift force on Model 1 at the frequency 5.91 rad/s are given in Appendix A. The uncertainty results, along with the numerical predictions, are presented in the next chapter.

Elements of the model tests and the uncertainty analysis presented in this chapter were also published in the work of Qiu et al. (2017) and Qiu et al. (2019).

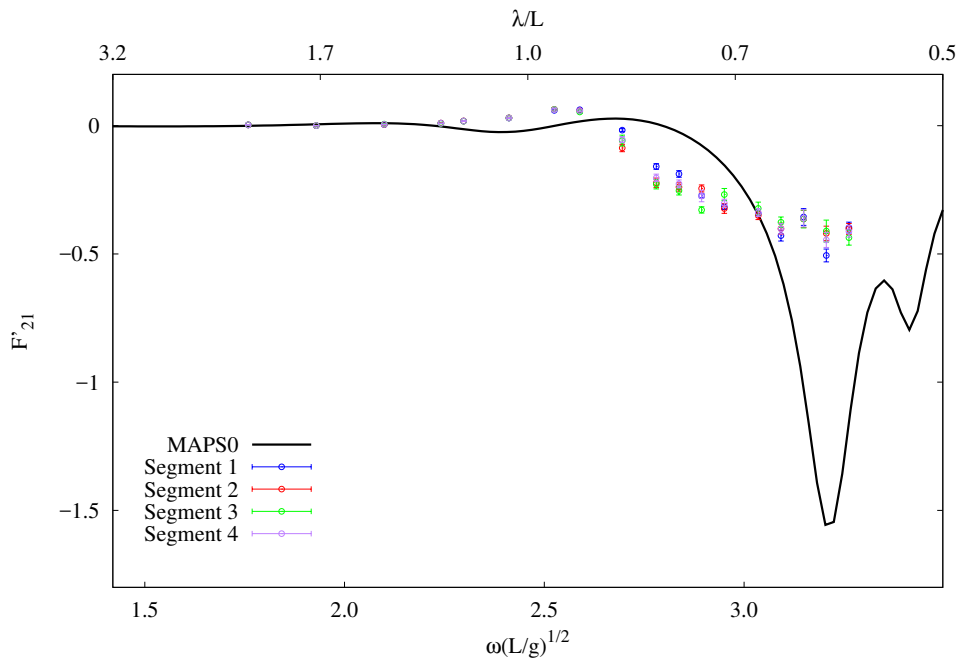


Figure 3.26: Transverse Mean Drift Force on Model 1 Using Different Segments for Data Analysis

Chapter 4

Numerical Simulations on Two-body Interactions in Waves

This chapter presents the numerical simulations on the hydrodynamic interactions of two floating bodies in close proximity. To validate the numerical method presented in Chapter 2, simulations on the experiments described in Chapter 3 are conducted, which involves two identical box-like FPSO models oscillating in head seas without forward speed. Further, validation studies are extended to the underway replenishment of a frigate and a supply vessel at a moderate speed. The two-body interactions are also simulated using a panel-free method based potential-flow program, MAPS0 (Qiu et al., 2006), in the frequency-domain. The numerical results from both methods are compared with each other and with the experimental data. Causes of the discrepancies in potential-flow predictions are identified, and a quasi-steady approach, which considers the changes in the gap due to transverse drift forces for the zero-speed cases, is used to improve the potential-flow simulations.

Prior to the simulations, investigations on wave modelling were conducted for zero-speed and forward-speed cases without the presence of ship models. The requirements for accurate wave generation and effective wave absorption were determined, including the number of cells per wave height, the cell aspect ratio (horizontal dimensions/vertical dimension) in the wave refinement zone, the length of outlet wave damping zone, and the time step size. Detailed results and discussions are presented in Appendix B.

In the present immersed boundary method, the background mesh remains constant, and refinements are made around the floating bodies and near the free surface. As shown in Fig. 4.1, uniform meshes are used in the refinement zones for bodies and a larger cell-aspect ratio was applied in the refinement zone for free surface. Note that the mesh size, h , used in the uncertainty analysis, is defined as the cell size in the body refinement zone, which is equal to the vertical cell size in the free-surface refinement zones.

Cell sizes in the body refinement zones were determined according to the relative error, E_{Δ} , between the targeted displacement of a ship and that calculated based on the level-set method (see Chapter 2). Fig. 4.2 plots the relative error, E_{Δ} , against the number of cells per ship draft. It can be seen that a minimum of 10 cells per draft is required to properly model the ship geometries.

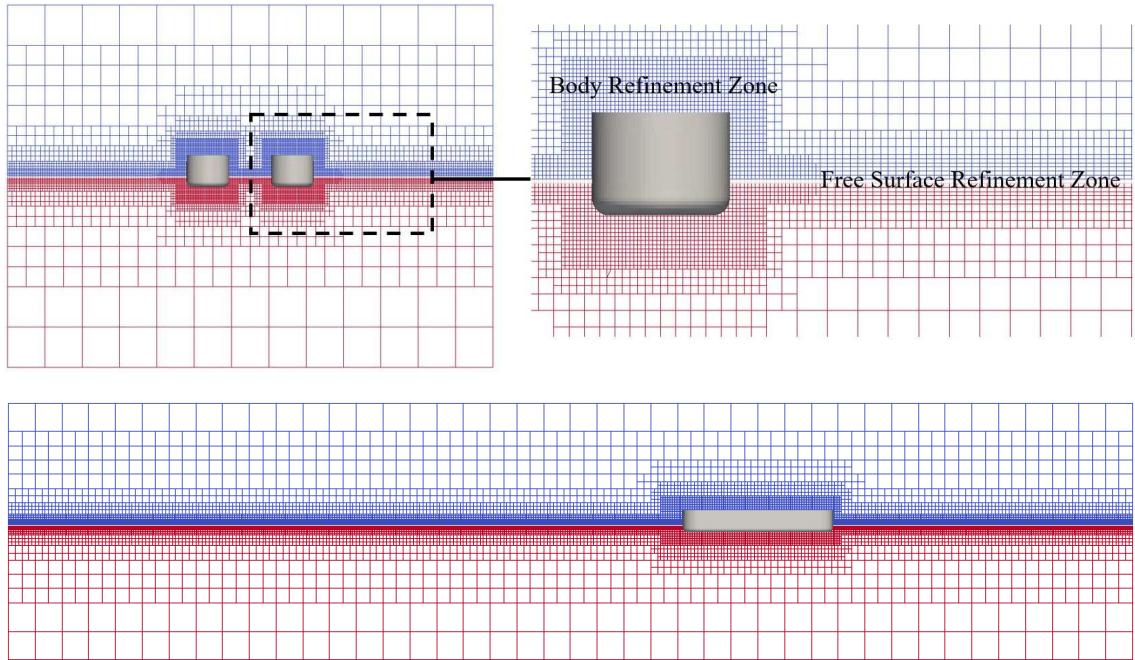


Figure 4.1: Background Mesh (Top: Section View; Bottom: Side View)

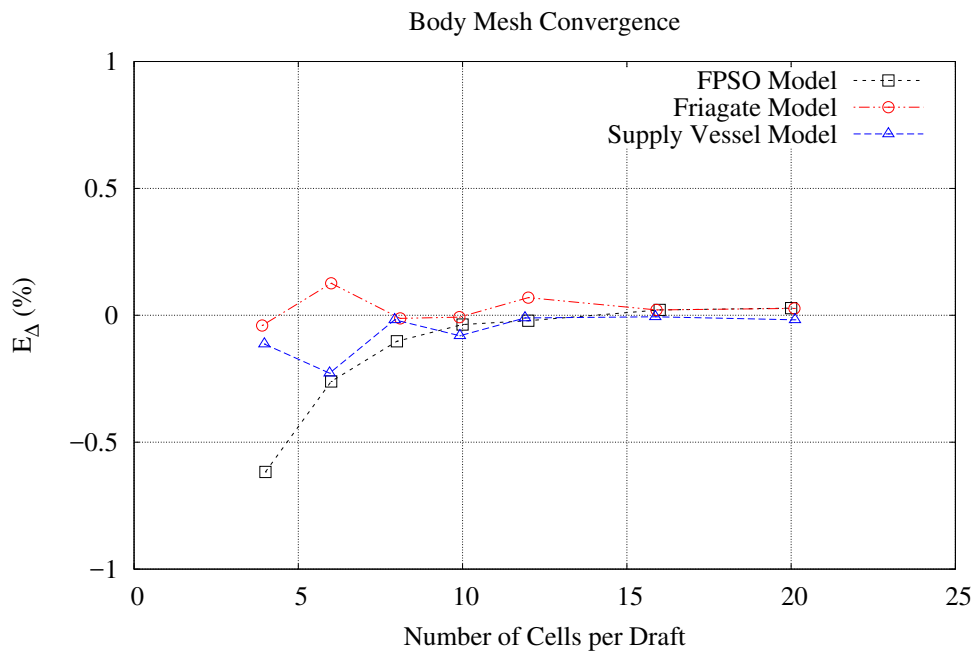


Figure 4.2: Convergence Study on Cell Size in Body Refinement Zone

4.1 Two-body Interactions in Waves at Zero Speed

4.1.1 Set-up for CFD Simulations

For the zero-speed cases, model tests of two identical box-like FPSO models in head seas (see Chapter 3 for details) were simulated. Simulation settings for this case were kept the same as those in the physical model tests. As shown in Fig. 4.3, the width and the depth of the numerical tank were 4.6 m and 1.8 m, respectively, which are the same as those of the towing tank. Each model undergoes 6-DOF motions and is restrained by four soft mooring lines with the same properties as those in the model tests. Based on the convergence studies (see Appendix B), the sizes of the inlet relaxation zone, the computational zone, and the outlet wave damping zone were set as 1.0λ , three model lengths, and 5.0λ , respectively, and the cell aspect ratio is 4 in the free-surface refinement zones.

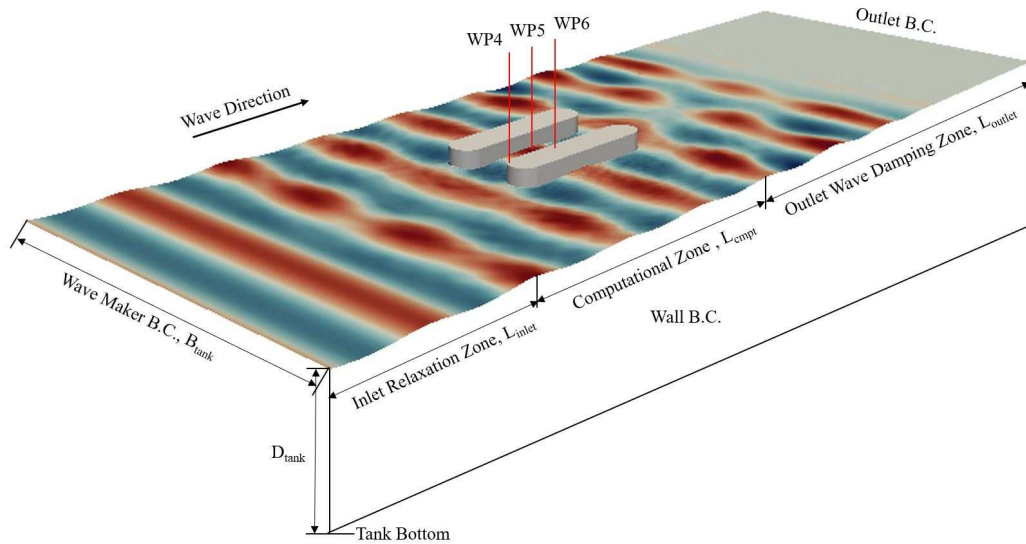


Figure 4.3: Simulation Set-up

4.1.2 Set-up for Potential-flow Simulations

Simulations were also conducted using the frequency-domain Motion Analysis Program Suite (MAPS0) developed by Qiu et al. (2006). The program is based on the panel-free method, where the geometry of a body surface is mathematically represented by Non-Uniform Rational Basis Spline (NURBS) surfaces. The integral equation in terms of source strength is desingularized before it is discretized, allowing the application of Gaussian quadrature globally over the exact body geometry. The near field pressure integration method is used to compute the drift forces (Peng and Qiu, 2014).

Based on the convergence studies, the number of Gaussian points distributed on each ship hull was 984, as shown in Fig. 4.4. No lid was added for irregular frequency removal, and no artificial damping for the free surface in the gap or for the roll motion was included in the computations to investigate the viscous effects in the two-body interaction problem. It is noted that tank walls were not considered.

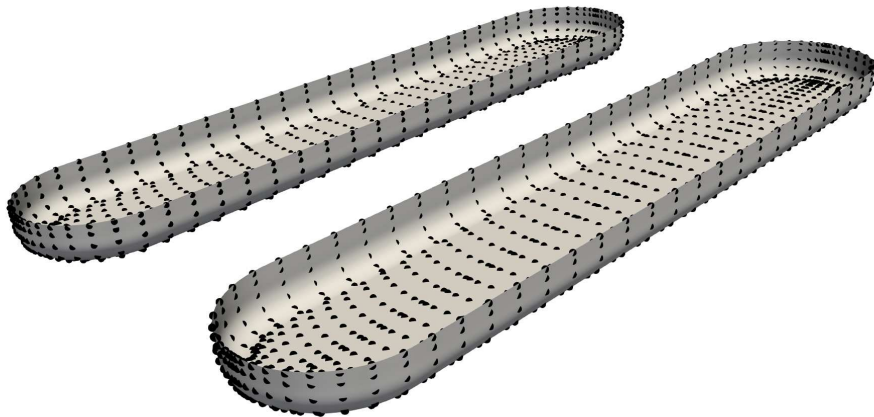


Figure 4.4: Gaussian Point Distribution on Ship Hull Surfaces

4.1.3 Uncertainty Analysis and Convergence Studies

Applying the Grid Convergence Index (GCI) method (Celik et al., 2008), the uncertainties due to spatial discretization were evaluated at four wave frequencies, including a long-wave case, a medium wave case, and two short-wave cases in the resonance region.

The resulting GCI and the intermediate details for $\omega = 4.65$ rad/s ($\lambda/L = 1.43$) are presented in Table 4.1. In these cases, the time step expressed in terms of the Courant-Friedrichs-Lewy number (CFL) was kept as 0.1. Note that $CFL = U_w \Delta t / \Delta z$, where U_w is the wave speed, Δt is the time step and Δz is the vertical cell size in the wave refinement zone. The fine mesh has 14.2 cells per draft and 12.9 cells per wave height, the medium mesh uses 10.7 cells per draft and 9.7 cells per wave height, and the coarse one has 7.1 cells per draft and 6.5 cells per wave height. The total numbers of cells for the fine, medium and coarse meshes are 10.3 M, 4.0 M, and 1.4 M, respectively. In the table, the non-dimensional motions are expressed as $x'_{ij} = x_{ij}/\eta_0$, $i = 1, 2$ and $j = 1, 2, 3$; $x'_{ij} = x_{ij}/(k\eta_0)$, $i = 1, 2$ and $j = 4, 5, 6$, where i represents the i th body, j denotes the mode, η_0 is the amplitude of incident wave, and k is the wavenumber. The amplitudes of wave elevation at WP4, WP5, and WP6, as shown in Fig. 4.3, are non-dimensionalized by $\eta_m = \eta_m/\eta_0$, $m = 4, 5, 6$. The longitudinal and transverse mean drift forces are non-dimensionalized by $F'_{ij} = F_{ij}/(\frac{1}{4}\rho g \xi_0^2 L_i)$, $j = 1, 2$ for longitudinal and transverse directions, respectively. The convergence types (CT) are denoted as M (monotonic), O (oscillatory), and D (divergent). It can be seen that uncertainties due to spatial discretization are small for body motions and wave elevations in the gap. However, greater uncertainty is observed in the longitudinal drift force. The

reason is that the mean drift forces are in small amplitude, and a small deviation in absolute value could lead to a large change in relative value and hence a greater uncertainty. It is also indicated that a finer grid may be needed to compute the drift forces for long waves, i.e., more grids over a wave height.

Table 4.1: Uncertainties in motions of Body 1, wave elevations in the gap, and mean drift forces on Body 1 from OpenFOAM at $\omega = 4.65$ rad/s

Parameter	x'_{11}	x'_{13}	x'_{14}	x'_{15}	η'_4	η'_5	η'_6	F'_{11}
h_1 (m)	0.0070							
h_2 (m)	0.0094							
h_3 (m)	0.0141							
ϕ_1	0.3387	0.4206	0.0258	0.6529	1.0788	0.8594	1.0253	-0.0267
ϕ_2	0.3372	0.4169	0.0218	0.6500	1.0697	0.8503	1.0105	-0.0317
ϕ_3	0.3389	0.3741	0.0796	0.6688	1.0827	0.7791	1.0294	-0.0248
CT	O	M	O	O	O	M	O	O
p	0.3774	5.7380	6.7723	4.8702	1.0031	4.7380	0.6878	0.9211
ϕ_{ext}^{21}	0.3524	0.4215	0.0265	0.6538	1.1057	0.8625	1.0930	-0.0104
$e_a^{21}(\%)$	0.4657	0.8965	18.2548	0.4380	0.8437	1.0684	1.4663	15.6209
$e_{\text{ext}}^{21}(\%)$	3.8842	0.2105	2.5009	0.1423	2.4395	0.3621	6.1949	156.4729
$\text{GCI}_{\text{fine}}^{21}(\%)$	5.0750	0.2661	3.7916	0.1789	3.1520	0.4591	8.3760	64.3491

For this wavelength, convergence studies on the time step were carried out using $CFL = 0.1, 0.14$ and 0.2 and the mesh size, h_2 . As shown in Fig. 4.5, the predicted surge, heave and pitch motions of Body 1 and wave elevations at WP4, WP5 and

WP6 are generally insensitive to time step.

For the medium wave case with $\omega = 5.72$ rad/s ($\lambda/L = 0.94$), the GCI and the intermediate results are presented in Table 4.2. The time step in terms of CFL was kept as 0.1. The total numbers of cells for the fine mesh with 23.1 cells per draft and 13.9 cells per wave height, the medium mesh with 17.8 cells per draft and 10.7 cells per wave height, and the coarse mesh with 14.2 cells per draft and 8.5 cells per wave height are 14.7 M, 7.1 M, and 4.2 M, respectively. In general, the spatial convergence is achieved, except the wave elevations at WP5. The reason could be that the wave elevations in the gap are not sensitive to the change in mesh size. As the difference between the results obtained using different meshes is too small, the uncertainty analysis procedure may not be valid (Celik et al., 2008).

Similarly, mesh with cell size h_2 and $CFL = 0.1, 0.14$ and 0.2 were used for the convergence studies on the time step. Figure 4.6 presents the temporal convergence of heave and pitch motions of Body 1, longitudinal drift force on Body 1, and wave elevations at WP4, WP5, and WP6. It can be seen that the results are converged as the time step is decreased.

Table 4.3 presents the GCI and the intermediate results for a short wave with $\omega = 6.91$ rad/s ($\lambda/L = 0.65$). While keeping the time step, $CFL = 0.1$, the total numbers of cells for the fine mesh with 30.2 cells per draft and 12.4 cells per wave height, the medium mesh with 24.9 cells per draft and 10.2 cells per wave height, and the coarse mesh with 17.8 cells per draft and 7.3 cells per wave height are 18.5 M, 10.7 M, and 4.5 M, respectively. It can be seen that the spatial convergence is achieved, but the results are more sensitive to the mesh size compared to the longer wave cases.

Convergence studies on the time step for this shorter wave were conducted using

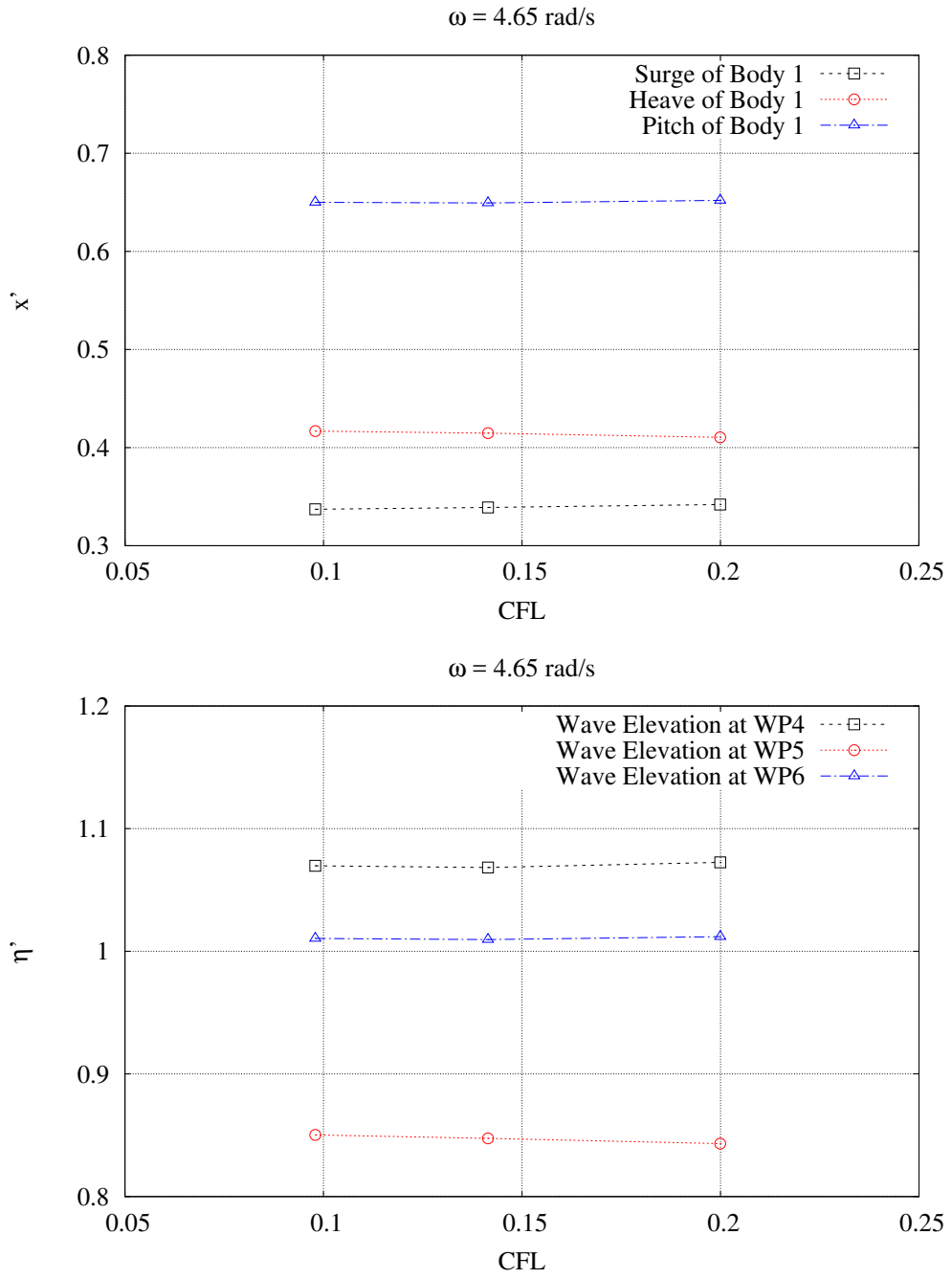


Figure 4.5: Temporal Convergence for Motions of Body 1 and Wave Elevations in the Gap from OpenFOAM at $\omega = 4.65 \text{ rad/s}$

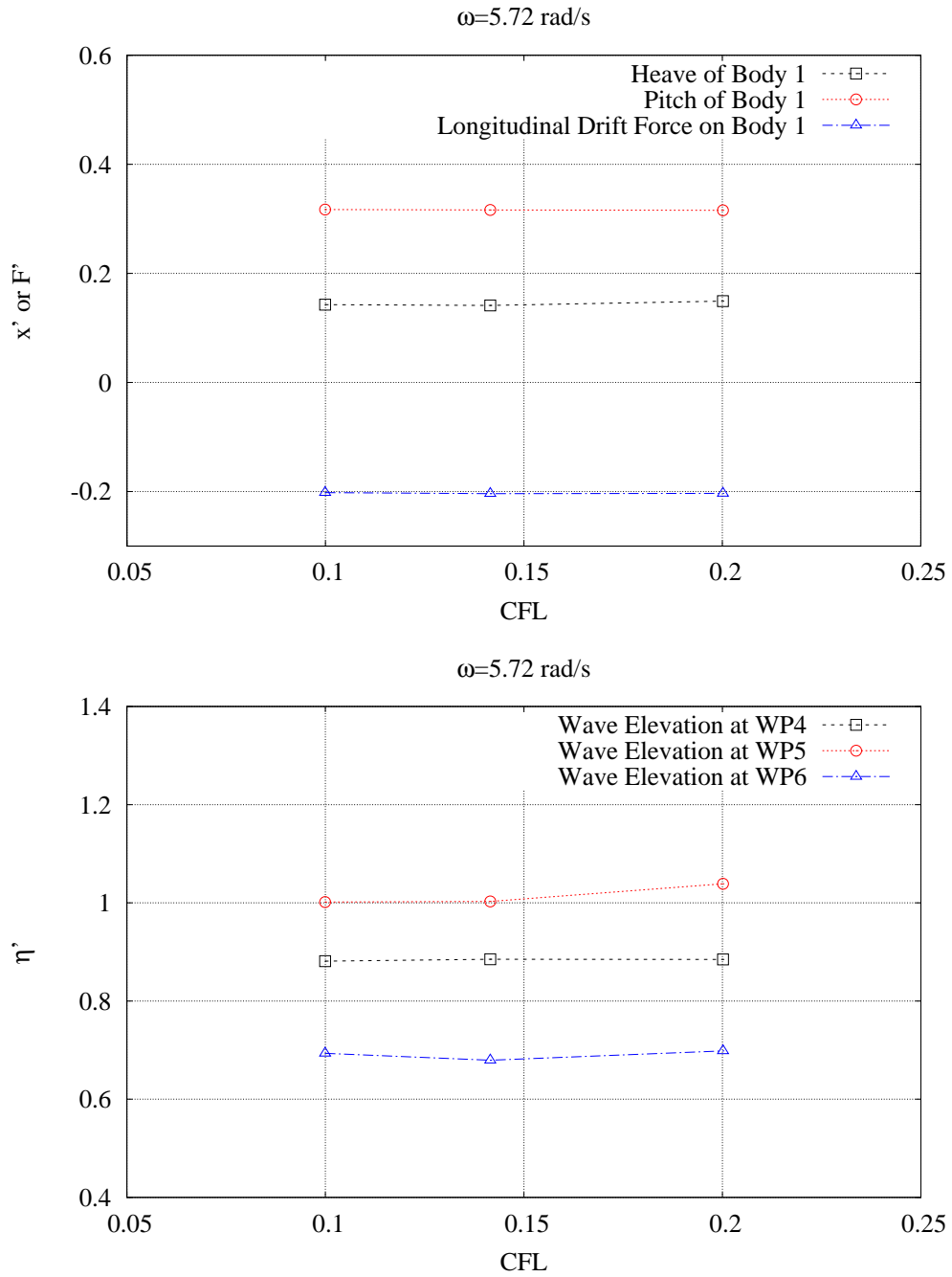


Figure 4.6: Temporal Convergence for Motions of Body 1, Mean Drift Forces on Body 1 and Wave Elevations in the Gap from OpenFOAM at $\omega = 5.72$ rad/s

Table 4.2: Uncertainties in motions of Body 1, wave elevations in the gap, and mean drift forces on Body 1 from OpenFOAM at $\omega = 5.72$ rad/s

Parameter	x'_{11}	x'_{13}	x'_{14}	x'_{15}	ξ'_4	ξ'_5	ξ'_6	F'_{11}
$h_1(m)$	0.0043							
$h_2(m)$	0.0056							
$h_3(m)$	0.0070							
ϕ_1	0.0397	0.1402	0.0818	0.3174	0.9038	0.9833	0.7099	-0.1982
ϕ_2	0.0393	0.1426	0.0851	0.3170	0.8912	1.0016	0.6934	-0.2021
ϕ_3	0.0410	0.1811	0.0915	0.3157	0.8782	1.0137	0.6699	-0.2157
CT	O	M	M	M	M	D	M	M
p	6.5150	12.4958	3.3116	5.8280	0.7747	-	2.1497	5.8667
ϕ_{ext}^{21}	0.0398	0.1401	0.0793	0.3175	0.9598	-	0.7316	-0.1971
$e_a^{21}(\%)$	0.9929	1.7022	3.9472	0.1218	1.4175	-	2.3733	1.9538
$e_{\text{ext}}^{21}(\%)$	0.2168	0.0679	3.0600	0.0336	5.8395	-	2.9689	0.5474
$\text{GCI}_{\text{fine}}^{21}(\%)$	0.2743	0.0833	3.5649	0.0421	7.8619	-	3.9155	0.6672

the mesh with cell size h_2 and $CFL = 0.1, 0.14,$ and 0.2 . Figure 4.7 presents the temporal convergence of surge and roll motions of Body 1, transverse drift force on Body 1, and wave elevations at WP4, WP5, and WP6. It can be observed that the responses are slightly more sensitive than those for the longer waves presented above, but they converged as CFL was decreased.

Table 4.4 presents the GCI and the intermediate results for a short wave with $\omega = 7.04$ rad/s ($\lambda/L = 0.62$). The time step in terms of CFL was kept as 0.1 The total numbers of cells for the fine mesh, medium mesh and coarse mesh are 18.5 M, 10.7

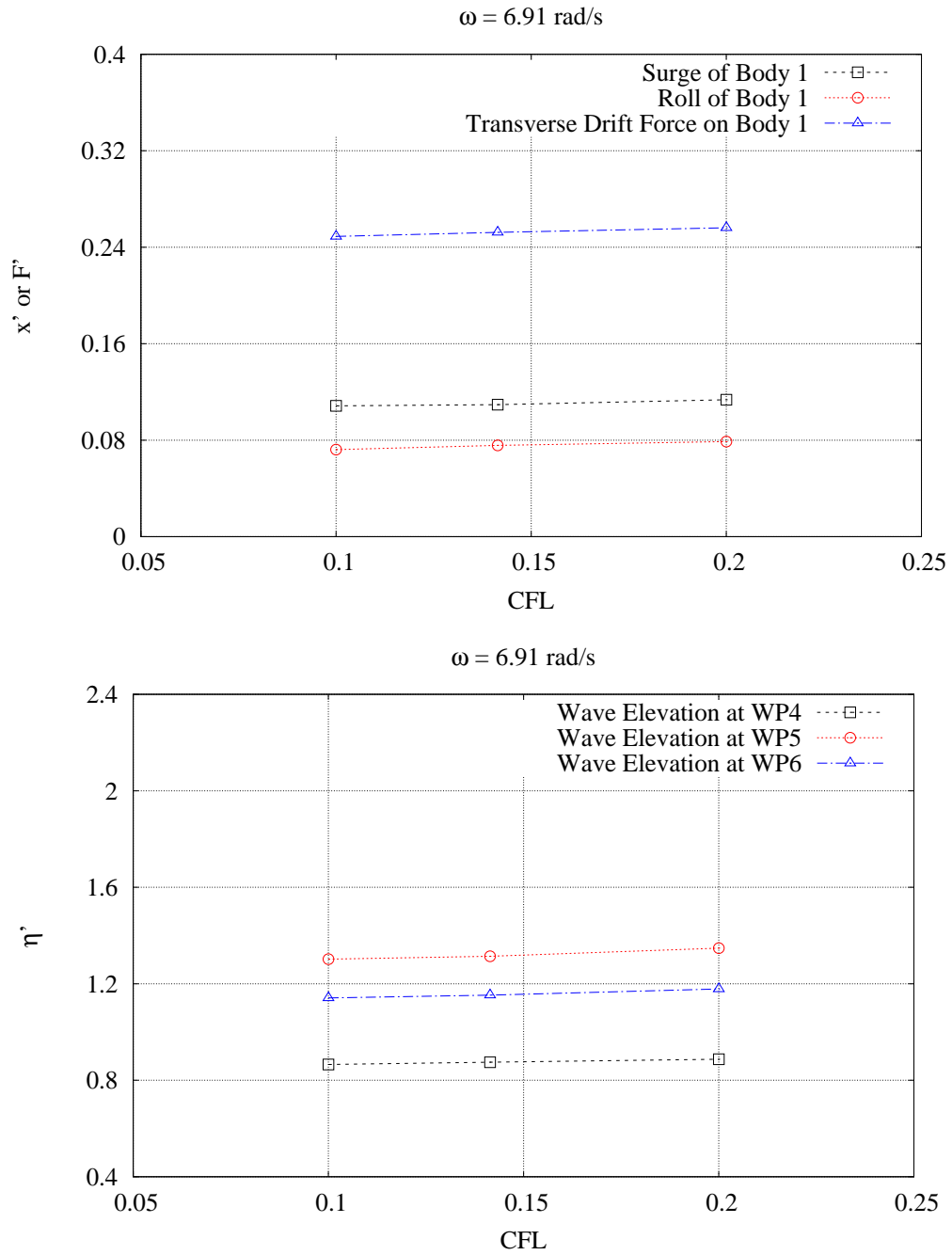


Figure 4.7: Temporal Convergence for Motions of Body 1, Mean Drift Forces on Body 1 and Wave Elevations in the Gap from OpenFOAM at $\omega = 6.91 \text{ rad/s}$

Table 4.3: Uncertainties in motions of Body 1, wave elevations in the gap, and mean drift forces on Body 1 from OpenFOAM at $\omega = 6.91$ rad/s

Parameter	x'_{12}	x'_{13}	x'_{14}	x'_{15}	ξ'_5	ξ'_6	F'_{11}	F'_{12}
$h_1(m)$	0.0033							
$h_2(m)$	0.0040							
$h_3(m)$	0.0056							
ϕ_1	0.0776	0.2222	0.0730	0.0391	1.4192	1.0998	-0.2087	-0.2647
ϕ_2	0.0821	0.2308	0.0722	0.0365	1.3020	1.1012	-0.2162	-0.2490
ϕ_3	0.0760	0.2423	0.0469	0.0429	1.1466	1.1181	-0.2024	-0.2765
CT	O	M	M	O	M	M	O	O
p	1.1286	2.2720	9.8966	3.0431	2.3085	6.7928	2.1527	1.9836
ϕ_{ext}^{21}	0.0594	0.2068	0.0731	0.0424	1.6265	1.0993	-0.1943	-0.2981
$e_a^{21}(\%)$	5.4258	3.7208	1.1125	7.1208	9.0002	0.1272	3.4683	6.2982
$e_{\text{ext}}^{21}(\%)$	30.5836	7.4934	0.1884	7.6242	12.7419	0.0465	7.4408	11.2002
$\text{GCI}_{\text{fine}}^{21}(\%)$	27.6875	8.3896	0.2385	11.0515	19.8959	0.0581	8.3566	16.7590

M, and 4.5 M, respectively, and the corresponding cell sizes are 30.2 cells per draft and 12.1 cells per wave height, 24.9 cells per draft and 10.0 cells per wave height and 17.8 cells per draft and 7.1 cells per wave height, respectively. Similar to the previous short-wave case with $\omega = 6.91$ rad/s, spatial convergence was achieved, but larger uncertainties were observed compared to the long-wave cases.

Similar to the previous case, mesh with cell size h_2 and $CFL = 0.1, 0.14,$ and 0.2 were used for the convergence studies on the time step for this shorter wave. Figure 4.8 presents the temporal convergence of surge and roll motions of Body 1, transverse

Table 4.4: Uncertainties in motions of Body 1, wave elevations in the gap, and mean drift forces on Body 1 from OpenFOAM at $\omega = 7.04$ rad/s

Parameter	x'_{12}	x'_{13}	x'_{14}	x'_{15}	ξ'_5	ξ'_6	F'_{11}	F'_{12}
$h_1(m)$	0.0033							
$h_2(m)$	0.0040							
$h_3(m)$	0.0056							
ϕ_1	0.1045	0.4211	0.0527	0.0974	0.8641	1.8485	-0.1589	-0.2589
ϕ_2	0.1004	0.4049	0.0517	0.0991	0.8667	1.8002	-0.1648	-0.2420
ϕ_3	0.0953	0.3430	0.0445	0.0952	0.8858	1.6916	-0.1562	-0.1840
CT	M	M	M	O	M	M	O	M
p	2.6670	2.8713	5.1653	2.8808	5.1469	0.9691	1.3530	2.4927
ϕ_{ext}^{21}	0.1104	0.4429	0.0532	0.0951	0.8626	2.0819	-0.1394	-0.2861
$e_a^{21}(\%)$	4.0134	4.0154	1.8937	1.7093	0.2992	2.6838	3.5551	6.9986
$e_{\text{ext}}^{21}(\%)$	5.3827	4.9191	1.0654	2.3757	0.1752	11.2110	13.9873	9.5092
$\text{GCI}_{\text{fine}}^{21}(\%)$	7.3965	6.7267	1.3716	2.8511	0.2179	16.2068	14.7934	14.0548

drift force on Body 1, and wave elevations at WP4, WP5, and WP6. The results were converged as CFL was decreased.

4.1.4 Validation Studies

Based on the spatial uncertainty analysis and temporal convergence studies, the following settings were used for simulations of two bodies in waves at zero speed: at least ten cells over the model draft in the body refinement zone, at least eight cells per wave height, the cell aspect ratio of four in the wave refinement zone, more than

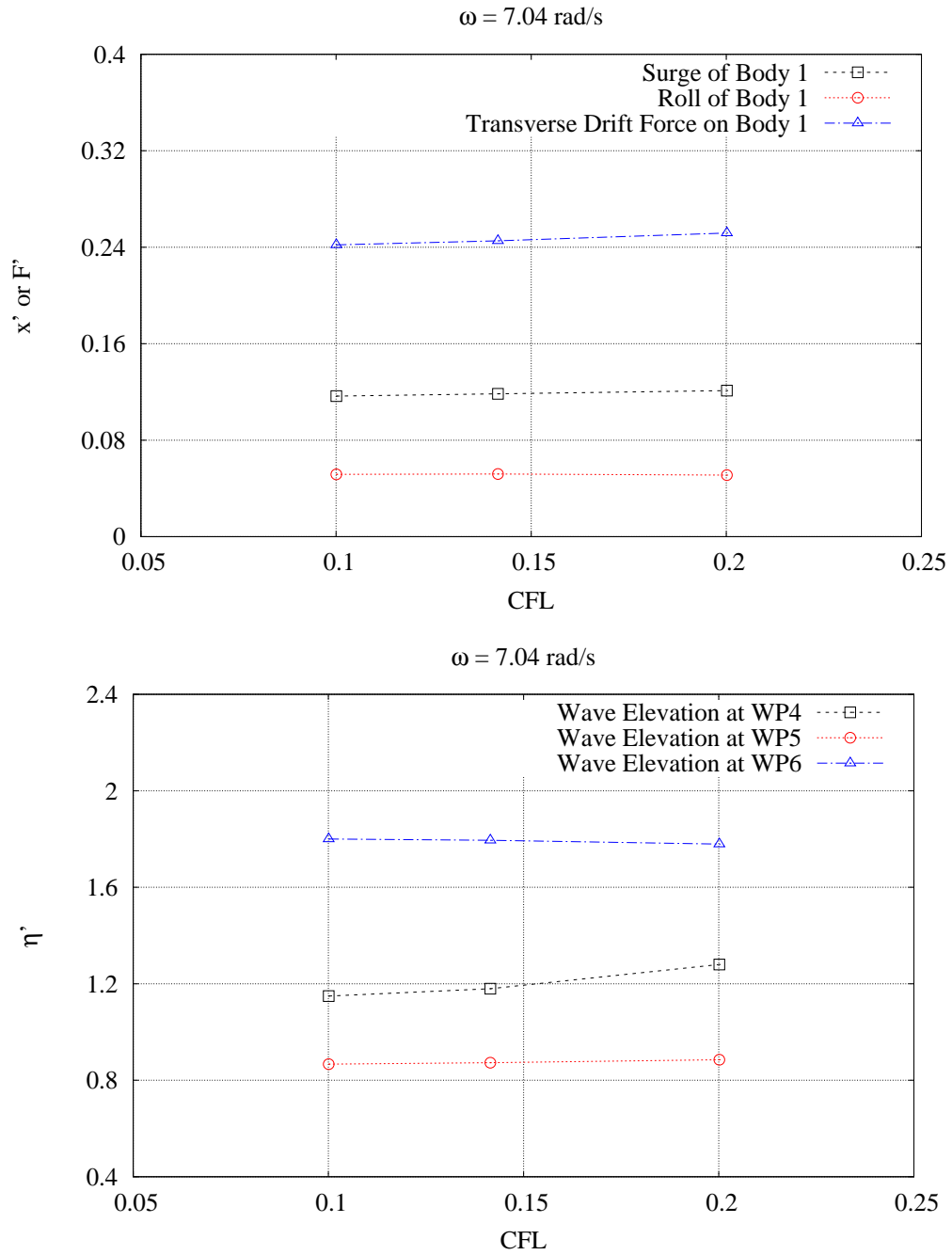


Figure 4.8: Temporal Convergence for Motions of Body 1, Mean Drift Forces on Body 1 and Wave Elevations in the Gap from OpenFOAM at $\omega = 7.04 \text{ rad/s}$

five wavelengths for the outlet wave damping zone, and CFL less than 0.14.

Time series of the sway motion of Bodies 1 and 2, heave and roll of Body 1 and wave elevation at WP6 for $\omega = 3.90$ rad/s ($\lambda/L = 2.03$) are presented in Fig. 4.9. For the long-wave case, a very good agreement can be observed between the numerical and experimental results. From the time series of sway motions, it can be seen that the change of gap is relatively small.

Figure 4.10 presents the time series of sway of Bodies 1 and 2, heave and roll of Body 1, and wave elevations at WP6 for $\omega = 5.72$ rad/s ($\lambda/L = 0.94$). For this medium wave case, the numerical results agree very well with the experimental data. As can be seen from the results, the wave elevations in the gap are more nonlinear compared to the long-wave case.

Time series of the sway of Bodies 1 and 2, heave and roll of Body 1, and wave elevations at WP6 for $\omega = 6.91$ rad/s ($\lambda/L = 0.65$) are presented in Fig. 4.11. Note that this frequency is in the resonance region. Compared to the long-wave cases, more nonlinearities can be observed in the responses. The predictions are generally in good agreement with the experimental ones. As shown in Fig. 4.12, sway motions of the two bodies clearly show a larger change of gap than that for a longer wave outside the resonance region.

Numerical results, including 6-DOF motions of Body 1, wave elevations in the gap, and drift forces on Body 1, obtained by the present method at all the tested wave frequencies, were compared with experimental data and those using the potential-flow method. Non-dimensional motions of Body 1 and wave elevations in the gap at WP4, WP5, and WP6 are presented in Figs. 4.13 to 4.21. Figures 4.22 and 4.23 present non-dimensionalized longitudinal and transverse drift forces acting on Body 1. In

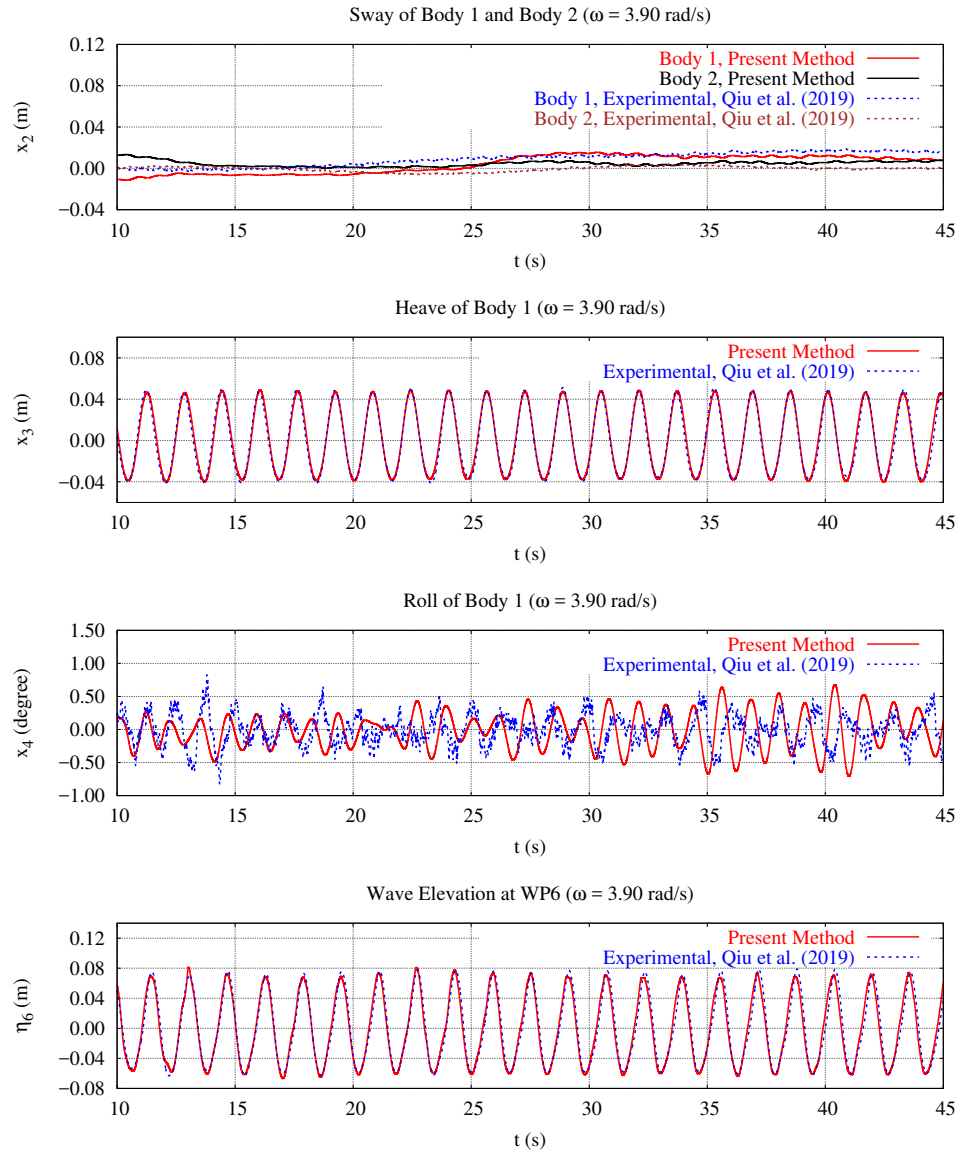


Figure 4.9: Time Series of Sway of Bodies 1 and 2, Heave and Roll of Body 1 and Wave Elevation at WP6 at $\omega = 3.90$ rad/s

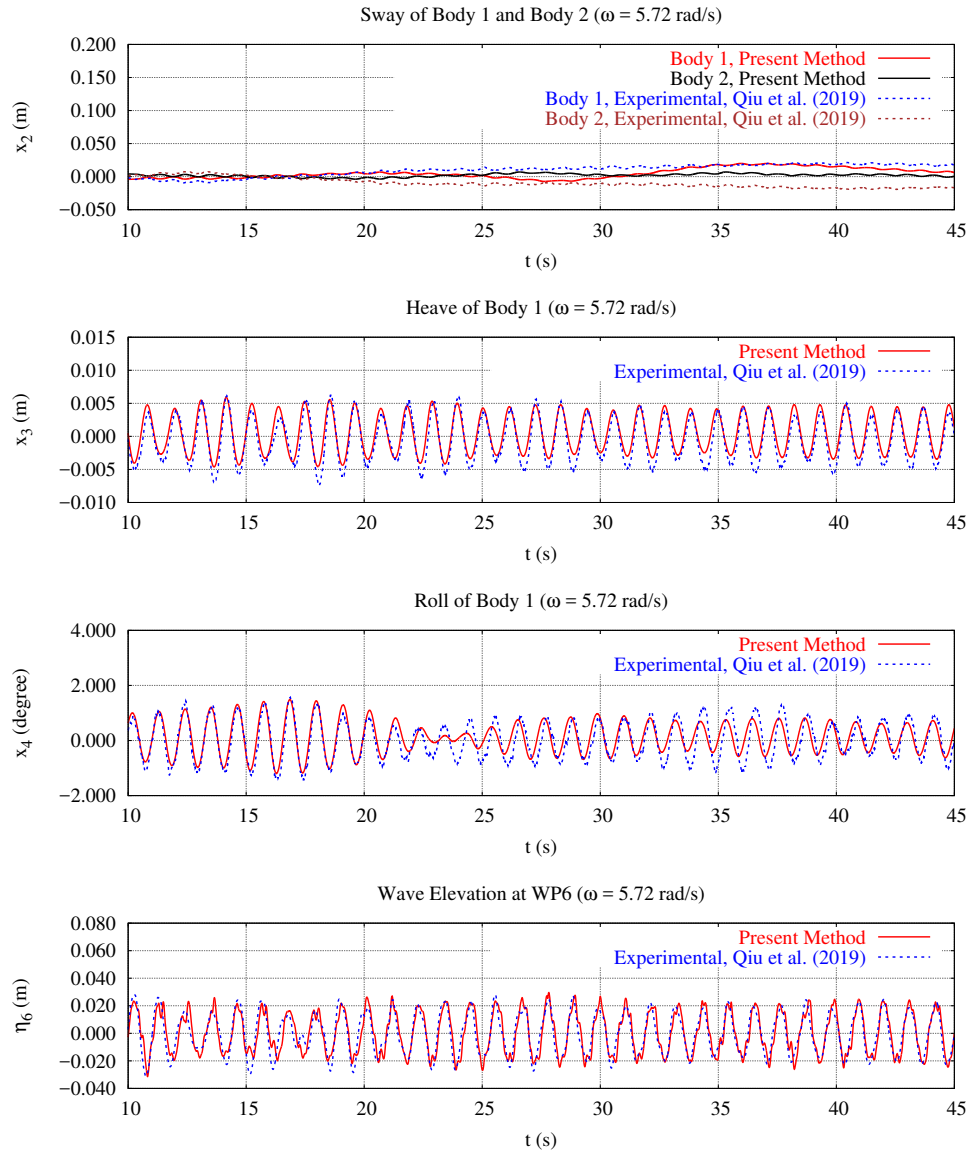


Figure 4.10: Time Series of Sway of Bodies 1 and 2, Heave and Roll of Body 1 and Wave Elevation at WP6 at $\omega=5.72$ rad/s

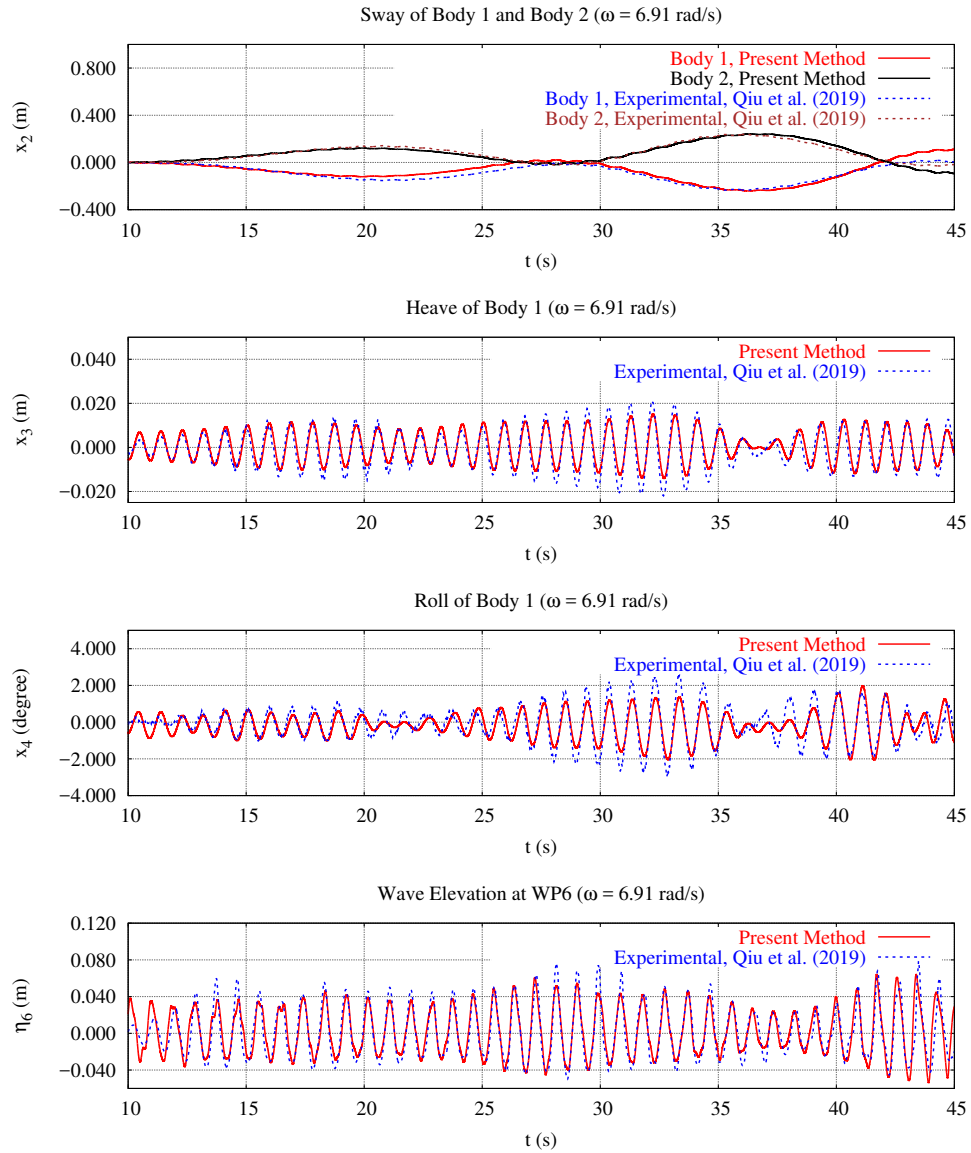


Figure 4.11: Time Series of Sway of Bodies 1 and 2, Heave and Roll of Body 1 and Wave Elevation at WP6 at $\omega=6.91$ rad/s

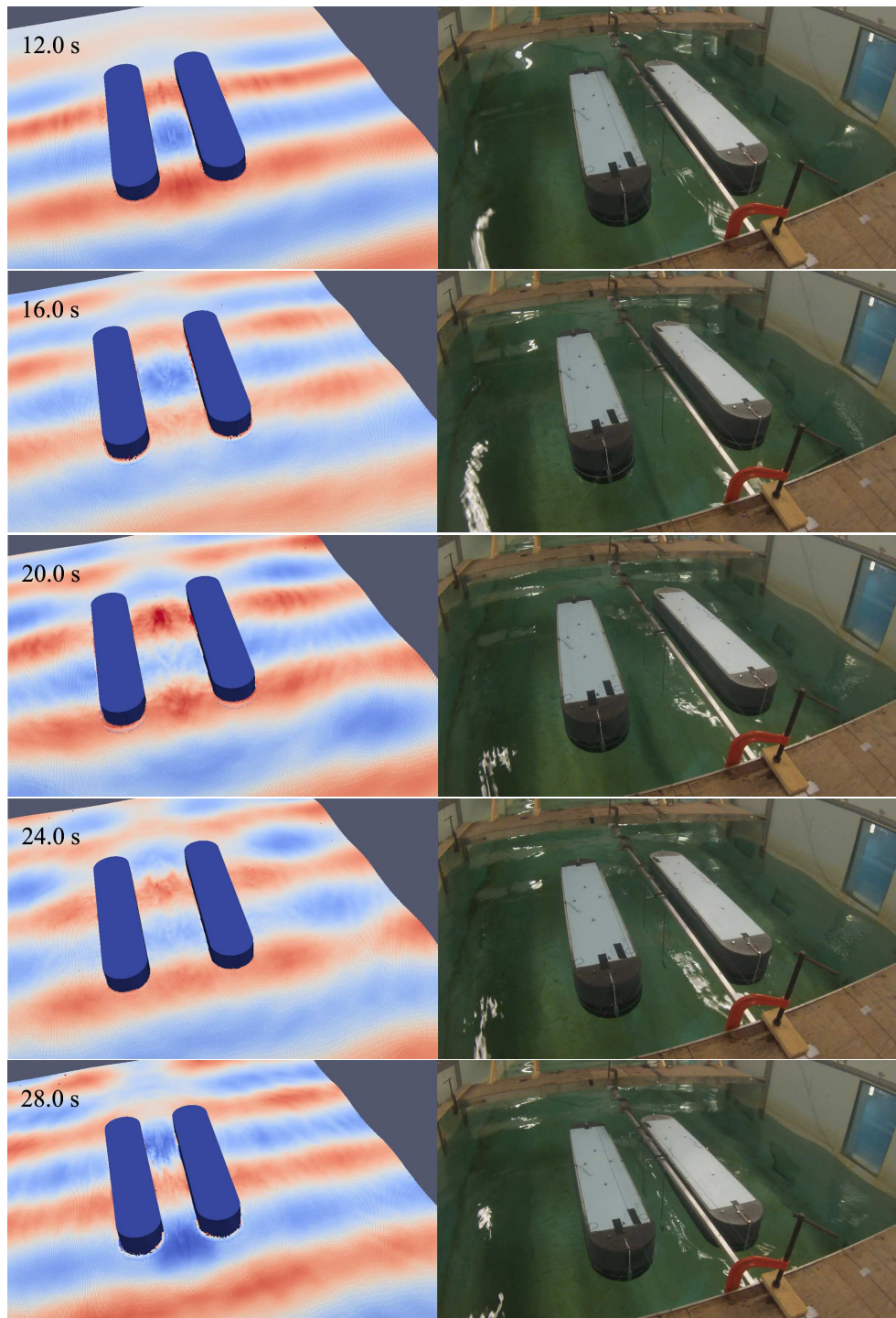


Figure 4.12: Comparison between Numerical Simulation and Model Test at $\omega=6.91$ rad/s

these figures, Type A and Type B uncertainties in the experimental results obtained using the method introduced in Chapter 3 are also presented.

Since the present method considers large body motions and viscosity, it leads to a much better agreement with experimental data than those using MAPS0, especially in the resonance region. The large discrepancies between the potential-flow results and the model test data could be attributed to the ignorance of viscous effects and also the constant gap width used in the simulations. As observed in both experimental data and CFD simulation results, the gap width remains constant in long waves (see Fig. 4.9). However, the gap between the two ships varies due to the transverse drift forces for short-wave cases in the resonance region (see Figs. 4.11 and 4.12).

To further investigate the gap effect, a quasi-steady approach was used in MAPS0. The mean gap width, D_{gap} , at each wave frequency was first determined using the mean transverse positions of Body 1, \bar{Y}_1 , and Body 2, \bar{Y}_2 and the initial gap width from test set-up, D_{gap0} , which is 40 cm in model scale.

$$D_{gap} = D_{gap0} - \bar{Y}_1 + \bar{Y}_2 \quad (4.1)$$

where the mean transverse positions were evaluated by averaging the time series of sway motions after the transit period.

Figure 4.24 shows the mean gap width from the model tests (average value of the five repeated tests, see Chapter 3) and the CFD simulations. It can be seen that the mean gap width in the resonance region is nearly 1.5 times that from the initial set-up, and the numerical results are generally in agreement with the test data. The mean gap widths were then used as input for the MAPS0 simulations.

Figures 4.25 - 4.32 present the surge, heave, roll and pitch motions of Body 1,

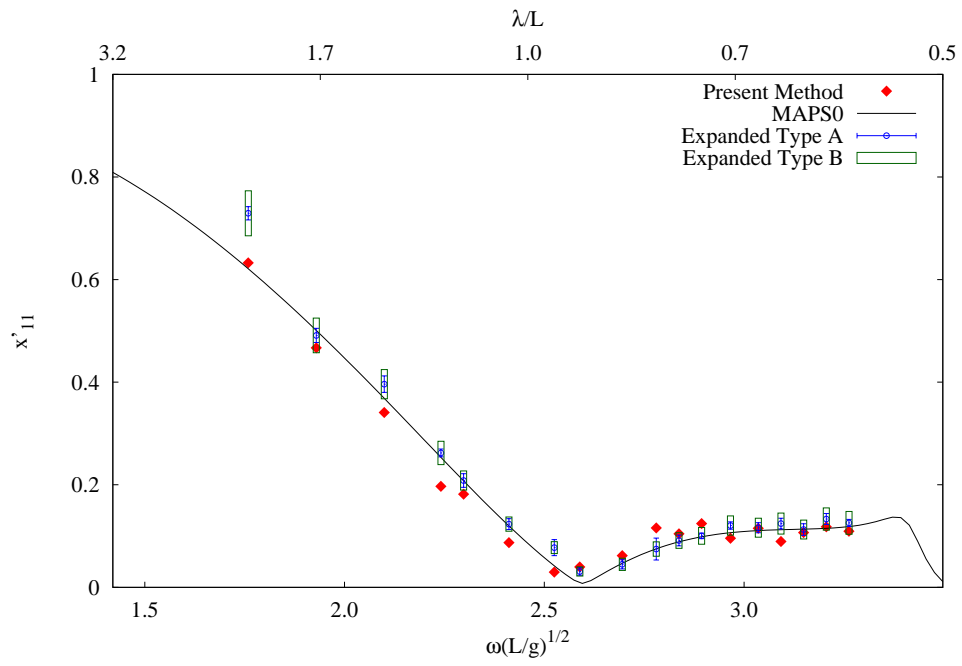


Figure 4.13: Surge Motion of Body 1

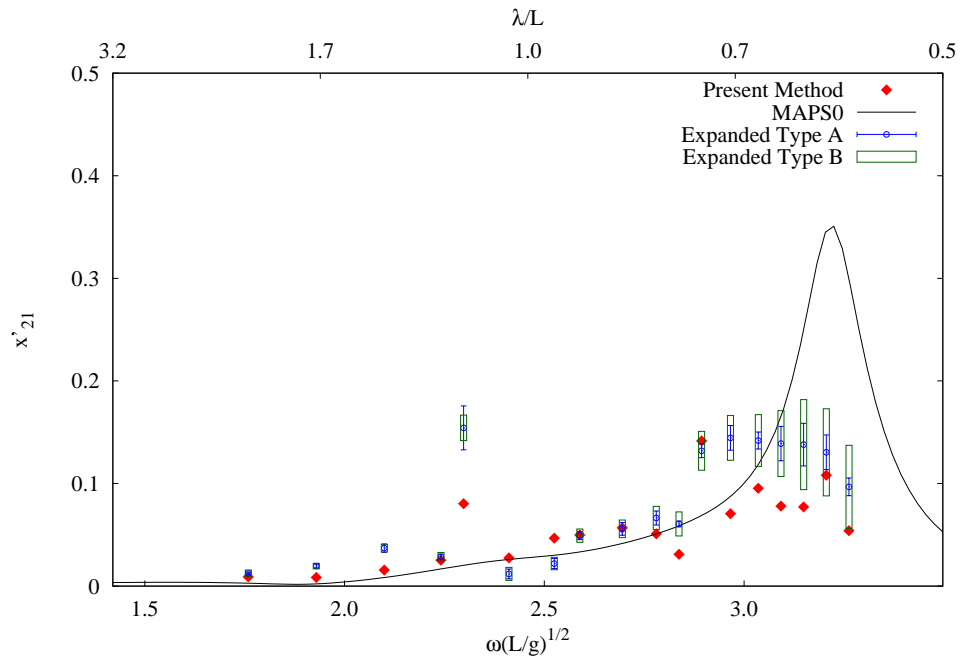


Figure 4.14: Sway Motion of Body 1

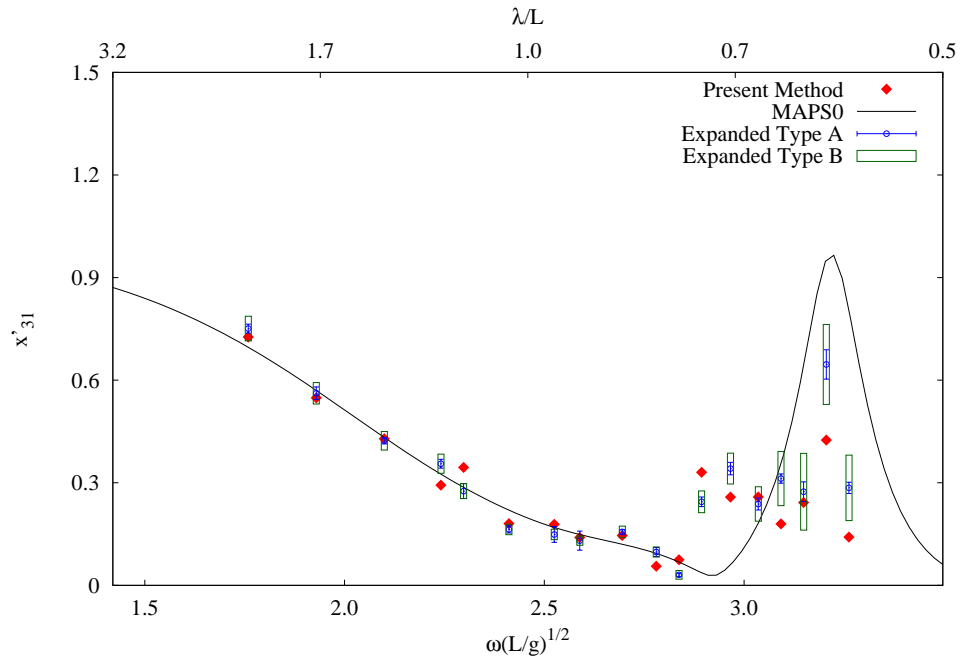


Figure 4.15: Heave Motion of Body 1

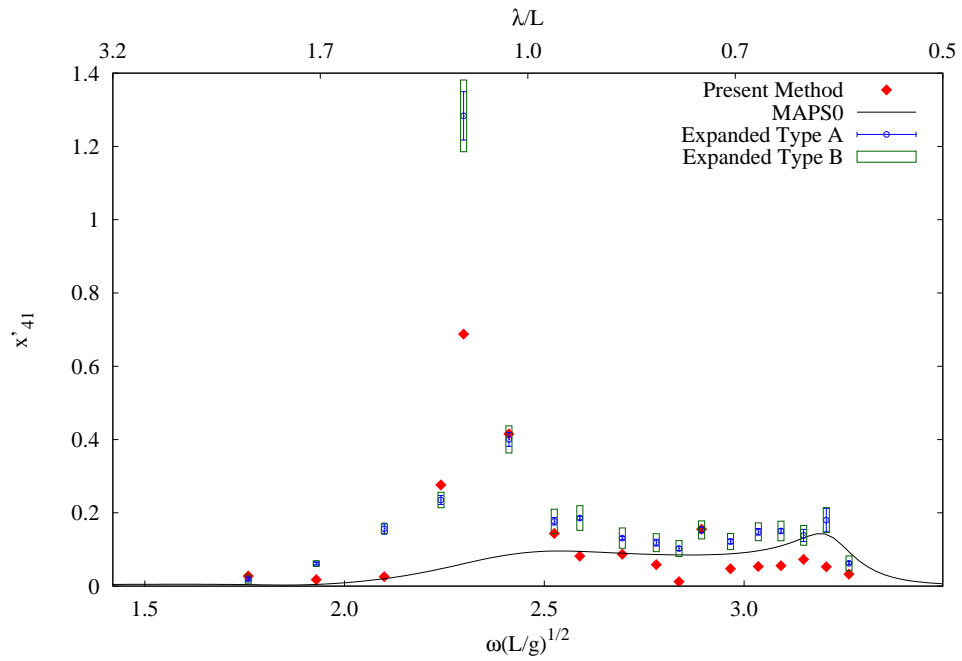


Figure 4.16: Roll Motion of Body 1

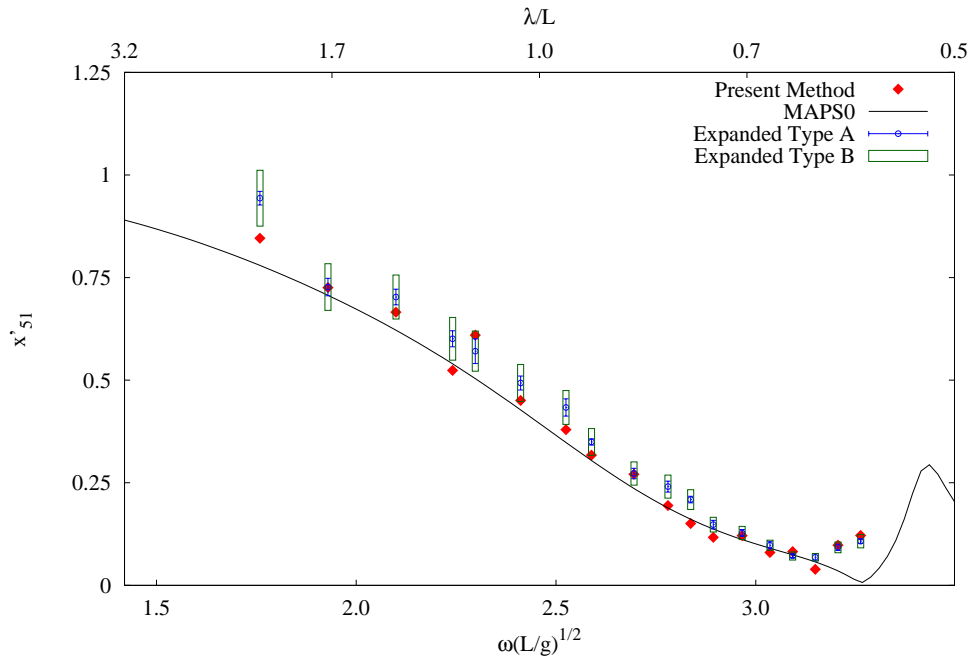


Figure 4.17: Pitch Motion of Body 1

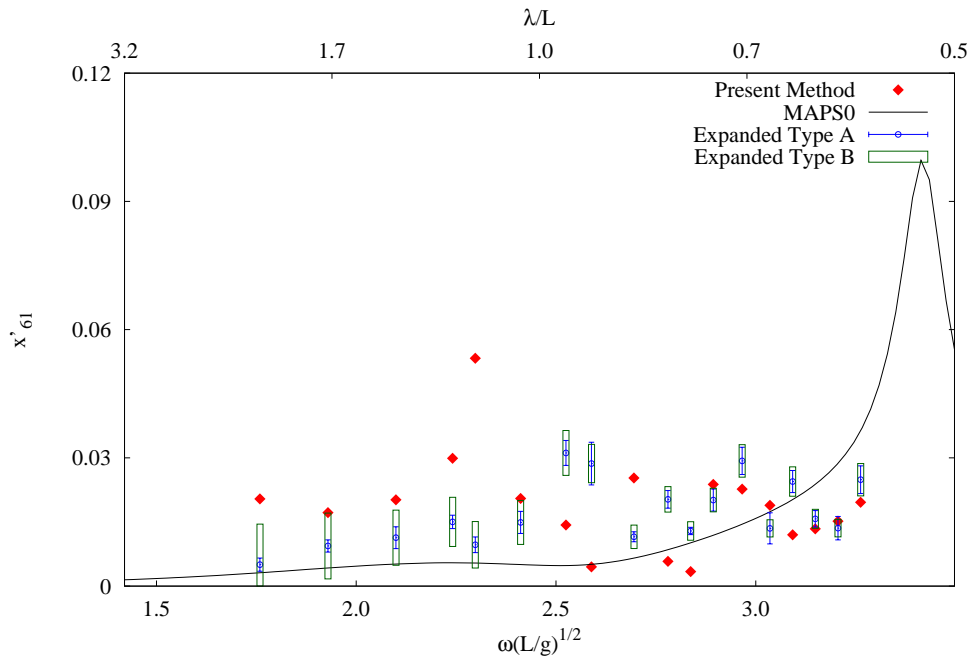


Figure 4.18: Yaw Motion of Body 1

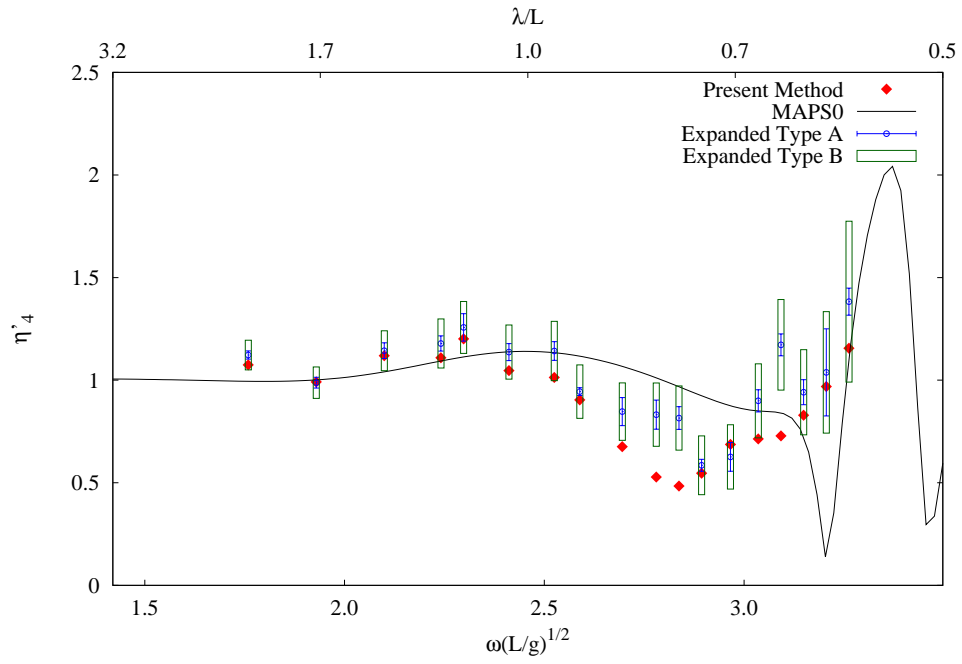


Figure 4.19: Wave Elevation at WP4

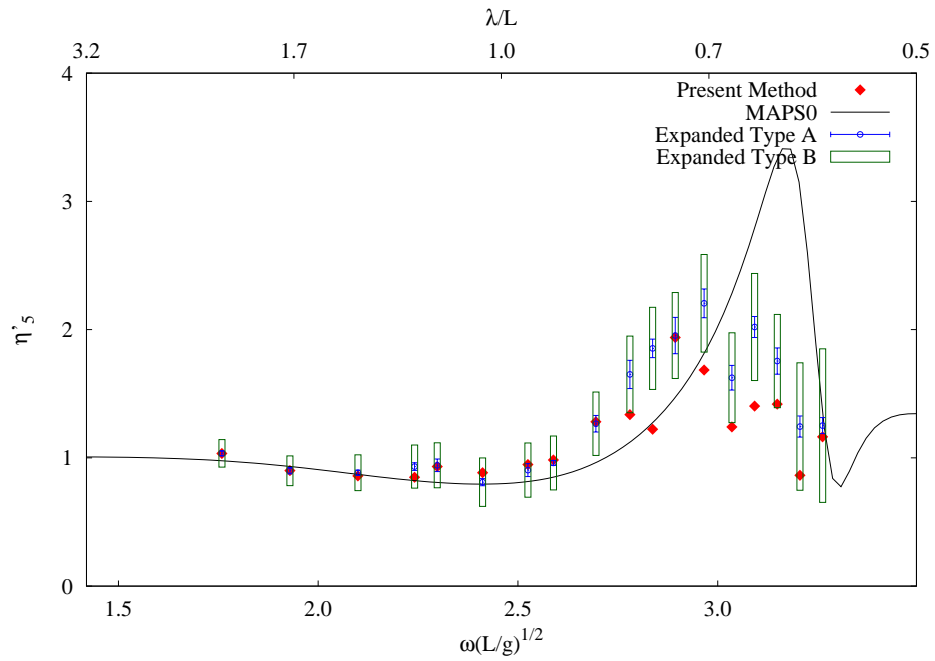


Figure 4.20: Wave Elevation at WP5

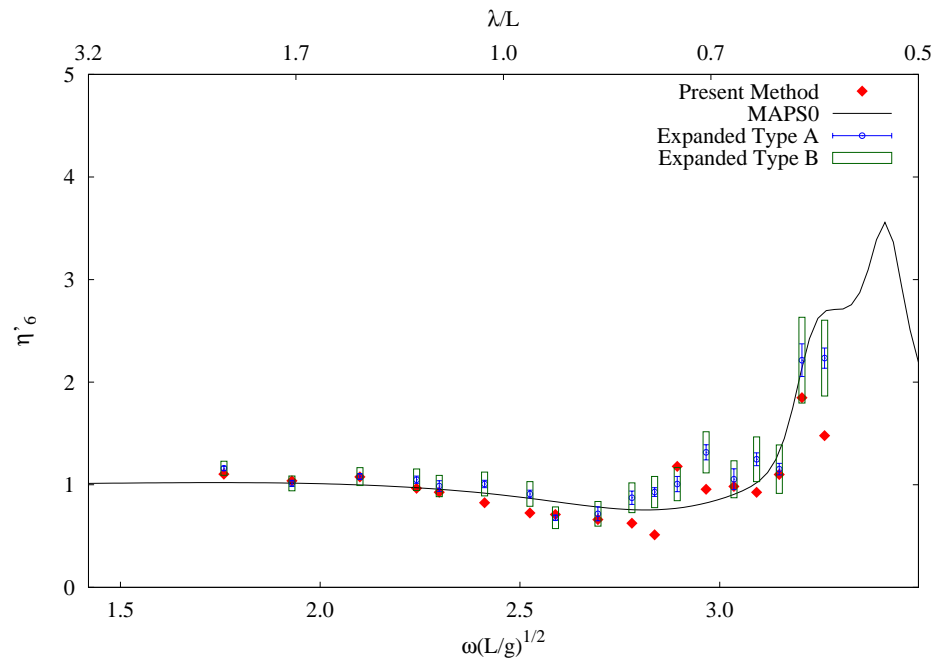


Figure 4.21: Wave Elevation at WP6

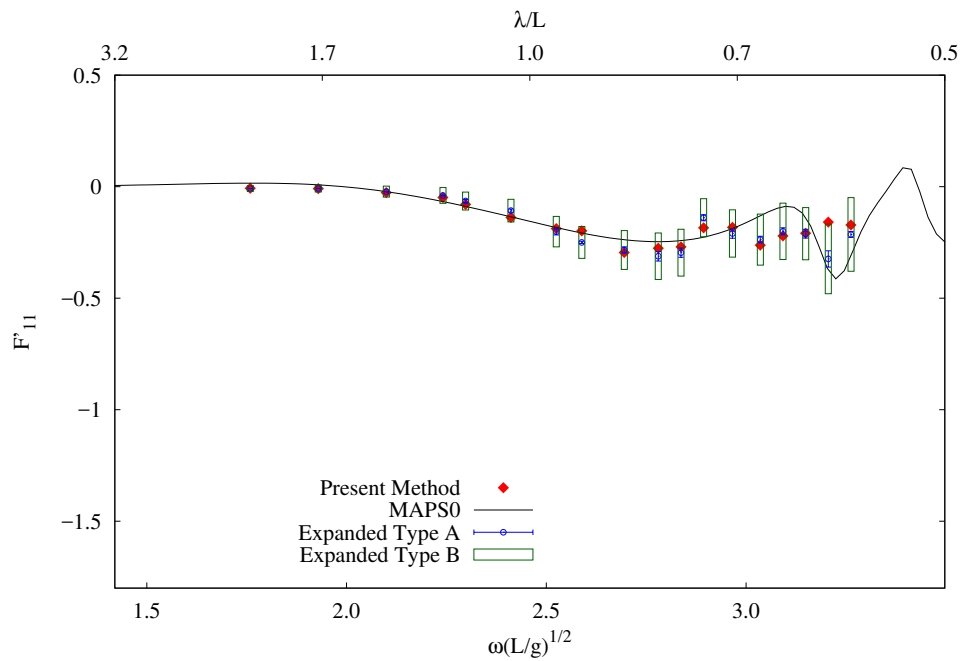


Figure 4.22: Longitudinal Drift Force on Body 1

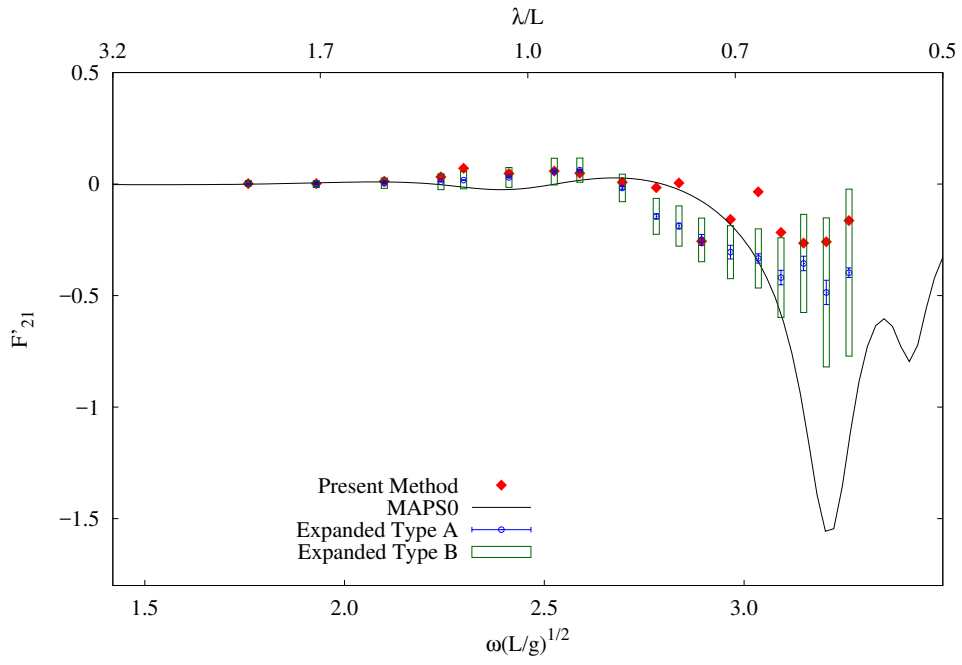


Figure 4.23: Transverse Drift Force on Body 1

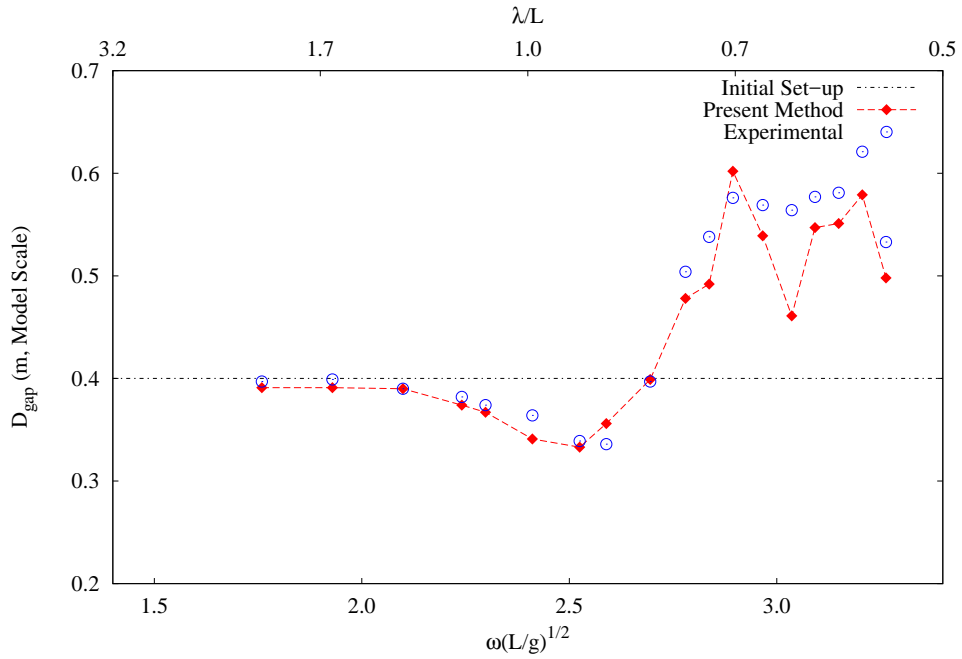


Figure 4.24: Mean Gap Width

wave elevations in the gap at WP5 and WP6 and longitudinal and transverse drift forces on Body 1.

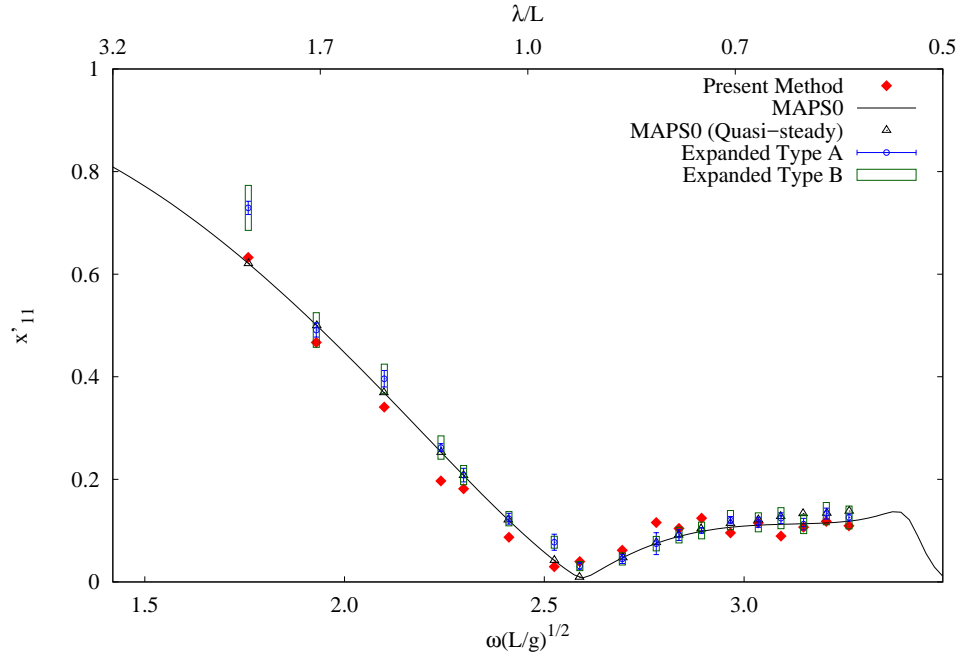


Figure 4.25: Surge Motion of Body 1

As shown in the comparisons, the gap effect is significant. The over-predictions, including wave elevations in the gap and drift forces in the resonance region, were significantly mitigated by the quasi-steady approach in MAPS0. As for the motions, surge, roll and pitch motions are not very sensitive to the change in gap. However, the heave resonance response was shifted to low frequencies. The discrepancies could be caused by various reasons; for example, the fluid viscosity was not accounted in the simulations, and the dynamic gap change in the interactions could not be modelled by the frequency-domain method.

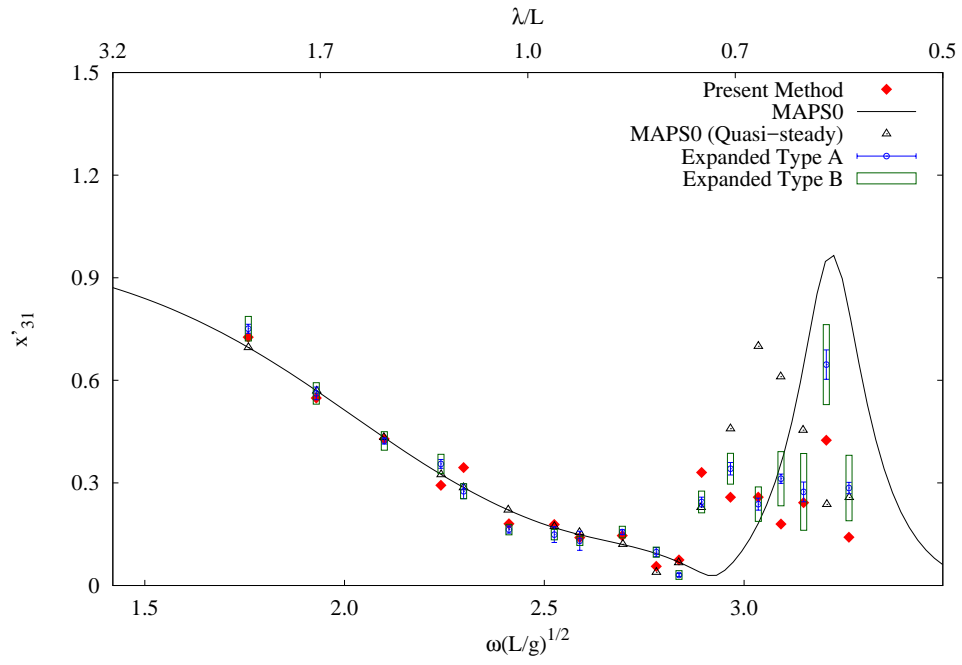


Figure 4.26: Heave Motion of Body 1

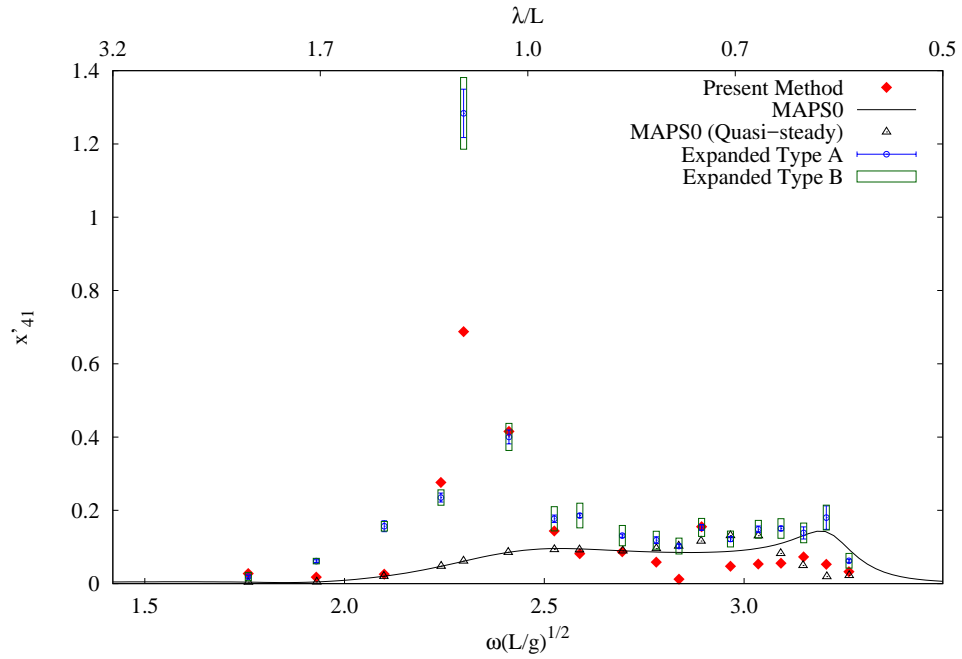


Figure 4.27: Roll Motion of Body 1

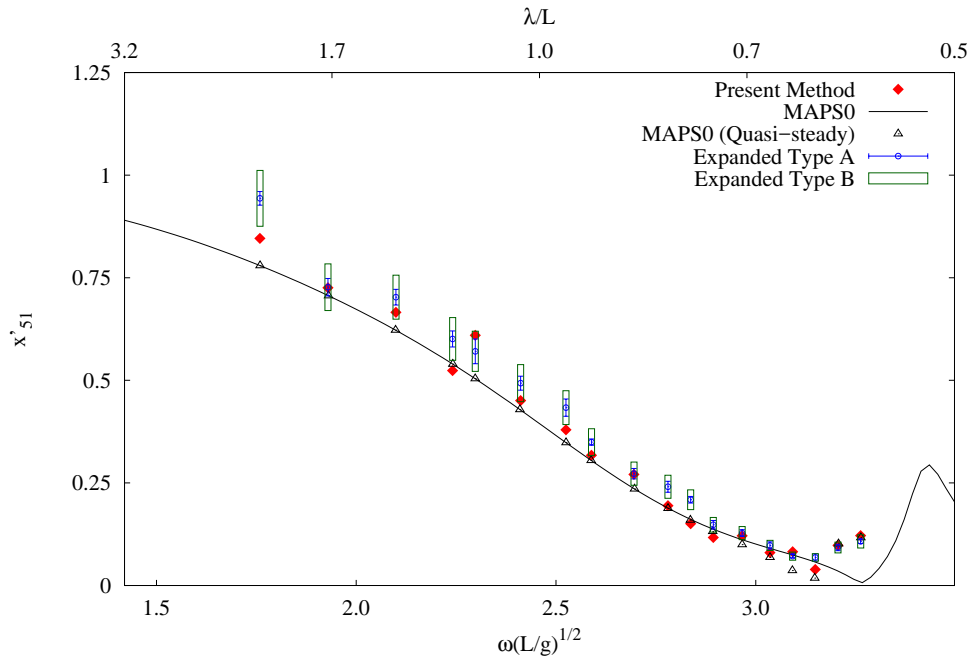


Figure 4.28: Pitch Motion of Body 1

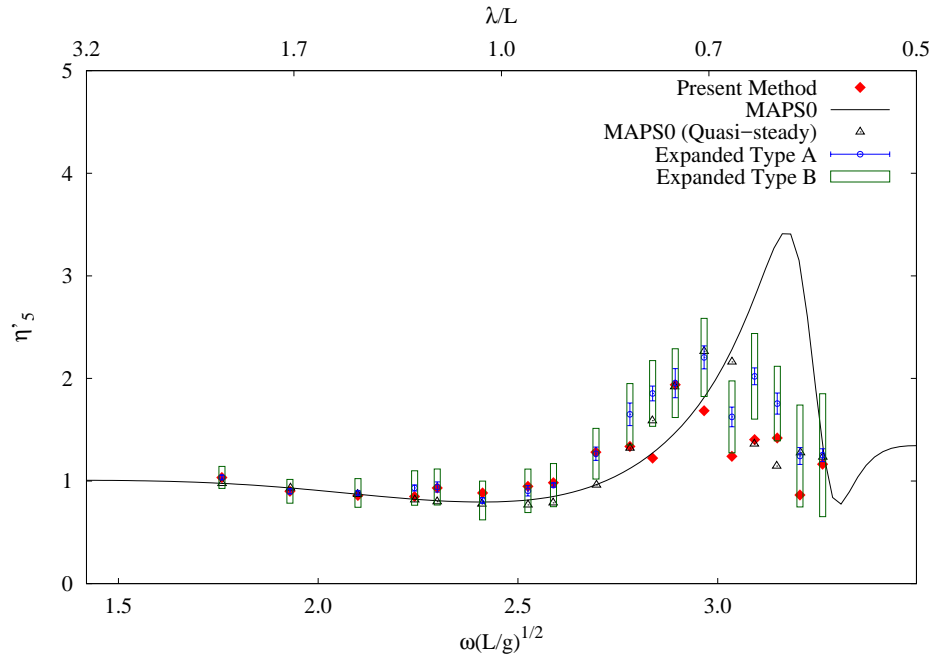


Figure 4.29: Wave Elevation at WP5

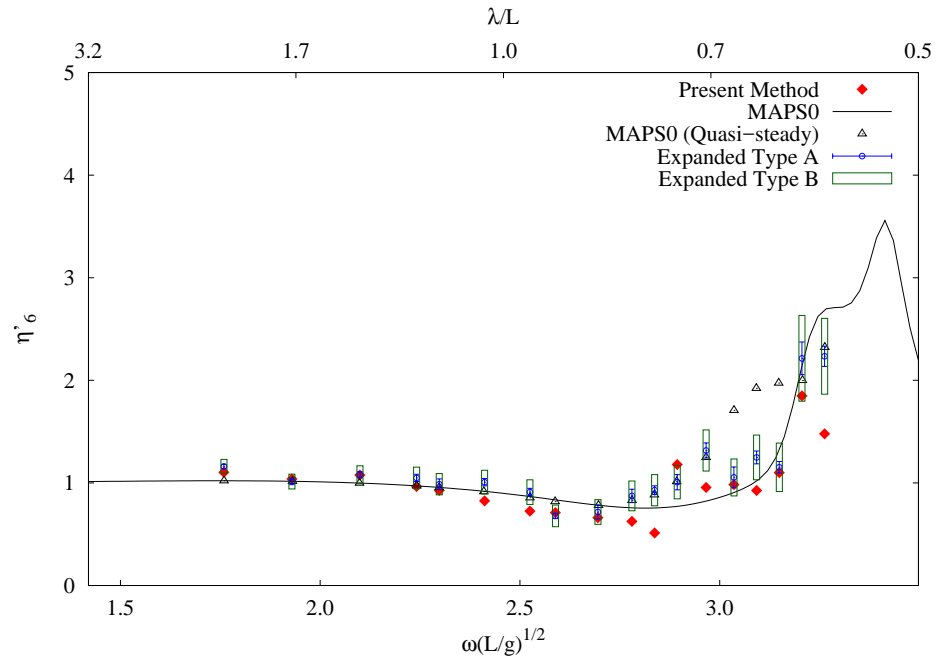


Figure 4.30: Wave Elevation at WP6

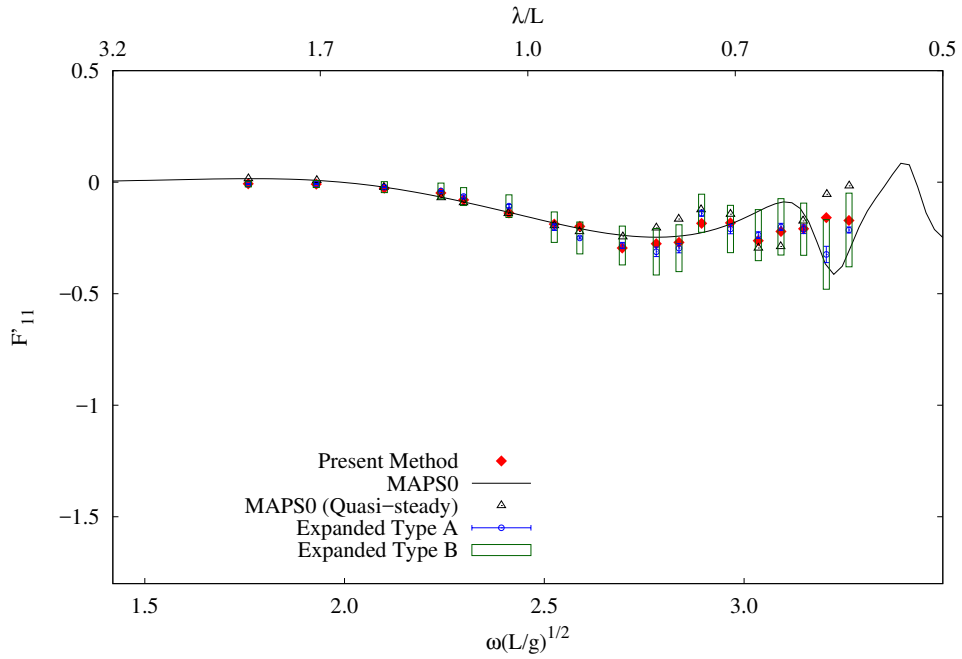


Figure 4.31: Longitudinal Drift Force on Body 1

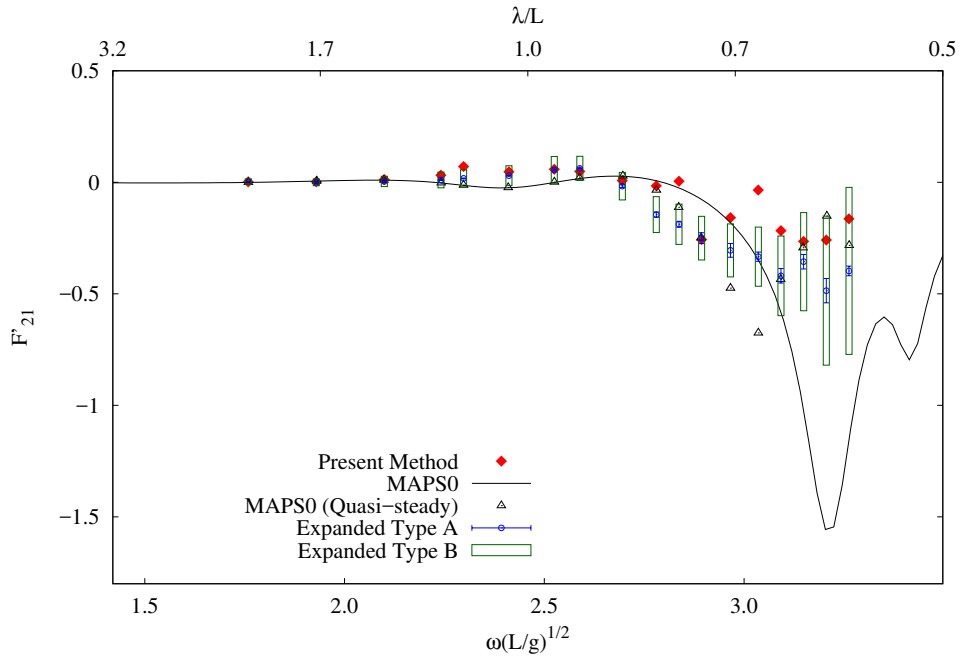


Figure 4.32: Transverse Drift Force on Body 1

4.2 Ship Replenishment in Waves with Forward Speed

To further validate the present method, studies on ship replenishment in waves with forward speed were conducted. As described by McTaggart et al. (2003), a frigate and a supply ship are arranged side-by-side with a gap distance of 30 m and march in head waves at a speed of 12 knots in full scale, as shown in Fig. 4.33. The ship model geometries are available in the work of McTaggart (2017). The particulars of the two vessels and scaled models are presented in Table 4.5. Different replenishment set-ups were also investigated: two ships aligned longitudinally at midships and the frigate 45 m ahead of the supply ship, as shown in Fig. 4.34.

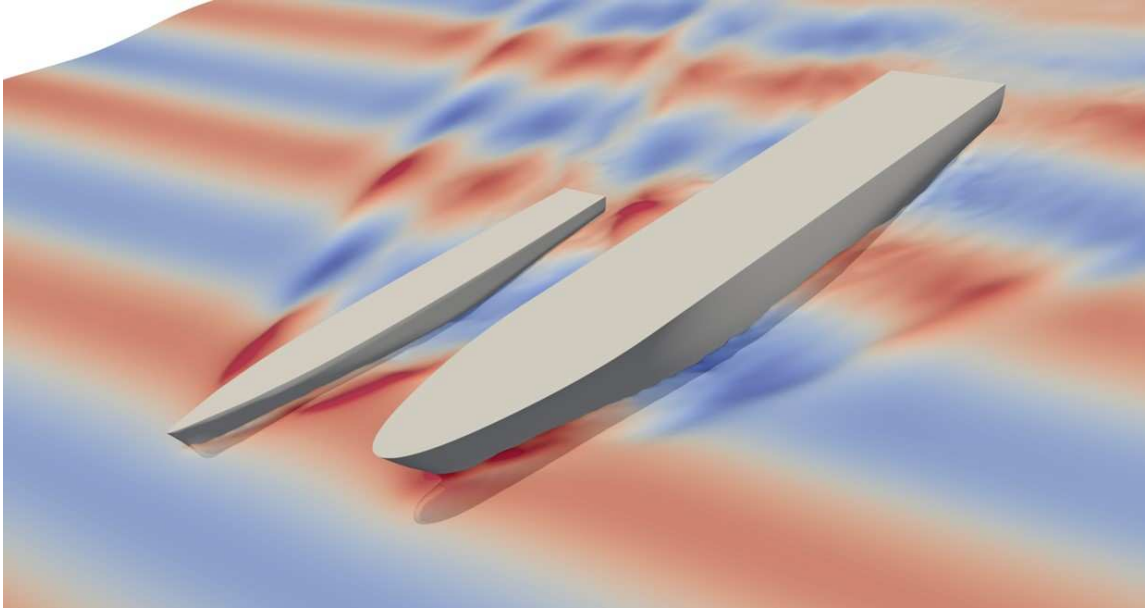


Figure 4.33: Supply Ship and Frigate Models

Table 4.5: Particulars of full-scale ships and models

Parameter	Supply Ship		Frigate	
	Full Scale	1:25 Scale	Full Scale	1:25 Scale
Length (m)	187.5	7.2	122.0	4.88
Breadth (m)	30.6	1.224	14.8	0.592
Draft (m)	8.5	0.34	4.5	0.18
VCG (m)	3.93	0.157	2.06	0.082
r_{xx} (m)	8.0	0.32	4.9	0.196
r_{yy} (m)	45.0	1.8	30.5	1.22

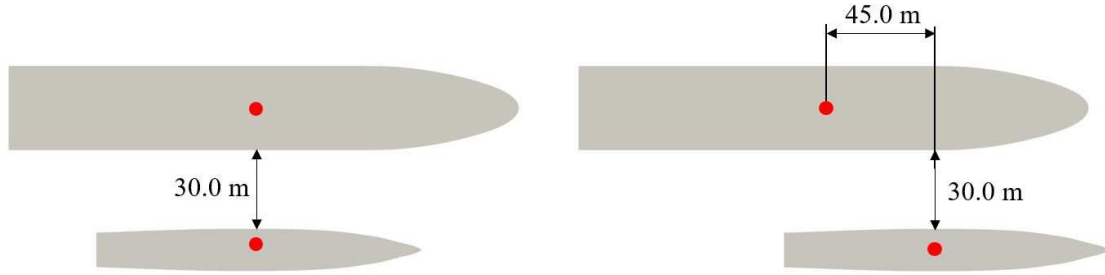


Figure 4.34: Ship Replenishment Set-up

4.2.1 Set-up for CFD Simulations

Simulations on the experiments, conducted at the towing tank of National Research Council Canada (NRC), was carried out with scaled models (1:25) advancing at a forward speed of $U = 1.23$ m/s with a gap of 1.2 m. In the experiment, the two models were semi-captured, i.e., free to heave, roll, and pitch (McTaggart et al., 2003).

As shown in Fig. 4.35, the domain width, B_{tank} , and the depth, D_{tank} , were 12.0 m and 7.0 m, respectively, which were the same as those of the NRC towing tank. Based on the convergence studies (see Appendix B), the inlet relaxation zone, the computational zone, and the outlet wave damping zone were set as 1.0λ , 3.0 times length of the frigate model, and 5.0λ , respectively, where λ is the wavelength. The cell aspect ratio in the wave refinement zone was set as four.

The simulation matrix is presented in Table 4.6, and the wave steepness is $1/40$.

4.2.2 Set-up for Potential-flow Simulations

Simulations were also conducted using the frequency-domain potential-flow program, MAPS0 (Qiu et al., 2006), as introduced in the previous section. The panel-free

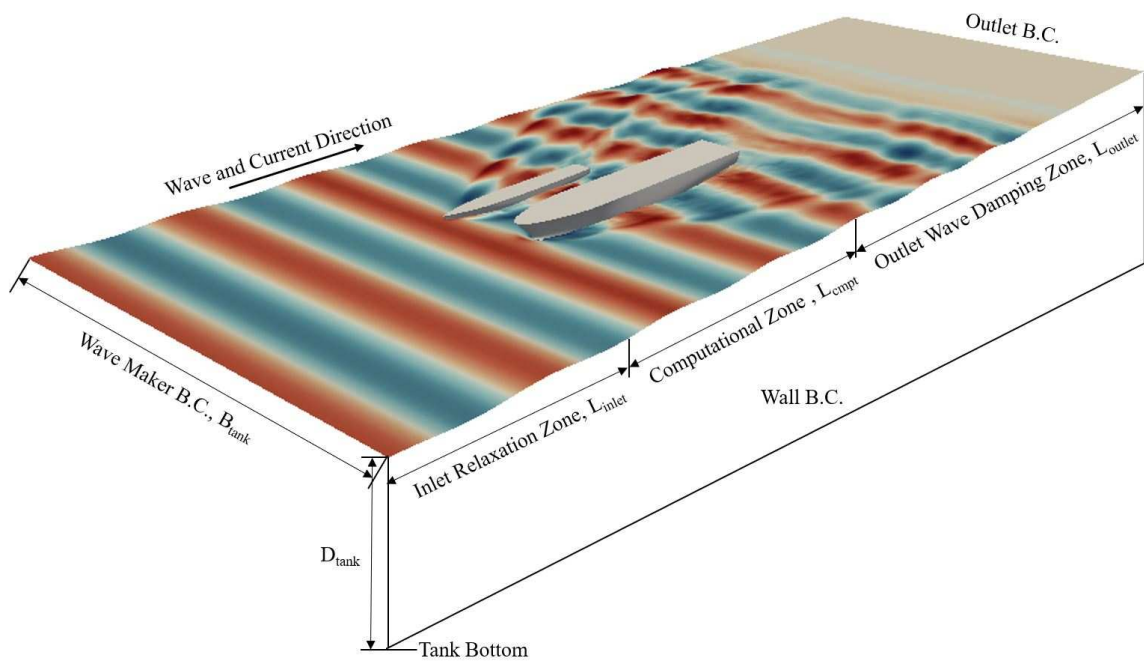


Figure 4.35: Simulation Set-up

Table 4.6: Wave frequencies for the replenishment model tests in model scale

No.	ω (rad/s)	λ/L (Supply Ship)	λ/L (Frigate)
1	2.51	1.30	2.00
2	2.90	0.98	1.50
3	3.18	0.81	1.25
4	3.55	0.65	1.00
5	4.10	0.49	0.75
6	5.03	0.33	0.50
7	7.11	0.16	0.25

method, utilizing the frequency-domain forward-speed Green function, was used to solve the body-wave interactions at forward speed. The simplified m-terms, based on the Neumann-Kelvin assumption, were applied to represent the interactions between the uniform flow and the unsteady wave field (Qiu and Peng, 2007).

Based on the convergence studies, the number of Gaussian points distributed on each ship hull was 774, as shown in Fig. 4.36. The viscous roll damping was set as 5% of critical damping. It is noted that no lid was added for irregular frequency removal, and tank walls were not considered.

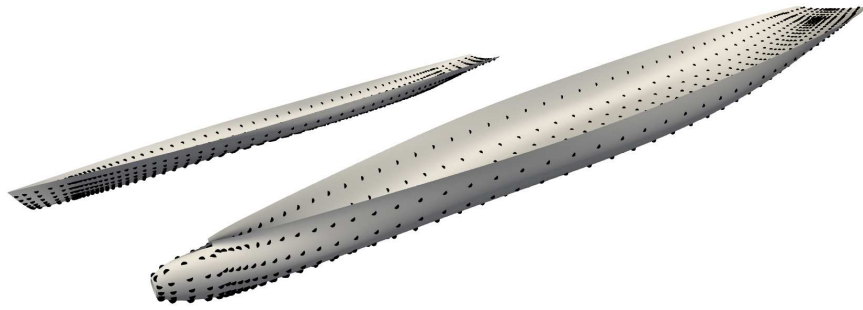


Figure 4.36: Gaussian Point Distribution on Ship Hull Surfaces

4.2.3 Uncertainty Analysis and Convergence Studies

Similar to the zero-speed cases, the GCI method was utilized to analyze the uncertainties in the numerical results, including the heave, roll, and pitch motions of the two ships, due to spatial discretization. Three wave frequencies were investigated, ranging from long to short waves at the model speed of $U = 1.23$ m/s.

Table 4.7 presents the GCI and the intermediate results for the long-wave case

at $U = 1.23$ m/s and $\omega = 2.51$ rad/s ($\lambda/L = 2.0$ for the frigate) with the two ships aligned longitudinally at midships. The motions are non-dimensionalized as $x'_i = x_i/\eta_0$ for $i = 3$; $x'_i = x_i/(k\eta_0)$ for $i = 4, 5$, where i represents the mode, η_0 is the amplitude of incident wave, and k is the wavenumber. The total numbers of cells for the fine, medium, and coarse meshes are 24.3 M, 13.5 M, and 5.7 M, respectively. The corresponding cell sizes are 16.5 cells per frigate draft and 22.3 cells per wave height, 13.2 cells per frigate draft and 17.9 cells per wave height, and 9.9 cells per frigate draft and 13.4 cells per wave height, respectively. The time step size expressed in terms of CFL was kept as 0.1. It is observed that for this long-wave case, the motions of the two vessels are not sensitive to the change in mesh size. Spatial convergence was achieved, and the uncertainties were small.

Figure 4.37 presents the temporal convergence for the motions of frigate and supply ship using CFL 0.1, 0.14 and 0.2 with mesh cell size, h_2 . It can be seen that the predicted motions are not sensitive to the time step as expected.

The GCI and the intermediate results for the medium wave case at $U = 1.23$ m/s and $\omega = 3.18$ rad/s ($\lambda/L = 1.25$ for the frigate) with the frigate positioned ahead of the supply ship are presented in Table 4.8. The time step in terms of CFL was kept as 0.1. The total number of cells for the fine mesh with 14.8 cells per frigate draft and 12.6 cells per wave height, the medium mesh with 11.5 cells per frigate draft and 9.8 cells per wave height, and the coarse mesh with 8.2 cells per frigate draft and 7.0 cells per wave height are 10.3 M, 5.2 M, and 2.2 M, respectively. Spatial convergence can be seen when a fine mesh is used, and uncertainties in heave motion of the frigate and roll motion of the supply ship are larger than those in other motion modes. Those relatively large GCI values suggest that a finer mesh may be used to

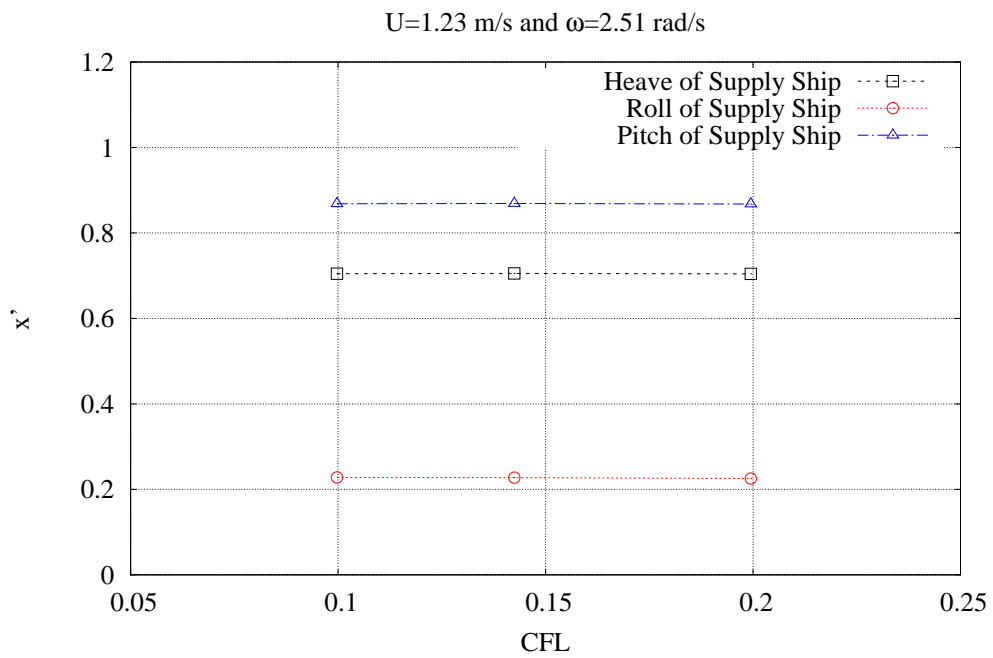
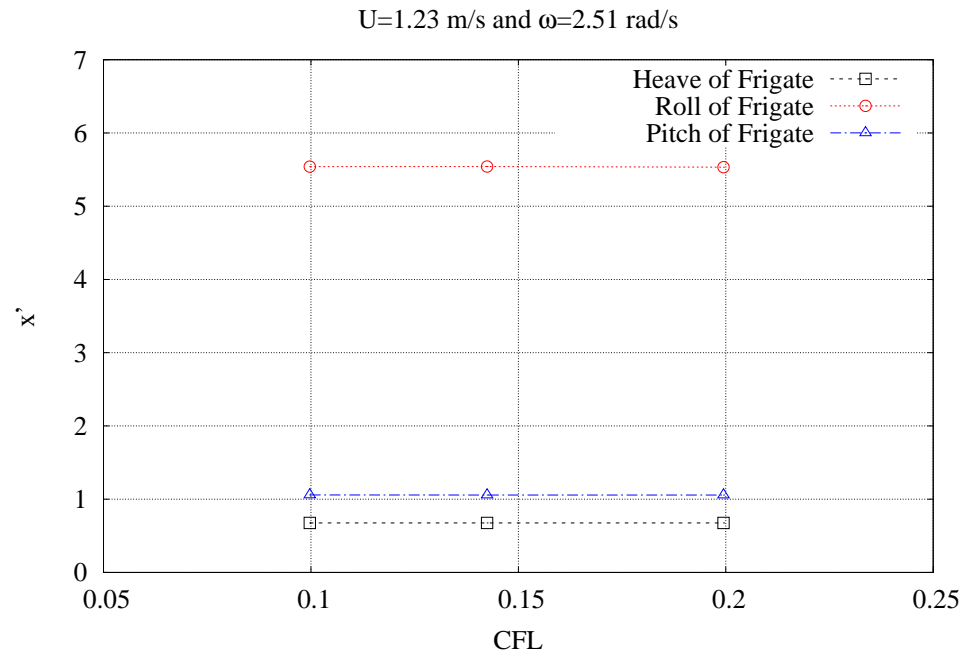


Figure 4.37: Temporal Convergence for Motions of Two Ships from OpenFOAM with Frigate and Supply Vessel Aligned at Midships at $U = 1.23$ m/s and $\omega = 2.51$ rad/s

Table 4.7: Uncertainties in motions of two ships from OpenFOAM with frigate and supply vessel aligned at midships at $U = 1.23$ m/s and $\omega = 2.51$ rad/s

Parameter	x'_3	x'_4	x'_5	x'_3	x'_4	x'_5
$h_1(m)$	0.0109					
$h_2(m)$	0.0137					
$h_3(m)$	0.0182					
ϕ_1	0.6741	5.5040	1.0503	0.7056	0.2329	0.8679
ϕ_2	0.6756	5.5402	1.0577	0.7047	0.2278	0.8684
ϕ_3	0.6734	5.4677	1.0512	0.7083	0.2504	0.8758
CT	O	O	O	O	O	M
p	1.3469	2.6136	0.6608	4.8623	5.4530	9.4367
ϕ_{ext}^{21}	0.6696	5.4583	1.0035	0.7061	0.2350	0.8678
$e_a^{21}(\%)$	0.2299	0.6536	0.7032	0.1374	2.2194	0.0531
$e_{\text{ext}}^{21}(\%)$	0.6613	0.8376	4.6642	0.0699	0.9050	0.0074
$\text{GCI}_{\text{fine}}^{21}(\%)$	0.8193	1.0315	5.5313	0.0876	1.1669	0.0092

reduce uncertainties.

Figure 4.38 presents the temporal convergence for the motions of frigate and supply ship. It can be observed that the predicted motions converge as the time step is decreased, but they are not very sensitive to the time step.

As for the short-wave case when the two ships aligned longitudinally at midships at $U = 1.23$ m/s and $\omega = 4.10$ rad/s ($\lambda/L = 0.75$ for the frigate), the corresponding GCI and the intermediate details are presented in Table 4.9. In these cases, CFL is 0.1, and the numbers of cells for the fine mesh with 21.4 cells per frigate draft and

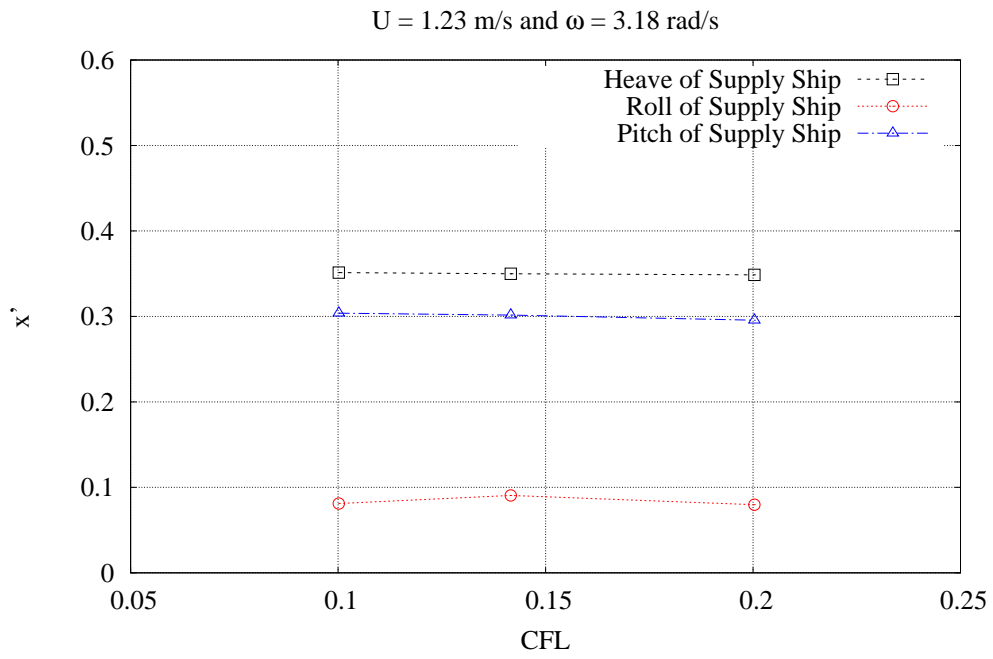
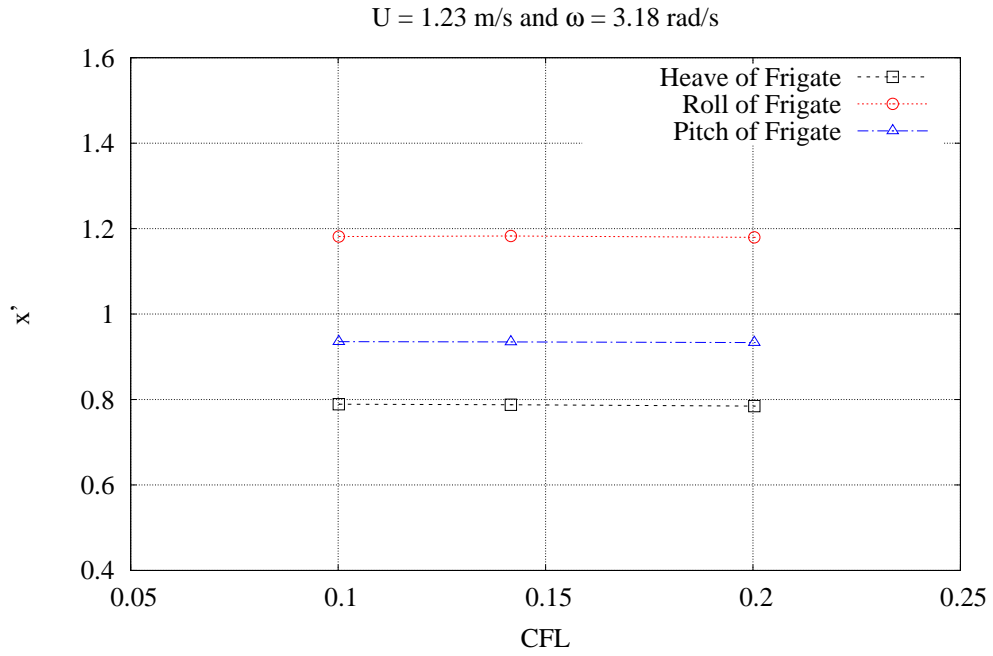


Figure 4.38: Temporal Convergence for Motions of Two Ships with Frigate and Supply Vessel Aligned at Midships from OpenFOAM at $U = 1.23 \text{ m/s}$ and $\omega = 2.51 \text{ rad/s}$

Table 4.8: Uncertainties in motions of two ships from OpenFOAM with frigate ahead of supply vessel at $U = 1.23$ m/s and $\omega = 3.18$ rad/s

Parameter	x'_3	x'_4	x'_5	x'_3	x'_4	x'_5
$h_1(m)$	0.0122					
$h_2(m)$	0.0156					
$h_3(m)$	0.0219					
ϕ_1	0.7976	1.1720	0.9372	0.3588	0.0928	0.3092
ϕ_2	0.7888	1.1816	0.9356	0.3512	0.0812	0.3036
ϕ_3	0.7752	1.1704	0.9148	0.3336	0.1084	0.2896
CT	M	O	M	M	O	M
p	0.6058	0.6431	7.5037	1.9744	2.7712	2.3099
ϕ_{ext}^{21}	0.8500	1.1192	0.9372	0.3700	0.1040	0.3160
$e_a^{21}(\%)$	1.0956	0.7888	0.1638	2.0894	14.2773	1.7554
$e_{\text{ext}}^{21}(\%)$	6.1828	4.7482	0.0292	3.0875	11.0420	2.1454
$\text{GCI}_{\text{fine}}^{21}(\%)$	8.3280	5.6216	0.0366	4.0655	17.7309	2.7886

10.9 cells per wave height, the medium mesh with 16.5 cells per frigate draft and 8.4 cells per wave height, and the coarse mesh with 13.2 cells per frigate draft and 6.7 cells per wave height are 26.1 M, 10.9 M and 6.9 M, respectively. It can be seen that the uncertainty in the heave motion of the supply ship is larger than those in other motions. This is due to the small amplitude of heave in short waves. In comparison with the case of longer wave ($\lambda/L = 2.0$), it can also be seen that the uncertainties in the roll motion are in general reduced by using a finer mesh.

Convergence studies on the time step were further carried out using the mesh size,

Table 4.9: Uncertainties in motions of two ships from OpenFOAM with frigate and supply vessel aligned at midships at $U = 1.23$ m/s and $\omega = 4.10$ rad/s

Parameter	x'_3	x'_4	x'_5	x'_3	x'_4	x'_5
$h_1(m)$	0.0084					
$h_2(m)$	0.0109					
$h_3(m)$	0.0137					
ϕ_1	0.1657	0.1312	0.2580	0.0627	0.0346	0.0362
ϕ_2	0.1719	0.1315	0.2645	0.0606	0.0343	0.0362
ϕ_3	0.1839	0.1323	0.2559	0.0579	0.0336	0.0368
CT	M	M	O	M	M	M
p	3.0990	3.8985	1.2214	1.1044	3.8756	22.1173
ϕ_{ext}^{21}	0.1600	0.1310	0.2387	0.0700	0.0348	0.0362
$e_a^{21}(\%)$	3.6141	0.2540	2.4473	3.5713	0.8837	0.0110
$e_{\text{ext}}^{21}(\%)$	3.5945	0.1685	8.1006	10.3597	0.5806	0.0001
$GCI_{\text{fine}}^{21}(\%)$	4.1805	0.2097	9.1378	14.9621	0.7364	0.0001

h_2 , and three CFL , 0.1, 0.14, and 0.2. The temporal convergence is shown in Fig. 4.39. Motions of the frigate and the supply vessel converged as the time step was decreased.

Based on the convergence studies and uncertainty analysis, the following settings were chosen as best-practice parameters: at least ten cells per ship model draft in the body refinement zone, at least eight cells per wave height, the cell aspect ratio of four in the wave refinement zone, minimum five wavelengths for the outlet wave damping zone, and $CFL < 0.14$.

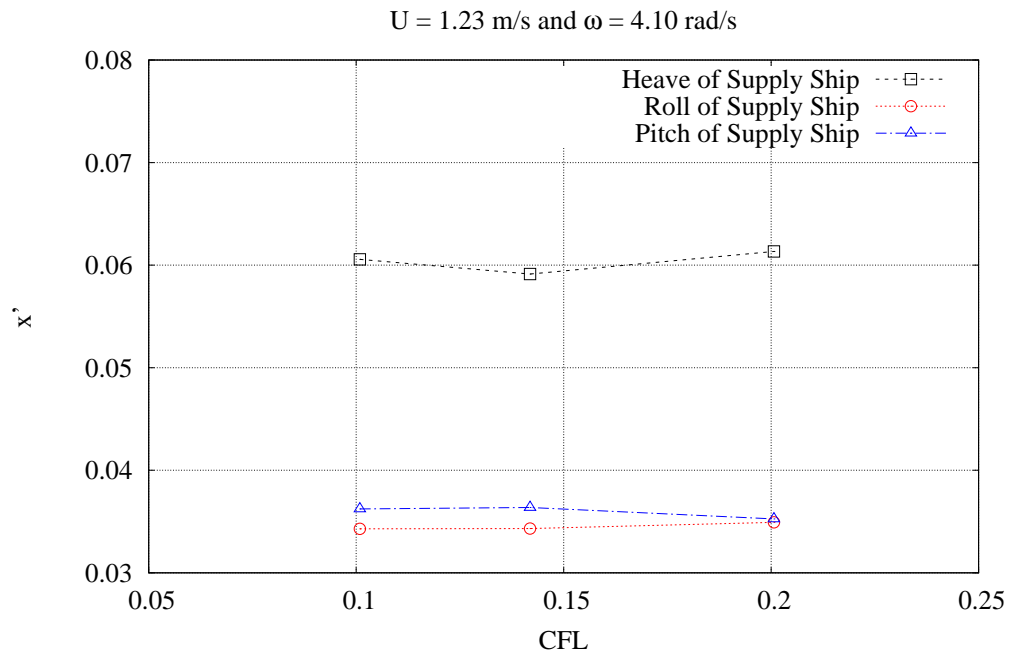
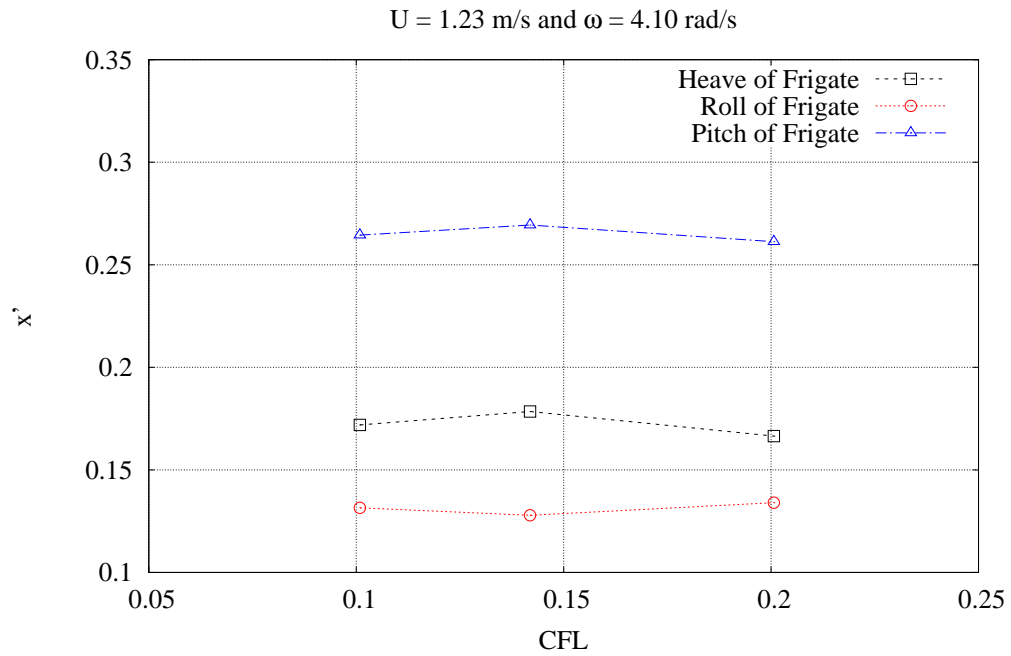


Figure 4.39: Temporal Convergence for Motions of Two Ships from OpenFOAM with Frigate and Supply Vessel Aligned at Midships at $U = 1.23 \text{ m/s}$ and $\omega = 4.10 \text{ rad/s}$

4.2.4 Validation Studies

Validation studies were performed based on best-practice settings. As examples, Figs. 4.40 and 4.41 present the time histories of motions for the frigate and the supply ship at $\omega = 3.18$ rad/s for the two side-by-side arrangements. The pitch motions are out of phase when the frigate is ahead of the supply ship, resulting in larger relative motions between the two ships, and green water on the deck of the frigate is observed when the two ships are aligned at midships (see Fig. 4.42).

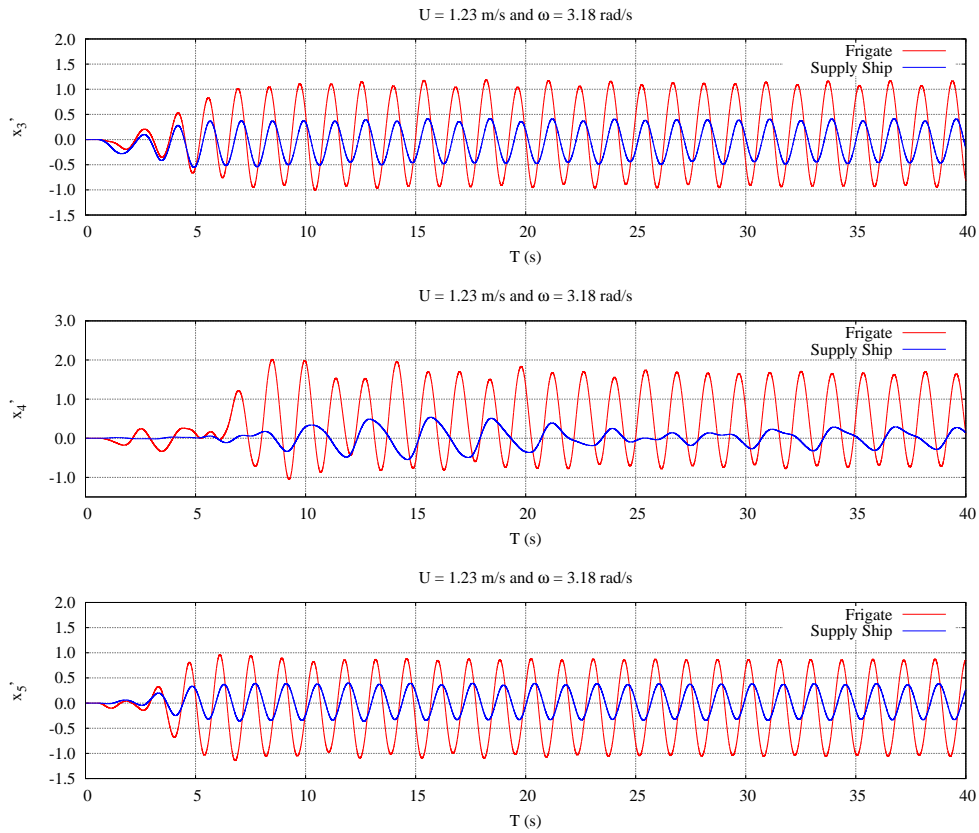


Figure 4.40: Time Series of Motions for Two Ship Models from OpenFOAM at $U = 1.23$ m/s and $\omega = 3.18$ rad/s - Aligned Longitudinally at Midships

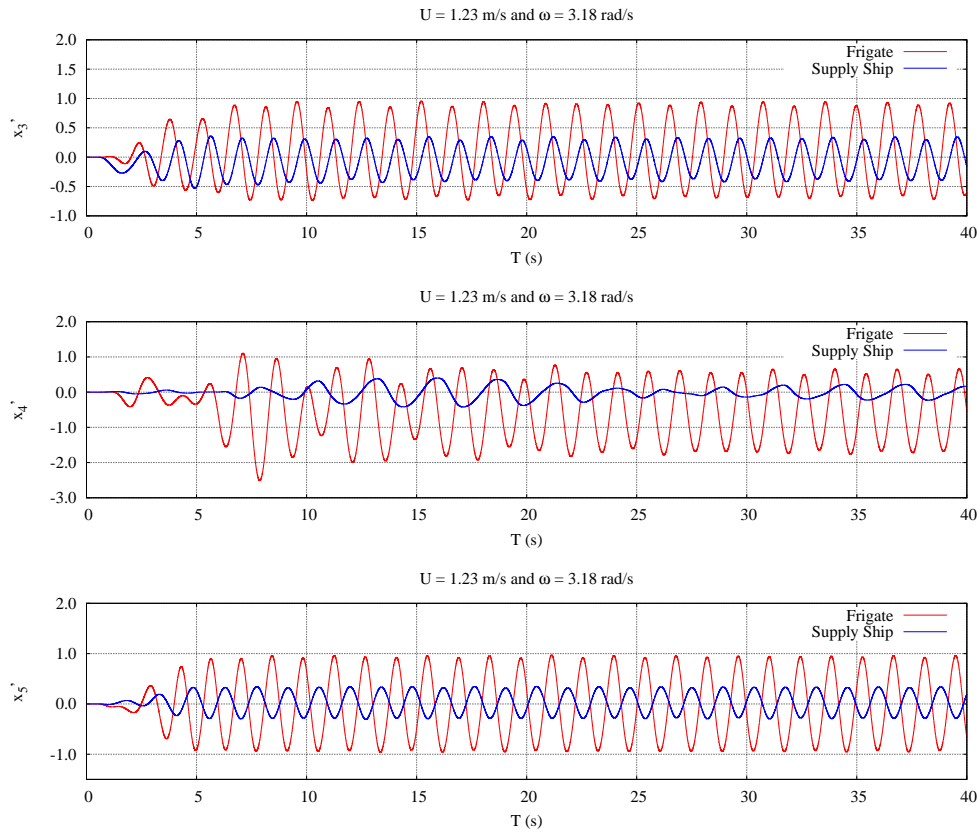


Figure 4.41: Time Series of Motions for Two Ship Models from OpenFOAM at $U = 1.23$ m/s and $\omega = 3.18$ rad/s - Frigate ahead of Supply Ship

The predicted motions of the two ships at all the wave frequencies and with both side-by-side arrangements are compared with the potential-flow results from MAPS0 and the experimental data from McTaggart et al. (2003). Figs. 4.43 - 4.45 present the non-dimensional heave, roll and pitch motions of the two ships.

As observed from the comparisons, both the CFD method and the potential-flow method produced predictions that agree well with the experimental data.

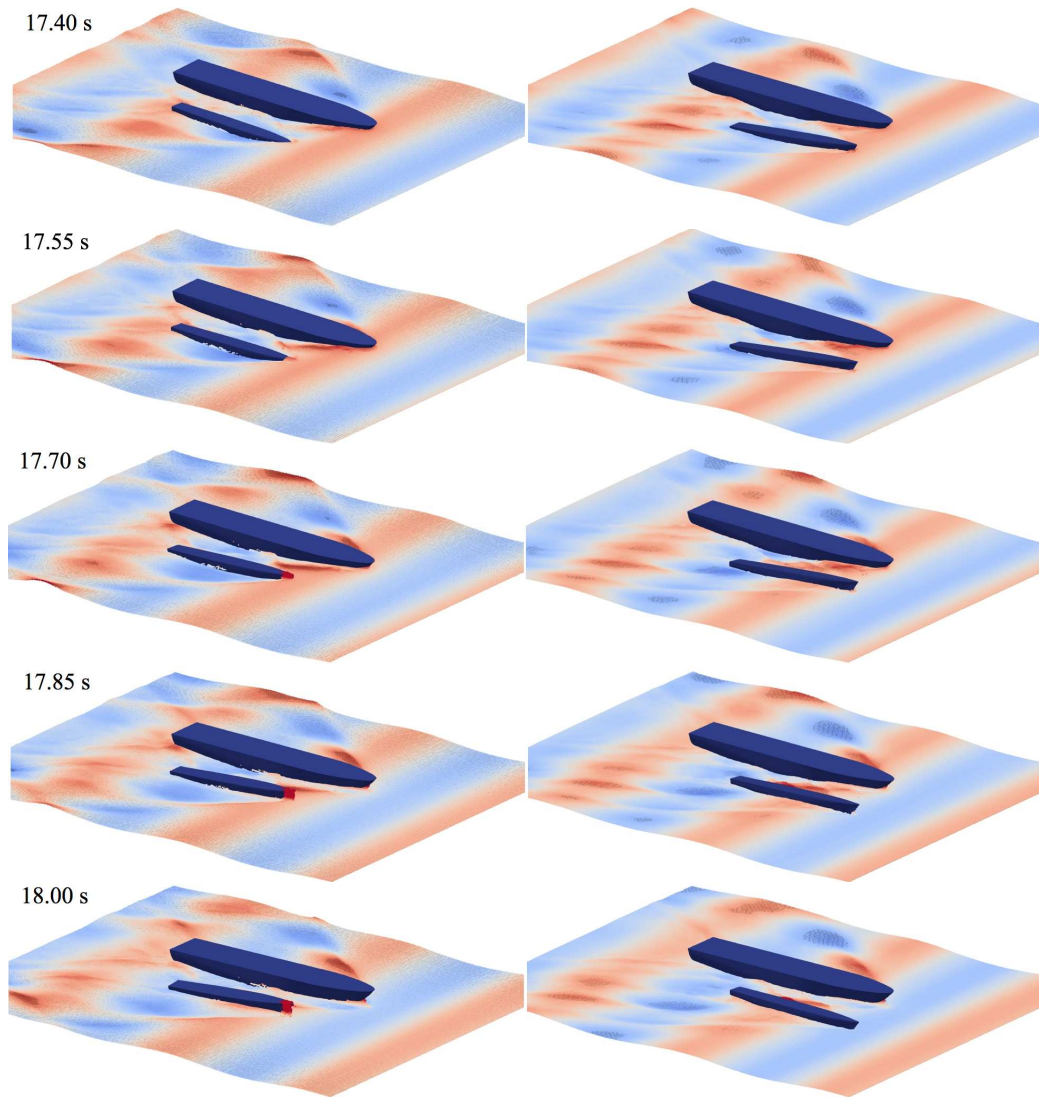


Figure 4.42: Two Ships in Waves at $U = 1.23$ m/s and $\omega = 3.18$ rad/s - Aligned Longitudinally at Midships (left) and Frigate ahead of Supply Ship (Right)

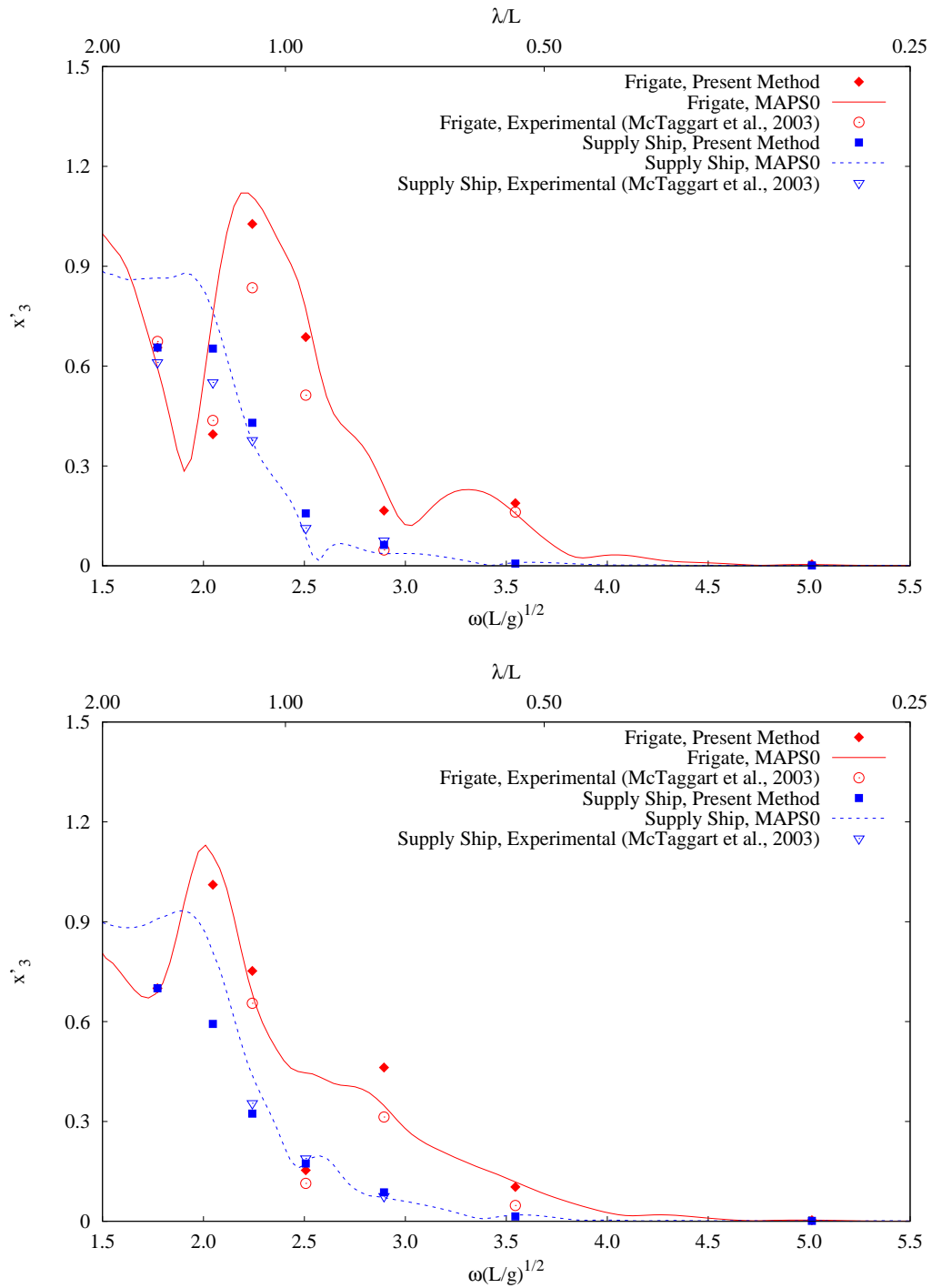


Figure 4.43: Heave Motions of Two Ships in Two Side-by-Side Arrangements - Aligned Longitudinally at Midships (Top) and Frigate ahead of Supply Ship (Bottom)

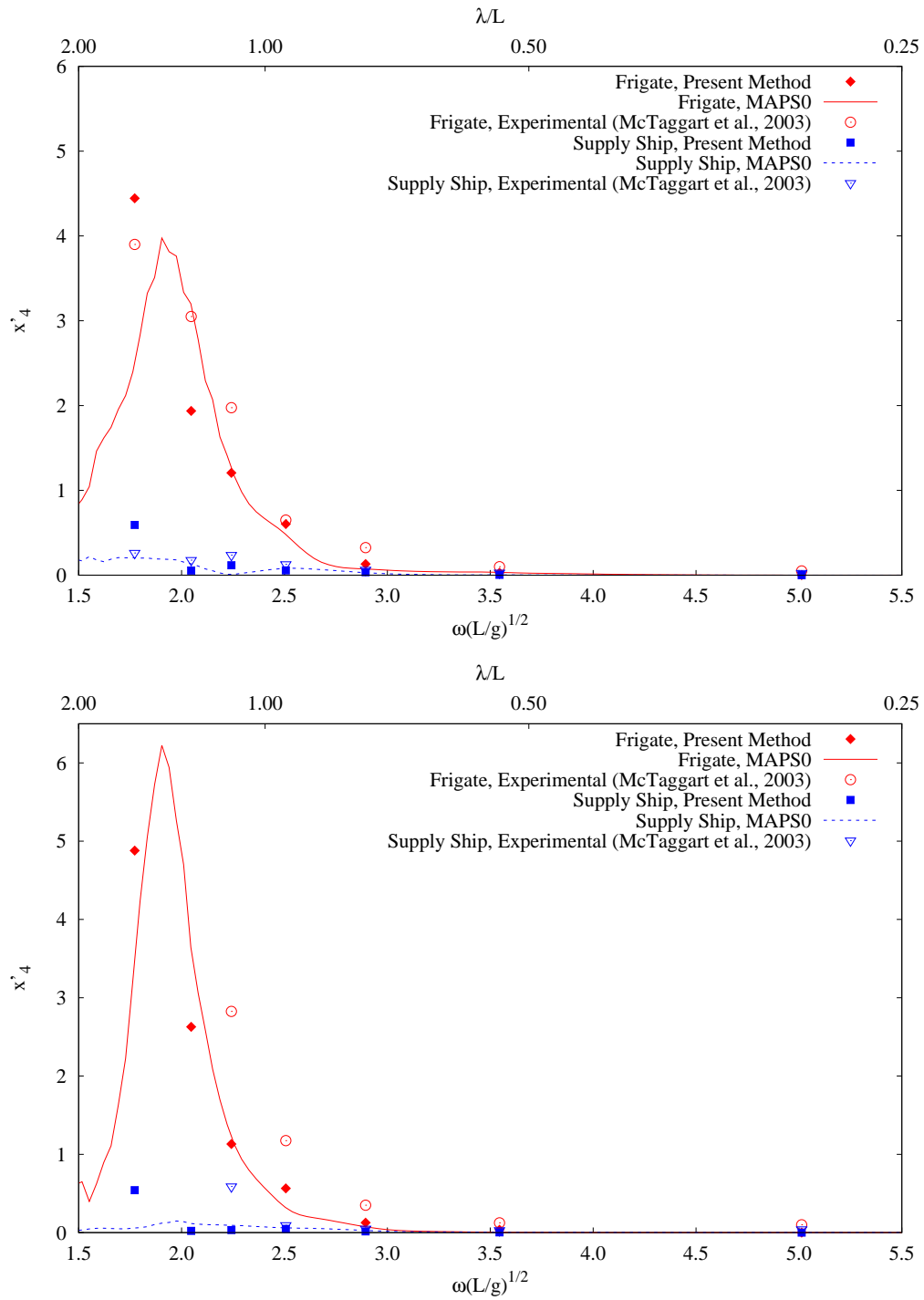


Figure 4.44: Roll Motions of Two Ships in Two Side-by-Side Arrangements - Aligned Longitudinally at Midships (Top) and Frigate ahead of Supply Ship (Bottom)

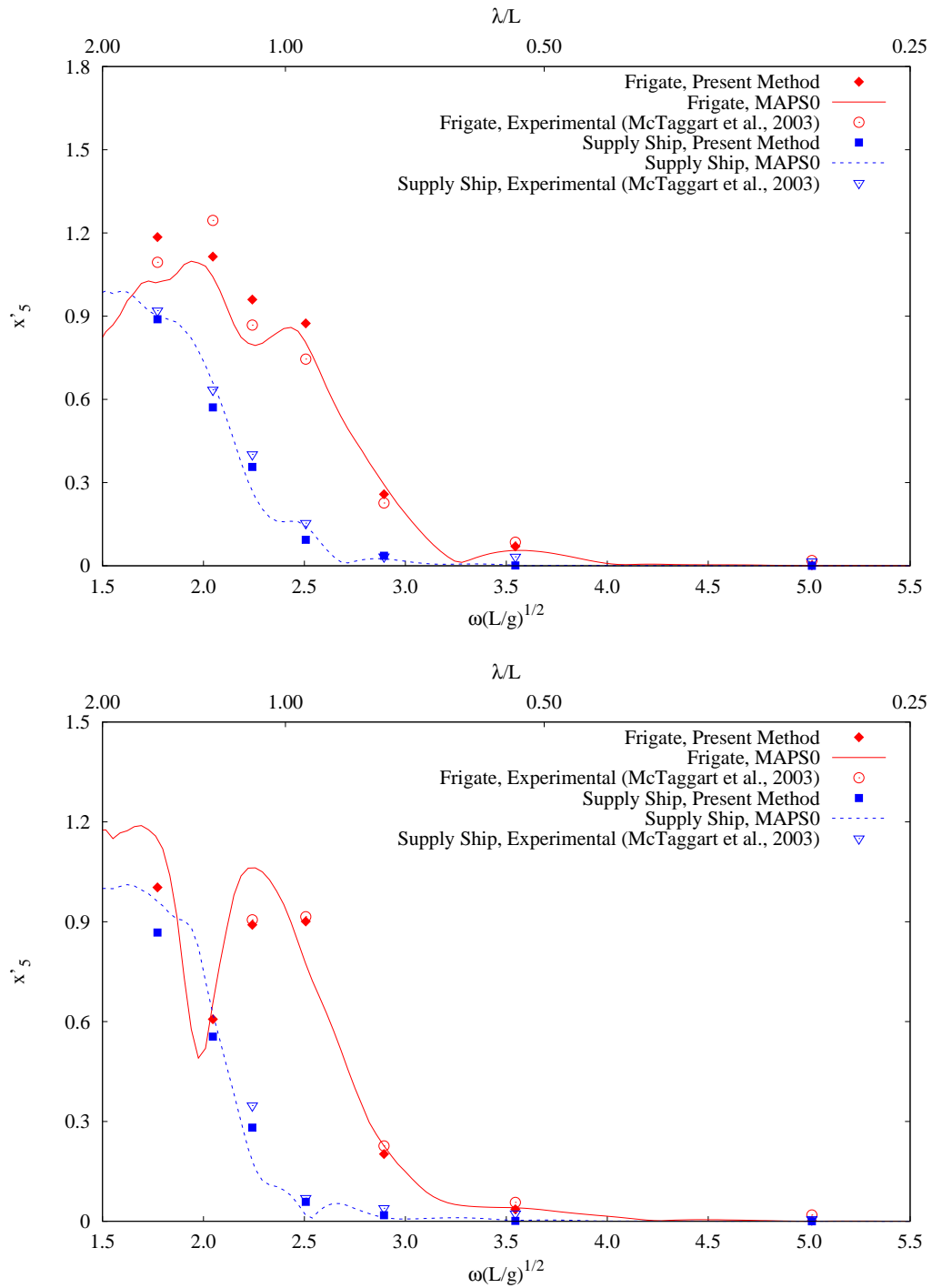


Figure 4.45: Pitch Motions of Two Ships in Two Side-by-Side Arrangements - Aligned Longitudinally at Midships (Top) and Frigate ahead of Supply Ship (Bottom)

4.3 Summary

Numerical simulations on two-body interactions in waves were performed using the present CFD solver, introduced in Chapter 2, and the potential-flow program, MAPS0. Two sets of floating bodies were involved in the simulations, including two FPSOs at zero speed and two ships during underway replenishment at a moderate speed.

Best-practice settings for wave modelling and simulation using the present solver were first determined from convergence studies and uncertainty analysis. It is found that uncertainties in the results due to spatial discretization are relatively larger for responses in short waves. For the zero-speed cases, similar to the model tests, the higher uncertainties could be caused by complexities of the interactions in the resonance region; on the other hand, for cases at moderate forward speed, ship motions in short waves are small in amplitude, leading to more significant uncertainties. Finer grids are recommended for simulations in the resonance region for the zero-speed cases.

Validation studies were then conducted. For the zero-speed cases, the predicted body motions, wave elevations in the gap, and drift forces on the bodies are in good agreement with the test data. Small discrepancies were observed, which could be caused by the reflected waves in model tests. In the present method, the wave damping zone was set long enough so that no waves could be reflected from the outlet boundary; on the other hand, in the physical model tests, reflected waves could be generated at the damping beach. For the forward-speed cases, the predicted heave, roll, and pitch motions are in a good agreement with experimental data.

Simulations were also conducted using the potential-flow program, MAPS0, in the

frequency-domain. For the zero-speed cases, artificial damping for the free surface in the gap and for the roll motion was excluded purposefully to investigate the viscous effects in the two-body interaction problem. As expected, large discrepancies were observed compared to the model test data and the CFD results. Moreover, the constant gap used in frequency-domain simulations may also contribute to the discrepancies. In the model tests and CFD simulations, the gap width, however, varied due to transverse drift forces during interactions, especially in the resonance region. To investigate the gap effect, a quasi-steady approach was used in the MAPS0 simulations, where the gap distance between the two bodies was set according to the mean sway motions of the models in the experiment. The results were significantly improved for wave elevations in the gap and drift forces, indicating the importance of considering gap change. A frequency shift of the resonance heave motion was observed; the reasons could be the ignorance of viscous effects and the mean body positions used in the frequency-domain simulations.

As for the two-body interactions at a moderate speed, both CFD and potential-flow results agree well with the experimental data.

The solver requires minimal effort for mesh generation since the background mesh only contains refinement zones near the bodies and the free surface. The mesh remains constant during the simulations; thus, no field interpolation due to mesh morphing or mesh moving is involved. Benefited from the constant mesh, the solver is robust and stable. For each zero-speed case, 120 seconds of simulation was performed, corresponding to 90, 110 and 130 wave periods for a long-, a medium- and a short-wave case, respectively. In the forward-speed cases, 60 seconds of simulation was conducted for each case, corresponding to 30, 40 and 60 wave periods for a long-, a medium-

and a short-wave case, respectively. During the simulations, no instability issue has been encountered.

As for the computational speed, using a typical mesh with about 10 M cells and setting CFL to 0.15, approximately 10, 11 and 12 wave periods can be obtained for a long-, a medium- and a short-wave case with zero-speed, respectively, within a day using 240 cores (Intel Xeon Gold 6248, 2.5GHz). As for the forward-speed cases, approximately 7, 10 and 15 wave periods can be achieved for a long-, a medium- and a short-wave case, respectively, using the same computational resources.

Elements of the simulations presented in this chapter were also published in the work of Meng and Qiu (2019) and Meng et al. (2020).

Chapter 5

Conclusions and Future Work

5.1 Conclusions

This thesis presents numerical and experimental studies on the hydrodynamic interactions of two floating bodies in close proximity. An immersed boundary method has been implemented in OpenFOAM. A geometric VOF method is utilized to capture the free surfaces, in which sharp air-water interface and mass conservation are preserved. Wave modelling is realized by using the relaxation zone approach. The flow solver can handle large motions of multiple bodies, and it is used to simulate two-body interactions in waves with and without forward speed.

Experiment on two-body interactions in waves at zero forward speed was conducted to validate the present solver and to provide benchmark test data. Two identical box-like FPSO models were arranged side-by-side in a towing tank and were free to oscillate in 6-DOF. Motions of the bodies, wave elevations in the gap, and drift forces were measured, and all the test runs were repeated five times. Sources of un-

certainties in the experiment were identified, and comprehensive uncertainty analysis on the test results was conducted based on the ISO-GUM methodology. A combined experimental and numerical approach was developed to estimate the uncertainties due to model properties and experimental set-up. It was found from numerical simulations that uncertainties due to the model geometry are negligible. However, uncertainties due to the model mass properties are relatively significant, especially for roll motions. The uncertainty in the gap width leads to large uncertainties in all results since it is closely related to the gap resonance frequency. The Type B uncertainties are, in general, higher than the Type A ones. Sensors with a smaller range of capacity and higher sensitivity are desirable to decrease the Type B uncertainty levels. Also, measurements near the resonance frequency showed more significant uncertainties than those at other frequencies.

As for numerical simulations, convergence studies were first performed to determine the best-practice settings for wave modelling. The toolbox, `waves2Foam`, is adopted in the present solver, where the explicit relaxation approach is utilized with an exponential weight function. It is recommended that the outlet wave damping zone should be no shorter than five times the wavelength, and the cell aspect ratio in the free surface refinement zones should be less than four. Validation studies were then carried out for two-body interactions with and without forward speed. Uncertainty analysis of the simulation results due to spatial discretization indicated relatively higher uncertainties for short-wave cases, which is similar to the observations in the model tests. Since high-frequency waves lie in the resonance region for the zero-speed cases, finer grids are recommended for simulations. Comparisons between numerical and experimental results showed good agreement.

Two-body interactions were also simulated using a potential-flow program in the frequency-domain. For the zero-speed cases, artificial damping for the free surface in the gap and for the roll motion was excluded purposefully to investigate the viscous effects in the two-body interaction problem. Compared to the model test data and the CFD results, large discrepancies were observed as expected. Further, as noticed in both experiments and CFD simulations, the gap width varied due to transverse drift forces during interactions. To investigate the gap effect, a quasi-steady approach was used in the potential-flow simulations, where the gap distance between the two bodies was set according to the mean sway motions of the models in the experiment at each test frequency. Compared to the results applying a constant gap distance for all wave frequencies, the results were significantly improved for wave elevations in the gap and drift forces, indicating the importance of considering gap change. A frequency shift of the resonance heave motion was observed, and it could be caused by various reasons. For instance, the viscous effects were ignored, and dynamic gap changes could not be considered appropriately in the frequency-domain simulations.

As for the underway replenishment of two ships at a moderate speed, the CFD results agree well with both experimental data and potential-flow results.

5.2 Future Work

The following aspects need to be addressed in future work.

5.2.1 Numerical Aspects

Computation efficiency The present flow solver utilizes static mesh and deploys refinements around the whole floating bodies. For the zero-speed cases in the resonance region, large sway motions due to transverse drift forces were observed (see Chapter 4), leading to a large body refinement zone. Adaptive mesh refinement (AMR) could be used to reduce the number of cells by only refining the mesh near the immersed boundaries, which may, in turn, speed up the simulations. Improvements can also be made by applying combined potential flow and viscous flow methods, such as the domain decomposition method and the Spectral Wave Explicit Navier-Stokes Equations (SWENSE) approach.

Turbulence modelling The present flow solver is based on laminar flow, which is proved accurate in simulating the two-body interaction problem with and without forward speed in the model scale. Further development of turbulence modelling could be made to investigate the turbulence effect.

Quantification of artificial damping coefficient As mentioned in Chapter 1, potential-flow methods are widely used in by the industry, and the over-predictions in two-body interaction problems can be alleviated by introducing artificial damping to the free surface in the gap. However, values of the damping coefficients are difficult to determine and need to be tuned based on model test or CFD simulation data. The present immersed boundary method well predicted two-body interactions in waves; thus, the flow solver can be further used to quantify the damping coefficients via extensive simulations. Two floating bodies with different gap distances and

different shapes could be investigated to quantify the artificial damping coefficients for arbitrary geometries.

Time-domain simulation using body-exact potential flow methods The numerical results indicated that considering the change of gap distance due to transverse drift forces is important in the prediction of two-body interactions (see Chapter 4). Time-domain simulations considering large body motions are suggested to quantify the viscous and damping effects further.

Frequency-domain simulation considering wall effects The quasi-steady approach used in the potential-flow method was successful in alleviating the over-predictions in wave elections in the gap and drift forces in the resonance region. However, the resonance response of heave motion shifted to low frequencies (see Chapter 4). Further investigations on wall effects are recommended.

5.2.2 Experimental Aspects

Wall effect In the present model test, the towing tank is 4.6 m wide, which may lead to wall effects. To quantify the wall effects, further model tests in a larger towing tank or a wave basin using the same models are suggested. More repeats for the cases in the resonance region are also recommended.

Scale effect Model tests using larger scaled models (currently 1:60) are recommended to investigate the scale effect.

Bibliography

- [1] D. W. Braudaway. Uncertainty specification for data acquisition devices (DAQ). In *Proceedings of the IEEE 20th Instrumentation and Measurement Technology Conference, Vail, Colorado, USA*, pages 946–950. Institute of Electrical and Electronics Engineers, 2003.
- [2] B. Buchner, A. van Dijk, and J. de Wilde. Numerical multiple-body simulations of side-by-side mooring to an FPSO. In *Proceedings of the 11th International Offshore and Polar Engineering Conference, Stavanger, Norway*, pages 343–353, June 2001.
- [3] T. Bunnik, W. Pauw, and A. Voogt. Hydrodynamic analysis for side-by-side of-flooding. In *Proceedings of the 19th International Offshore and Polar Engineering Conference, Osaka, Japan*, pages 648–653, July 2009.
- [4] I. B. Celik, U. Ghia, P. J. Roache, and C. J. Freitas. Procedure for Estimation and Reporting of Uncertainty Due to Discretization in CFD Applications. *Journal of Fluids Engineering*, 130(7):1–4, 2008.
- [5] X. Chen. Hydrodynamics in offshore and naval applications—Part I. In *Keynote Lecture of the 6th International Conference on Hydrodynamics, Perth, Australia*,

November 2004.

- [6] X. Chen, R. Zhu, and Y. Yang. Time-domain analysis of motion responses of side-by-side vessels during offshore installations and underway replenishment. *International Journal of Offshore and Polar Engineering*, 28(1):19–30, 2018.
- [7] W. E. Cummins. The impulse response function and ship motions. In *David Taylor Model Basin, Washington DC, USA*, pages 1–9, October 1962.
- [8] D. G. Danmeier. *A higher-order method for large-amplitude simulations of bodies in waves*. Ph.D. thesis, massachusetts institute of technology, 1999.
- [9] Q. Dong, H. Lu, J. Yang, and X. Guo. Dynamic gangway responses between tlp and semi-submersible platform during tender-assisted drilling. *Marine Structures*, 67:1–21, 2019.
- [10] B. Elie, G. Reliquet, P.-E. Guillerm, O. Thilleul, P. Ferrant, L. Gentaz, and A. Ledoux. Simulation of the gap resonance between two rectangular barges in regular waves by a free surface viscous flow solver. In *Proceedings of the 32nd International Conference on Offshore Mechanics and Arctic Engineering, Nantes, France*, pages 1–9, June 2013.
- [11] E. Fadlun, R. Verzicco, P. Orlandi, and J. Mohd-Yusof. Combined immersed-boundary finite-difference methods for three-dimensional complex flow simulations. *Journal of Computational Physics*, 161(1):35–60, 2000.

- [12] O. M. Faltinsen, O. F. Rognebakke, and A. N. Timokha. Two-dimensional resonant piston-like sloshing in a moonpool. *Journal of Fluid Mechanics*, 575:359–397, 2007.
- [13] X. Feng and W. Bai. Wave resonances in a narrow gap between two barges using fully nonlinear numerical simulation. *Applied Ocean Research*, 50:119–129, 2015.
- [14] X. Feng, W. Bai, X. Chen, L. Qian, and Z. Ma. Numerical investigation of viscous effects on the gap resonance between side-by-side barges. *Ocean Engineering*, 145:44–58, 2017.
- [15] R. S. Figliola and D. E. Beasley. *Theory and design for mechanical measurements*. John Wiley & Sons, 2011.
- [16] J.-R. Fournier, M. Naciri, and X.-B. Chen. Hydrodynamics of two side-by-side vessels experiments and numerical simulations. In *Proceedings of the 16th International Offshore and Polar Engineering Conference, San Francisco, California, USA*, pages 158–165, May–June 2006.
- [17] D. C. Hong, S. Y. Hong, B. W. Nam, and S. W. Hong. Comparative numerical study of repulsive drift forces and gap resonances between two vessels floating side-by-side in proximity in head seas using a discontinuous HOBEM and a constant BEM with boundary matching formulation. *Ocean Engineering*, 72:331–343, 2013.
- [18] S. Hong, J. Kim, S. Cho, Y. Choi, and Y. Kim. Numerical and experimental study on hydrodynamic interaction of side-by-side moored multiple vessels. *Ocean Engineering*, 32(7):783–801, 2005.

- [19] C. Hu and M. Kashiwagi. A CIP-based method for numerical simulations of violent free-surface flows. *Journal of Marine Science and Technology*, 9(4):143–157, Dec 2004.
- [20] C. Hu and C. Liu. Development of Cartesian grid method for simulation of violent ship-wave interactions. *Journal of Hydrodynamics*, 28(6):1003–1010, 2016.
- [21] R. H. M. Huijsmans, J. A. Pinkster, and J. J. de Wilde. Diffraction and radiation of waves around side-by-side moored vessels. In *Proceedings of the 11th International Offshore and Polar Engineering Conference, Stavanger, Norway*, pages 406–412, June 2001.
- [22] M. Irvine, J. Longo, and F. Stern. Pitch and heave tests and uncertainty assessment for a surface combatant in regular head waves. *Journal of Ship Research*, 52(2):146–163, 2008.
- [23] ISO. Evaluation of measurement data—Guide to the expression of uncertainty in measurement. *JCGM100:2008*, 2008.
- [24] R. I. Issa. Solution of the implicitly discretised fluid flow equations by operator-splitting. *Journal of Computational Physics*, 62(1):40–65, 1986.
- [25] ITTC. Sample work instructions calibration of load cells, 7.6-02-09, rev. 0. *Recommended Procedures and Guidelines*, 2002.
- [26] ITTC. Floating offshore platform experiments, 7.5-02-07-03.1. *Recommended Procedures and Guidelines*, 2005.

- [27] ITTC. Seakeeping experiments, 7.5-02 07-02.1, rev. 4. *ITTC Recommended Procedures and Guidelines*, 2011.
- [28] N. G. Jacobsen, D. R. Fuhrman, and J. Fredsøe. A wave generation toolbox for the open-source CFD library: OpenFoam. *International Journal for Numerical Methods in Fluids*, 70(9):1073–1088, 2012.
- [29] H. Jasak. *Error analysis and estimation for the finite volume method with applications to fluid flows*. PhD thesis, Imperial College London (University of London), 1996.
- [30] S.-C. Jiang, W. Bai, P.-W. Cong, and B. Yan. Numerical investigation of wave forces on two side-by-side non-identical boxes in close proximity under wave actions. *Marine Structures*, 63:16–44, 2019.
- [31] S.-C. Jiang, W. Bai, and G.-Q. Tang. Numerical simulation of wave resonance in the narrow gap between two non-identical boxes. *Ocean Engineering*, 156:38–60, 2018.
- [32] M. Kashiwagi. 3-D calculation for multiple floating bodies in proximity using wave interaction theory. In *Proceedings of the 17th International Offshore and Polar Engineering Conference, Lisbon, Portugal*, pages 2246–2252, July 2007.
- [33] M. Kashiwagi, K. Endo, and H. Yamaguchi. Wave drift forces and moments on two ships arranged side by side in waves. *Ocean Engineering*, 32(5-6):529–555, 2005.

- [34] Y. Kim and G. Hermansky. Uncertainties in seakeeping analysis and related loads and response procedures. *Ocean Engineering*, 86:68–81, 2014.
- [35] N. Kodan. The motions of adjacent floating structures in oblique waves. *Journal of Energy Resources Technology*, 106(2):199–205, 1984.
- [36] T. Kristiansen and O. M. Faltinsen. Gap resonance analyzed by a new domain-decomposition method combining potential and viscous flow DRAFT. *Applied Ocean Research*, 34:198–208, 2012.
- [37] C. Liu and C. Hu. An efficient immersed boundary treatment for complex moving object. *Journal of Computational Physics*, 274:654–680, 2014.
- [38] L. Lu, L. Cheng, B. Teng, and L. Sun. Comparison of potential flow and viscous fluid models in gap resonance. In *Proceedings of the 25th International Workshop on Water Waves and Floating Bodies, Harbin, China*, pages 1–4, May 2010.
- [39] S. Mayer, A. Garapon, and L. S. Sørensen. A fractional step method for unsteady free-surface flow with applications to non-linear wave dynamics. *International Journal for Numerical Methods in Fluids*, 28(2):293–315, 1998.
- [40] S. Maysam Mousaviraad, S. Hamid Sadat-Hosseini, P. M. Carrica, and F. Stern. Ship-ship interactions in calm water and waves. part 2: URANS validation in replenishment and overtaking conditions. *Ocean Engineering*, 111:627–638, 2016.
- [41] S. Maysam Mousaviraad, S. H. Sadat-Hosseini, and F. Stern. Ship-ship interactions in calm water and waves. Part 1: Analysis of the experimental data. *Ocean Engineering*, 111:615–626, 2016.

- [42] K. McTaggart. Radiation and diffraction forces and motions for two ships at moderate forward speed. In *SNAME Maritime Convention, Houston, Texas, USA*, pages 1–20, October 2017.
- [43] K. McTaggart, D. Cumming, C. C. Hsiung, and L. Li. Seakeeping of two ships in close proximity. *Ocean Engineering*, 30(8):1051–1063, 2003.
- [44] K. McTaggart, P. R. de Reilhac, L. Boudet, and S. Oakey. Validation of a distributed simulation of ship replenishment at sea with model tests. *Journal of Marine Science and Technology*, 24:1209–1222, 2018.
- [45] W. Meng, H. Peng, and W. Qiu. Cfd simulations of two-body interactions in waves (accepted). In *Proceedings of the 33rd Symposium on Naval Hydrodynamics, Osaka, Japan*, October 2020.
- [46] W. Meng and W. Qiu. Simulation of two-body interaction in waves with the immersed boundary method. In *Proceedings of the 34th International Workshop on Water Waves and Floating Bodies, Newcastle, Australia*, pages 1–4, April 2019.
- [47] R. Mittal and G. Iaccarino. Immersed boundary methods. *Annual Review of Fluid Mechanics*, 37(1):239–261, 2005.
- [48] J. Mohd-Yusof. Combined immersed-boundary/b-spline methods for simulations of flow in complex geometries. In *Annual Research Briefs, Center for Turbulence Research, Stanford University*, pages 317–327, 1997.

- [49] B. MOLIN. On the piston and sloshing modes in moonpools. *Journal of Fluid Mechanics*, 430:27–50, 2001.
- [50] B. Molin and F. Remy. Experimental and numerical study of the gap resonances in-between two rectangular barges. In *Proceedings of the 13th Congress of International Maritime Association of the Mediterranean, Istanbul, Turkey*, pages 1–8, October 2009.
- [51] J. N. Newman. Application of generalized modes for the simulation of free surface patches in multiple body interactions. In *Report of the 4th Annual WAMIT Consortium Meeting, Woods Hole, USA*, October 2003.
- [52] J. N. Newman and P. D. Sclavounos. The computation of wave loads on large offshore structures. In *Proceedings of the International Conference on Behaviour of Off-shore Structures, Trondheim, Norway*, pages 1–18, June 1988.
- [53] M. Ohkusu. On the heaving motion of two circular cylinders on the surface of a fluid. *Reports of Research Institute for Applied Mechanics, Kyushu University*, 17:167–185, 1969.
- [54] H. T. Ok, S. J. Lee, and J. H. Choi. Numerical simulation of motion of single and side-by-side vessels in regular waves using OpenFOAM. *Ships and Offshore Structures*, 12(6):793–803, 2017.
- [55] W. H. Pauw, R. H. M. Huijsmans, and A. Voogt. Advances in the hydrodynamics of side-by-side moored vessels. In *Proceedings of the 26th International Conference on Offshore Mechanics and Arctic Engineering, San Diego, California, USA*, pages 597–603, June 2007.

- [56] H. Peng, M. A. Ali, and W. Qiu. Hydrodynamic interaction of two bodies in waves. In *Proceedings of the 30th International Workshop on Water Waves and Floating Bodies, Bristol, UK*, pages 1–4, April 2015.
- [57] H. Peng and W. Qiu. Computation of motion and added wave resistance with the panel-free method. *Journal of Offshore Mechanics and Arctic Engineering*, 136(3):1–9, 06 2014.
- [58] M. Perić and C. Swan. An experimental study of the wave excitation in the gap between two closely spaced bodies, with implications for lng offloading. *Applied Ocean Research*, 51:320–330, 2015.
- [59] C. S. Peskin. Flow patterns around heart valves: A numerical method. *Journal of Computational Physics*, 10(2):252–271, 1972.
- [60] A. Pinelli, I. Naqavi, U. Piomelli, and J. Favier. Immersed-boundary methods for general finite-difference and finite-volume navierstokes solvers. *Journal of Computational Physics*, 229(24):9073–9091, 2010.
- [61] W. Qiu, W. Meng, H. Peng, J. Li, J.-M. Rousset, and C. A. Rodríguez. Benchmark data and comprehensive uncertainty analysis of two-body interaction model tests in a towing tank. *Ocean Engineering*, 171:663–676, 2019.
- [62] W. Qiu and H. Peng. Computation of forward-speed wave-body interactions in frequency domain. *International Journal of Offshore and Polar Engineering*, 17(2):125–131, 2007.

- [63] W. Qiu and H. Peng. Numerical solution of body-exact problem in the time domain. *Journal of Ship Research*, 57(1):13–23, 2013.
- [64] W. Qiu, H. Peng, and J. M. Chuang. Computation of wave-body interactions using the panel-free method and exact geometry. *Journal of Offshore Mechanics and Arctic Engineering*, 128(1):31–38, 02 2006.
- [65] W. Qiu, J.-M. Rousset, H. Peng, W. Meng, and B. Horel. Benchmark tests of two body interaction in waves. In *Proceedings of the 36th International Conference on Ocean, Offshore and Arctic Engineering, Trondheim, Norway*, pages 1–8, June 2017.
- [66] W. Qiu, J. Sales, D. Lee, H. Lie, V. Magarovskii, T. Mikami, J.-M. Rousset, S. Sphaier, L. Tao, and X. Wang. Uncertainties related to predictions of loads and responses for ocean and offshore structures. *Ocean Engineering*, 86:58–67, 2014.
- [67] C. M. Rhie and W. L. Chow. Numerical study of the turbulent flow past an airfoil with trailing edge separation. *AIAA Journal*, 21(11):1525–1532, 1983.
- [68] J. Roenby, H. Bredmose, and H. Jasak. A computational method for sharp interface advection. *Royal Society Open Science*, 3(11):1–27, 2016.
- [69] M. Uhlmann. An immersed boundary method with direct forcing for the simulation of particulate flows. *Journal of Computational Physics*, 209(2):448–476, 2005.

- [70] G. Van Oortmerssen. Hydrodynamic interaction between two structures floating in waves. In *Proceedings of the 2nd International Conference on Behaviour of Off-shore Structures, London, England*, pages 339–356, August 1979.
- [71] D. Vieira, P. de Mello, R. Dotta, and K. Nishimoto. Experimental investigation on the influence of the liquid inside the tanks in the wave behavior of fmg vessels in side-by-side offloading operations. *Applied Ocean Research*, 74:28–39, 2018.
- [72] V. Vukčević, H. Jasak, and Š. Malenica. Decomposition model for naval hydrodynamic applications, Part I: Computational method. *Ocean Engineering*, 121:37–46, 2016a.
- [73] V. Vukčević, H. Jasak, and Š. Malenica. Decomposition model for naval hydrodynamic applications, Part II: Verification and validation. *Ocean Engineering*, 121:76–88, 2016b.
- [74] R. Watai, P. Dinoi, F. Ruggeri, A. Souto-Iglesias, and A. Simos. Rankine time-domain method with application to side-by-side gap flow modeling. *Applied Ocean Research*, 50:69–90, 2015.
- [75] P. Wen and W. Qiu. Improved prediction of 3-D water entry with a CIP method and parallel computing. *Ocean Engineering*, 164:426–442, 2018.
- [76] M. D. Woodward, M. van Rijsbergen, K. W. Hutchinson, and A. Scott. Uncertainty analysis procedure for the ship inclining experiment. *Ocean Engineering*, 114:79–86, 2016.

- [77] J. Yang and E. Balaras. An embedded-boundary formulation for large-eddy simulation of turbulent flows interacting with moving boundaries. *Journal of Computational Physics*, 215(1):12–40, 2006.
- [78] J. Yang and F. Stern. Sharp interface immersed-boundary/level-set method for wave-body interactions. *Journal of Computational Physics*, 228(17):6590–6616, 2009.
- [79] X. Yang, X. Zhang, Z. Li, and G.-W. He. A smoothing technique for discrete delta functions with application to immersed boundary method in moving boundary simulations. *Journal of Computational Physics*, 228(20):7821–7836, 2009.
- [80] W. Zhao, J. Yang, Z. Hu, and L. Tao. Prediction of hydrodynamic performance of an fmg system in side-by-side offloading operation. *Journal of Fluids and Structures*, 46:89–110, 2014.
- [81] Q. Zhou, M. Liu, H. Peng, and W. Qiu. Experimental studies of hydrodynamic interaction of two bodies in waves. In *Proceedings of the 36th International Conference on Ocean, Offshore and Arctic Engineering, St. Johns, Canada*, pages 1–9, June 2015.
- [82] Y. Zhuang and D. Wan. CFD modeling on gap flows of two ships with side-by-side vonfiguration in waves. In *Proceedings of the 28th International Ocean and Polar Engineering Conference, Sapporo, Japan*, pages 1223–1228, June 2018.

Appendix A

Example of Uncertainty Calculation

As an example, details on the calculation of uncertainties in the heave motion of Model 1, wave elevation at WP4 in the gap and the longitudinal drift force on Model 1 at the frequency 5.91 rad/s are given below to illustrate the uncertainty calculation process.

Based on Eq. (3.7), the Type A standard uncertainties of the measurements were obtained from repeated measurements and presented in Table A.1.

Note that the mean value of F_{11} , the longitudinal mean drift force on Model 1, is the summation of longitudinal components of mooring forces, F_{M1} , F_{M2} , F_{M3} and F_{M4} , where M1 and M2 denote the two mooring lines on the port and starboard sides of the bow, respectively; M3 and M4 are those at the stern. The standard uncertainty was calculated as

$$u_{F_{11A}}^2 = u_{F_{M1A}}^2 + u_{F_{M2A}}^2 + u_{F_{M3A}}^2 + u_{F_{M4A}}^2 \quad (\text{A.1})$$

Table A.1: Type A standard uncertainties (at the wave frequency of 5.91 rad/s)

Item	ξ_2	ξ_4	x_{31}	F_{M1}	F_{M2}	F_{M3}	F_{M4}	F_{11}
Unit	(mm)	(mm)	(mm)	(N)	(N)	(N)	(N)	(N)
Test 1	27.200	20.265	3.898	-0.256	-0.220	-0.240	-0.229	-
Test 2	26.651	21.156	4.306	-0.266	-0.229	-0.247	-0.236	-
Test 3	27.592	22.674	4.089	-0.273	-0.228	-0.245	-0.246	-
Test 4	27.798	23.397	4.079	-0.261	-0.216	-0.231	-0.235	-
Test 5	28.032	23.689	4.140	-0.269	-0.208	-0.222	-0.247	-
Mean	27.455	22.236	4.102	-0.265	-0.220	-0.237	-0.239	-0.961
u_A	0.243	0.660	0.065	0.003	0.004	0.005	0.003	0.008

The Type B standard uncertainties were obtained considering uncertainties from sensor calibration, manufacturer's specifications and numerical simulations. The standard uncertainties are given in Table A.2.

Table A.2: Type B standard uncertainties (at the wave frequency of 5.91 rad/s)

Item	ξ_2	ξ_4	x_{31}	F_{M1}	F_{M2}	F_{M3}	F_{M4}	F_{11}
Unit	(mm)	(mm)	(mm)	(N)	(N)	(N)	(N)	(N)
u_{CB}	1.381	1.461	0.077	0.030	0.060	0.052	0.026	0.089
u_{MB}	0.044	0.036	-	0.018	0.031	0.032	0.032	0.058
u_{NB}	-	0.333	0.047	-	-	-	-	0.042
u_B	1.382	1.499	0.090	-	-	-	-	0.114

Considering the degrees of freedom for measurements as 4 and infinity for Type A

and Type B evaluations, respectively, the effective degrees of freedom were obtained according to Eq. (3.10). Coverage factors were interpolated by assuming a confidence level of 95%. The expanded Type A and Type B uncertainties were calculated according to Eq. (3.9) and are presented in Table A.3.

Table A.3: Combined uncertainties (at the wave frequency of 5.91rad/s)

	x'_{31}	ξ'_4	F'_{11}
value	0.156	0.847	-0.284
u_{cA}	0.003	0.026	0.006
ν_{effA}	6.260	4.707	5.669
k_A	2.422	2.600	2.490
u_{eA}	0.007	0.068	0.014
u_{cB}	0.009	0.073	0.046
ν_{effB}	∞	∞	∞
k_B	1.960	1.960	1.960
u_{eB}	0.017	0.142	0.090

Appendix B

Investigations on Wave Modelling

Length of wave damping zone, vertical grid size, cell aspect ratio and time step for wave modelling were investigated for the zero-speed and the forward-speed cases without the presence of ship models. As shown in Fig. B.1, the length of inlet relaxation zone was kept greater than one wavelength, the computational zones were three times the length of the FPSO model and the frigate model for the zero-speed and the forward-speed cases, respectively. The width and the depth of the numerical wave tanks were set the same as those of the physical towing tanks (4.6 m wide and 1.8 m deep for the zero-speed cases and 12 m wide and 7 m deep for the forward-speed cases). Wave elevations at the origin of $OXYZ$, i.e., the intersection of the centreline of the gap and the midship section of the models, 0.5 m ahead and 0.5 m behind the midship section for the zero-speed cases, and 1.0 m ahead and 1.0 m behind the midship section for the forward-speed cases, were checked against the targeted values. In the figure, the wave probe locations are indicated by WP4 (front), WP5 (middle) and WP6 (back), respectively.

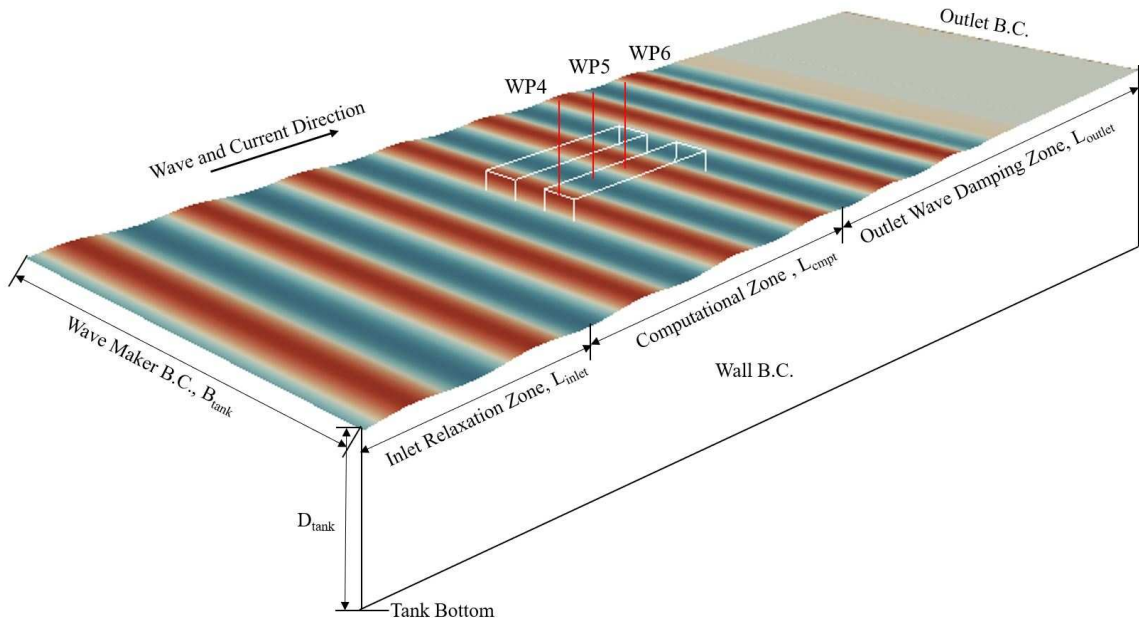


Figure B.1: Simulation Set-up

Effects on wave elevations at the targeted locations were examined by changing the number of cells per wave height, H_w , the cell aspect ratio in the wave refinement zone, the length of outlet wave damping zone, L_{outlet} , and the time step. Note that the time step is expressed in terms of the Courant-Friedrichs-Lewy number, $CFL = U_w \Delta t / \Delta z$, where U_w is the wave speed, Δt is the time step and Δz is the vertical cell size in the wave refinement zone.

Figure B.2 presents the relative error, E_η , at WP4 for the zero-speed cases and at WP5 for the forward-speed cases, in the predicted wave elevation with respect to the targeted value versus the number of cells per wave height. In this figure, the aspect ratio of a cell was kept as 4, CFL was set 0.1, and the outlet wave damping zone was 5 times the wavelength. It can be seen that at least 8-10 cells per wave height is needed for wave generation.

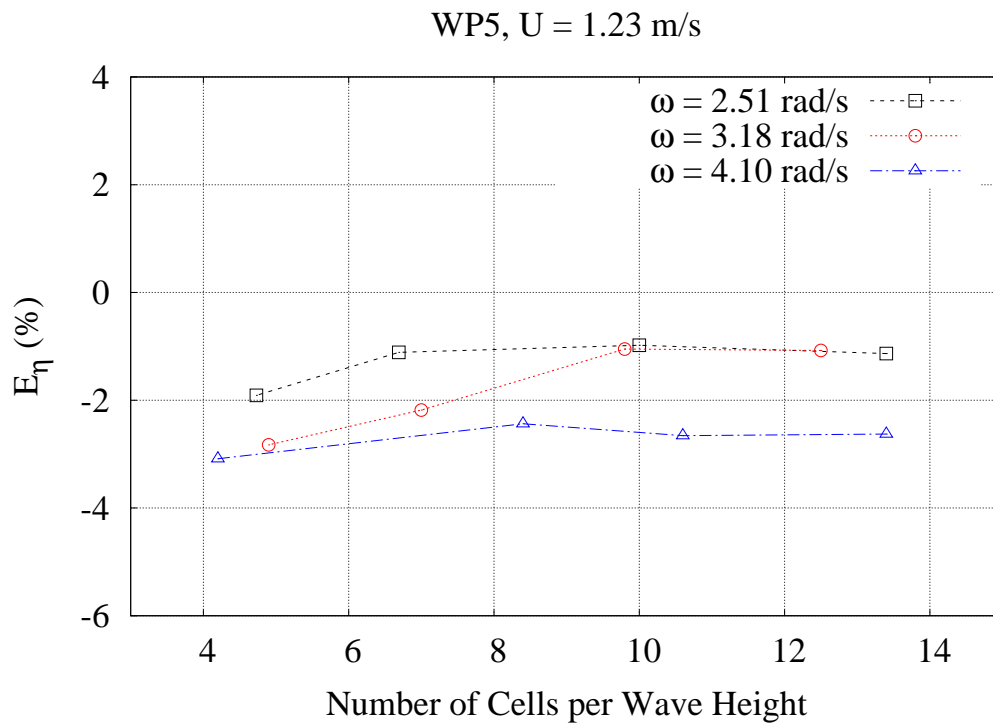
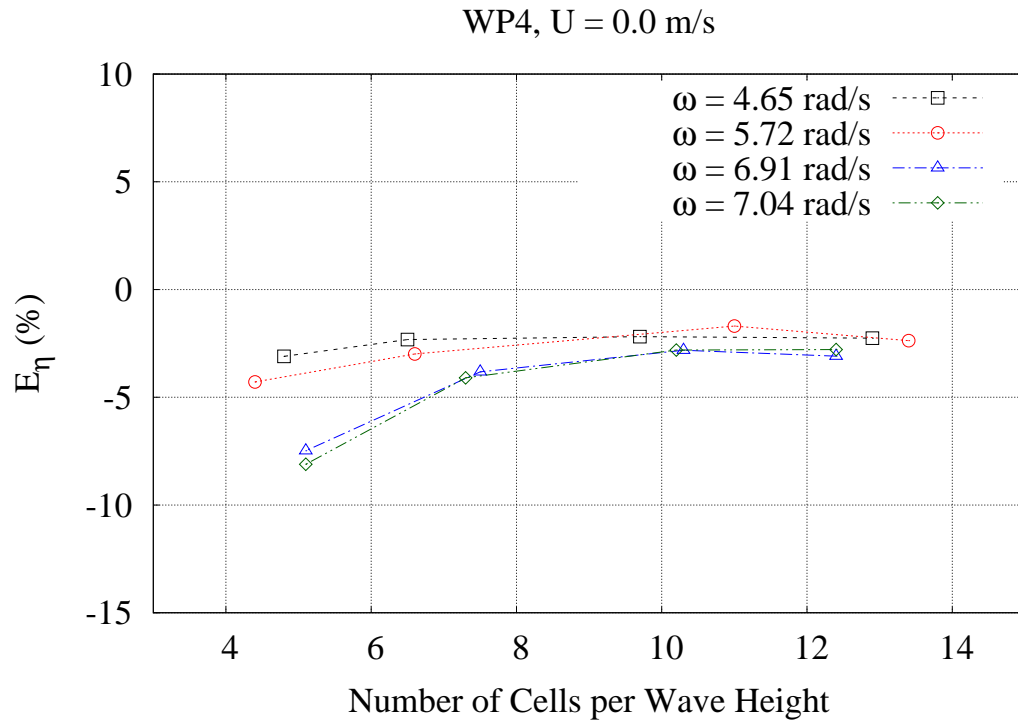


Figure B.2: Effect of Vertical Cell Size on Wave Generation

The effect of cell aspect ratio in the wave refinement zone is shown in Fig. B.3. In the simulations, about 10 cells were distributed over wave height, CFL was 0.1 and the outlet wave damping zone was 5 times the wavelength. The relative errors, E_η , indicated that the cell aspect ratio should be less than 2^2 . The aspect ratio of 4 was then chosen as the best-practice value.

Figure B.4 shows the effect of the length of the outlet wave damping zone at WP5 for the zero- and forward-speed cases, and Fig. B.5 additionally presents the relative error, E_η , at WP4 and WP6 for the zero-speed cases. In all the cases, about 10 cells were distributed over wave height, the cell aspect ratio was kept as 4 and CFL was 0.1. It can be seen that zero-speed cases are more sensitive to the length of the damping zone than the forward-speed cases, and the wave elevations vary locally due to the reflected waves from the outlet wave damping zone. Based on these results, the length of the damping zone should be no less than 5 wavelengths.

Further studies on the time step were conducted with about 10 cells over wave height, the cell aspect ratio of 4, and 5 times the wavelength for the outlet wave damping zone. As shown in Fig. B.6, CFL should be around 0.1 - 0.15 for accuracy and efficiency.

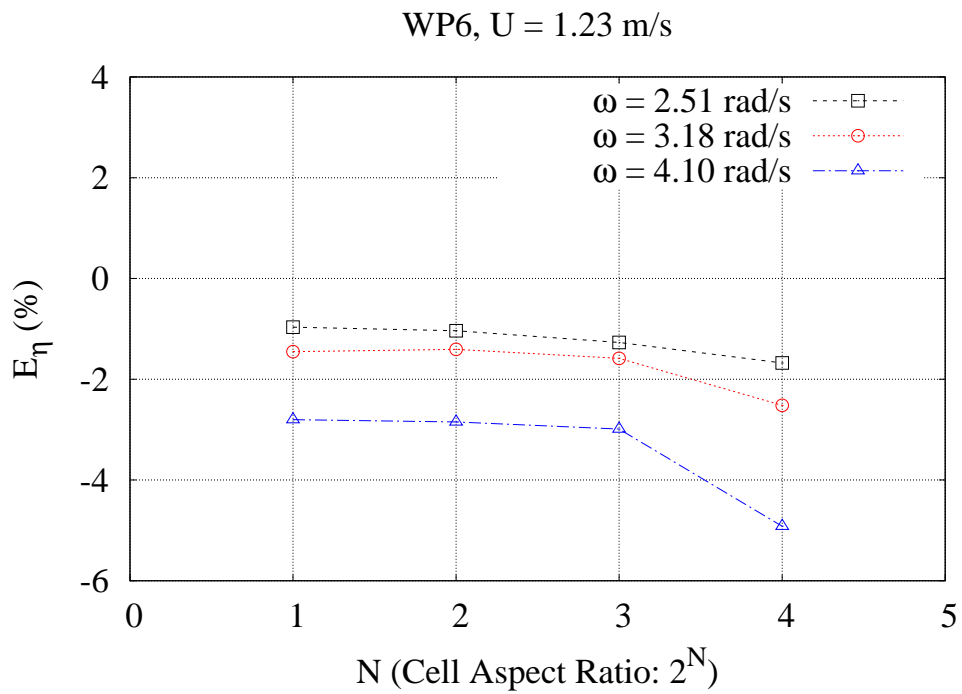
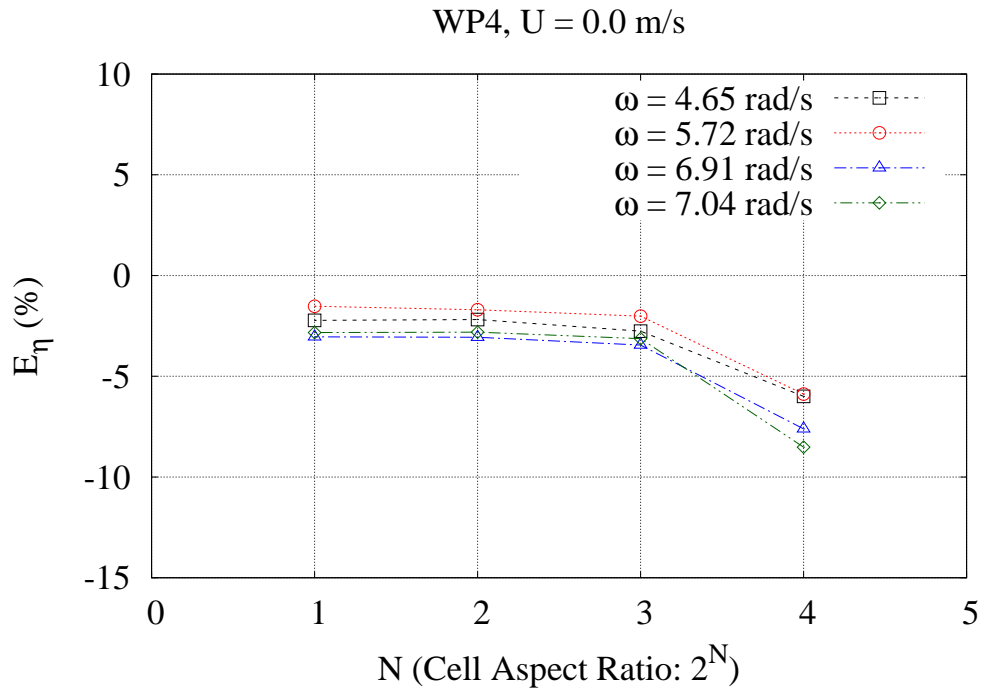


Figure B.3: Effect of Cell Aspect Ratio on Wave Generation

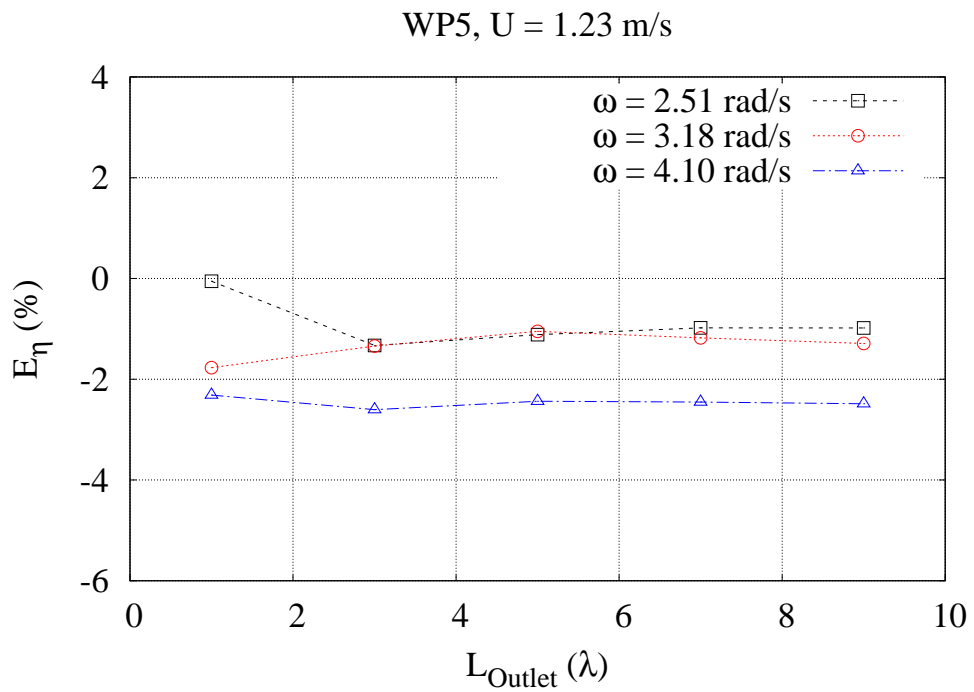
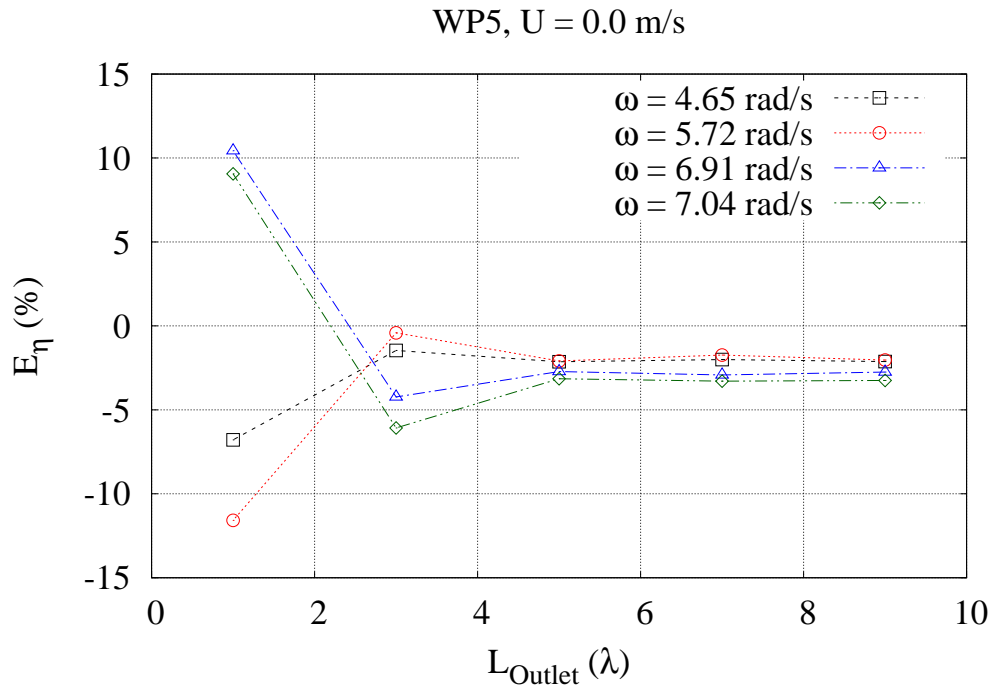


Figure B.4: Effect of Damping Zone Length on Wave Generation

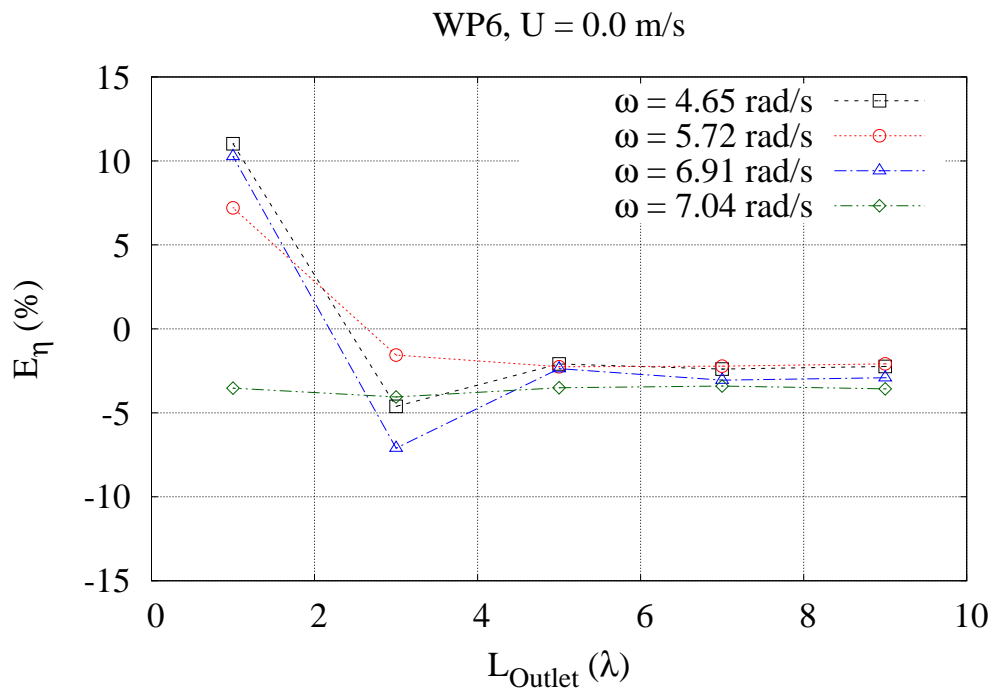
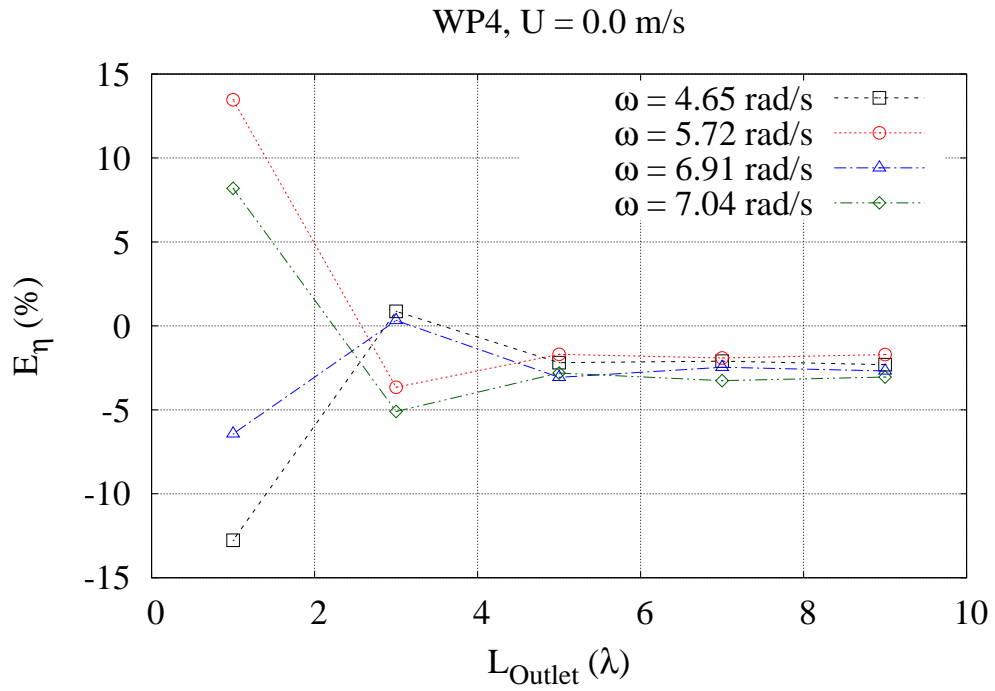


Figure B.5: Effect of Damping Zone Length on Wave Generation

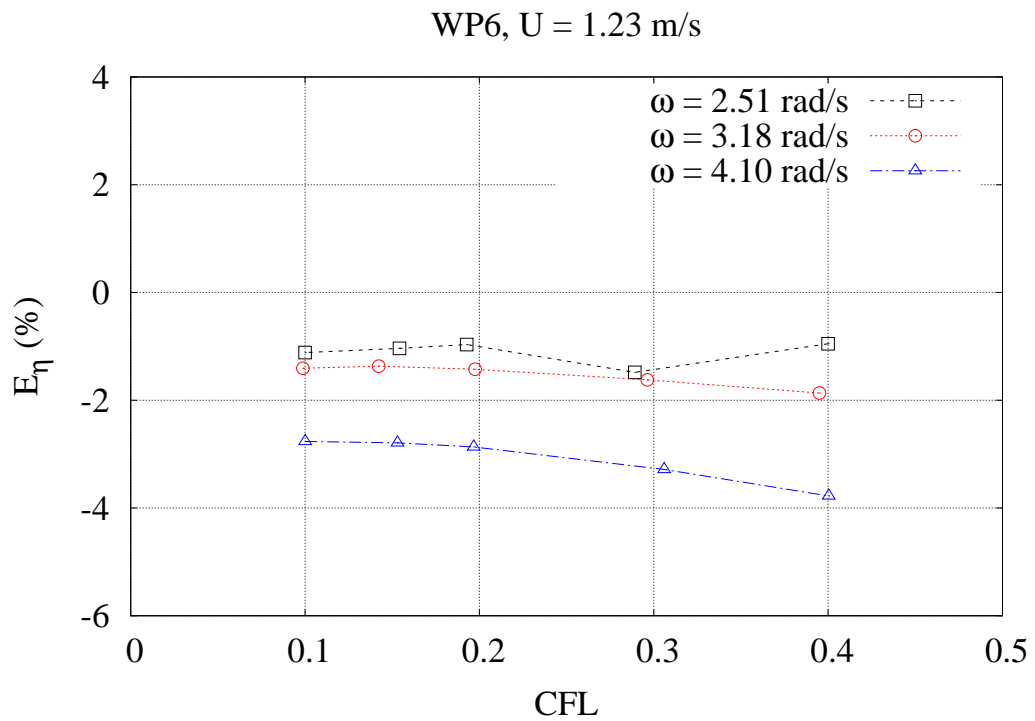
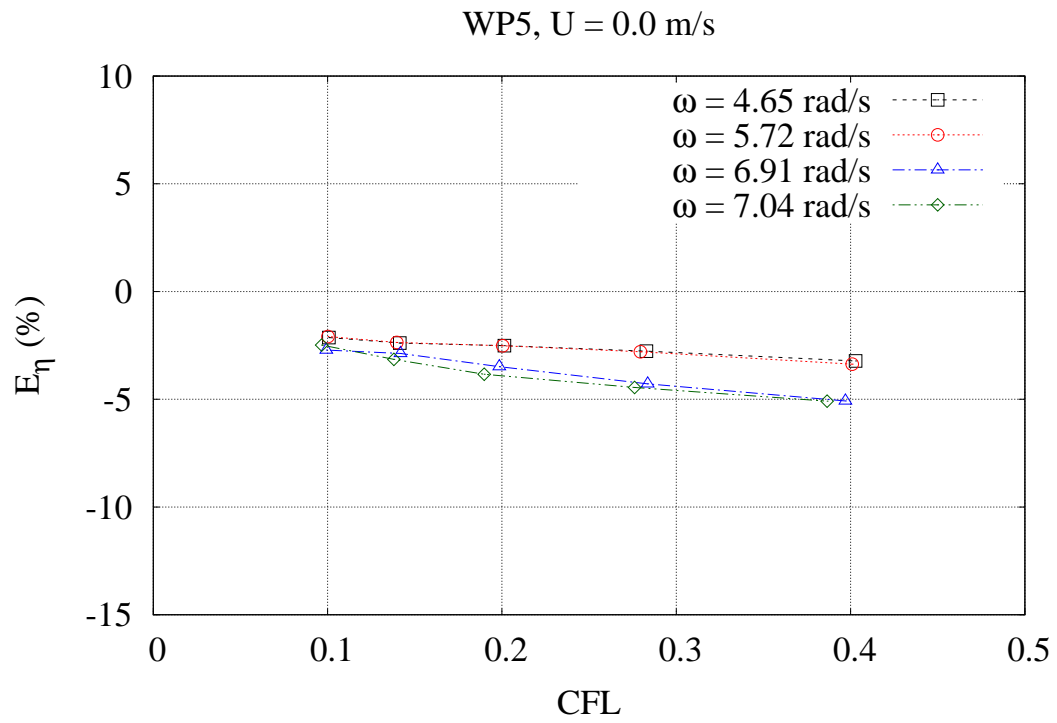


Figure B.6: Effect of Time Step on Wave Generation